MODELING THE GREAT SALT LAKE

by

Ibrahim Nourein Mohammed

A thesis submitted in partial fulfillment
of the requirements for the degree

of

MASTER OF SCIENCE
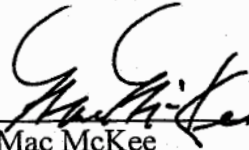
in

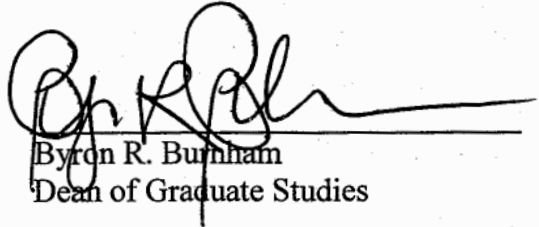Civil and Environmental Engineering

Approved:

_____   _____
David G. Tarboton   Mac McKee
Major Professor   Committee Member

_____   _____
Michael C. Minnotte   Byron R. Burnham
Committee Member   Dean of Graduate Studies

UTAH STATE UNIVERSITY
Logan, Utah

2006

ABSTRACT

Modeling the Great Salt Lake

by

Ibrahim Nourein Mohammed, Master of Science

Utah State University, 2006

Major Professor: Dr. David G. Tarboton
Department: Civil and Environmental Engineering

This work investigated fluctuations in the Great Salt Lake level and volume
due to variability in the climate and the hydrology of the river basins that drain to the
lake, as well as internal dynamics related to the lake bathymetry and salinity. The
Great Salt Lake is a terminal lake whose level is determined by the balance between
inflows and outflows. Inflows are from three major rivers and precipitation directly
on the lake. The only outflow is evaporation. Evaporation is sensitive to lake area,
which changes with lake level according to the bathymetry. Evaporation is also
sensitive to salinity, which changes the lake surface saturation vapor pressure.
Salinity changes with lake volume as the total salt load in the lake becomes
concentrated or diluted.

This work examined the role of topography/bathymetry in the lake dynamics
and the occurrence of modes in the total volume probability distribution.

Bathymetry, expressed in the form of (level-area-volume) relationships, transforms the area probability density function into the volume probability density function. Modes in the area density function are suggested to represent preferred states in the climate. These area density function modes are modified as they propagate through to the volume density function.

This work also examined the impact of salinity on GSL evaporation, through the effect that it has on saturation vapor pressure, was quantified using the water activity coefficient. The reduction in saturation vapor pressure varies from 10% to 40% depending upon salinity. This reduction in saturation vapor pressure was accommodated in a modification to the Penman equation that was used to calculate Lake Evaporation based on climate inputs. Comparisons between evaporation calculations accounting for salinity and lake evaporation estimates from mass balance and lake level observations validated these salinity modifications to the Penman equation.

The overall result of this study is an improved quantitative understanding of the large scale interactions involved in the dynamics of the Great Salt Lake basin system.

(127 pages)

ACKNOWLEDGMENTS

My gratitude is to my father, Nourein; my mother, Bothyna; my sisters, Nisreen, Nora, Noha, and Najwan; and my brother, Mohammed, whom I love for their strong stand and encouragement during my study. This success is accredited to their wishes and prayers.

I thank my colleagues, classmates, and friends in the hydrology lab and back home in Sudan who stood behind me. They shared with me my feelings, discussed with me this work, and prayed for me to achieve this task.

Ibrahim Nourein Mohammed

CONTENTS

LIST OF TABLES

LIST OF FIGURES

CHAPTER 1

GENERAL INTRODUCTION

1.1. Problem Statement

The Great Salt Lake (GSL) is the fourth largest, perennial, closed basin in the world. The lake is shallow (average depth 4-6 m), with a large surface area (greater than 6400 km^2), and its salinity ranges from 5% to 28%. Covering portions of northern Utah, southern Idaho, and western Wyoming, the GSL drainage has an area of 54,955 km^2 (21,500 square miles). GSL inflows are from three major rivers in the Wasatch Region, the Bear, Provo/Jordan, and Weber rivers in addition to groundwater seepage. The only outflow is evaporation. The evaporation depends upon meteorological factors, salinity, and the lake surface area, which fluctuates with level.

Closed basin lakes, such as GSL, are sensitive in terms of exhibiting a natural balance between inflows and outflows. Moreover, they are sensitive to long-term climatic fluctuations that integrate out high-frequency variability. Previous work (Lall and Mann, 1995,Lall, Sangoyomi, and Abarbanel, 1996) has explored and developed an empirical understanding of the role of climatic variability in the dynamics of the Great Salt Lake (GSL) of Utah. Sangoyomi, Lall, and Abarbanel (1996) studied the possibility that variations in the volume of the GSL may be described as a low-dimensional nonlinear dynamical system. In addition, Sangoyomi (1993) has shown that the GSL volume time series reveals significant

interannual and interdecadal fluctuations, which are related to regional climatic variability and are important for understanding and forecasting drought and the long-term availability of water. This prior work did not explicitly consider the interplay between lake volume and surface area which is a major control on the evaporation outflux.

Fluctuations of the GSL's level are of direct concern to industries and infrastructure along the shore such as the Salt Lake City Airport, the Union Pacific Railroad, wastewater treatment plants, and Interstate highway 80 (Lall, Sangoyomi, and Abarbanel, 1996). They are also well correlated with regional water supply conditions. During 1983-1986 the Great Salt Lake rose rapidly to its highest level in a hundred years and then declined quickly. A pumping project (the West Desert Project) that cost about $60 million was initiated due to that event. During April 10, 1987 to June 30, 1989 more than 2.5 million acre-feet of water and 695 million tons of salt were removed from the lake as part of the West Desert Pumping Project (Wold and Waddell, 1994). From January 1990 to June 1992, 200,000 acre-feet of water and 94 million tons of salt returned to the lake from West Pond (Loving, Waddell, and Miller, 2000). The following decade (1990-2000) has seen concern that the GSL might be drying up. In examining such behaviors we have to consider the dynamics of the GSL, because high levels threaten infrastructure, while low levels put large scale industries in jeopardy.

Figure 1-1 depicts the primary processes that interact in the GSL basin system. This figure identifies solar radiation, precipitation, and air humidity as the

primary drivers of this system. For example, precipitation drives the snow which in turn supplies streamflow (the dominate contributor). Precipitation affects the soil moisture and groundwater which also feeds to the GSL. Meanwhile, solar radiation affects air temperature which itself reduces snow that supplies streamflow. On the other hand, evaporation may impact cloudiness, solar radiation and precipitation, ultimately impacting the degree of recycling of water in the lake-basin system. Air temperature increases evaporation which is area controlled. Evaporation reduces the lake volume, which reduces lake area and increases salinity. Both reduced lake area and increased salinity reduce the evaporation, a negative feedback in the system. Salinity affects evaporation by reducing the saturation vapor pressure over a saline water surface relative to a fresh water surface. This reduction in saturation vapor pressure has been explained as function of the brine's ionic composition, water activity coefficient, by Salhotra, Adams, and Harleman (1985).

The problem addressed in this work will be modeling of changes in GSL volume and fluctuations in GSL level as they are related to the forcings, such as precipitation, temperature, and other measures of climate that act on the lake-basin system. We will compare peaks in the area-volume derivatives with modes in the lake volume distribution to examine the role of the topography/bathymetry on the GSL volume fluctuations. Also, we will address evaporation from the GSL by modeling the relationship of saturation vapor pressure to salinity. The goal of this work is to develop and improve understanding of the various processes described in Figure 1-1 and how they are related to the GSL hydrology. We would like to better

understand how both external forcings and internal feedbacks are involved in GSL basin system dynamics. The intent is for this work to contribute to better understanding of long-term, large-scale climatic fluctuations and their interaction with surface hydrology. We would like to understand the climate conditions that could lead to changes in lake levels/volumes. Better understanding of lake processes can help towards better physical model forecasts of lake levels and volumes. Such forecasts are important to assess the risks of low or high lake levels that have consequences for lake resources and management of infrastructure such as the pumps for protection against flooding.

1.2. Objectives

Our specific objectives are to:

1. quantify the relationships identified in Figure 1-1, through exploratory data analysis and statistical modeling.

2. explore the possibility of relationships between modes in the lake volume distribution and attributes of the topographic area-volume relationship.

Both stochastic and physical models will be used in this work with physical reasoning used as a guide for the exploration of statistical relationships between lake volume changes and input variables. These relationships may tell us something about the nature of the system generating the time series of the GSL. Also, they can be used for forecasting the GSL volume.
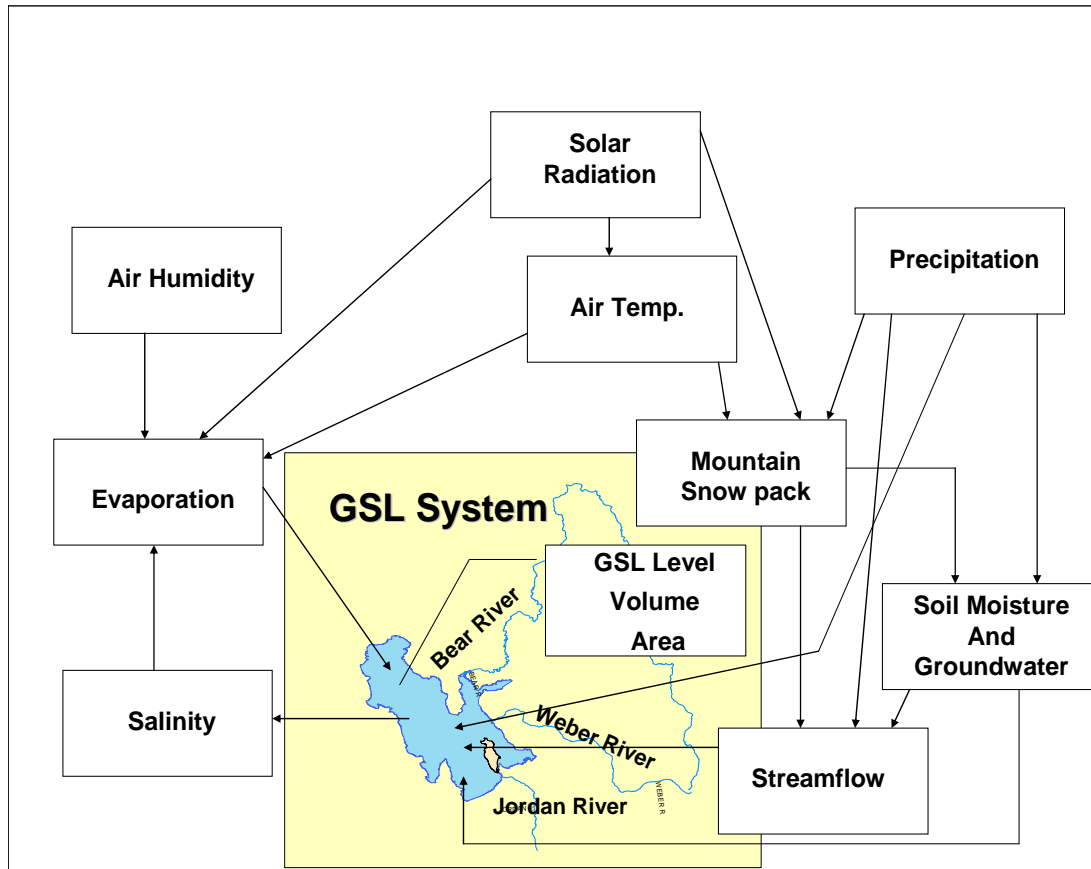
Figure 1-1.   Primary process interactions in the Great Salt Lake Basin that drive
lake volume fluctuations.

1.3. Study Area

The Great Salt Lake (latitude 40° to 42° N, longitude 112° to 113° W) is a
closed lake in the lowest part of the Great basin, located in semiarid northwestern
Utah, United States (Figure 1-2). It is a remnant of freshwater Lake Bonneville,
which existed about 10 to 15 thousand years ago. The GSL is approximately 113
kilometers long and 48 kilometers wide, with a maximum depth of about 14 meters.
The effective area of Great Salt Lake basin is about 54,955 km^2. Most of the inflow

to GSL comes from rivers draining the three major watersheds, the Bear River watershed (19,262 km^2), the Weber River watershed (6,413 km^2) and the Jordan/ Provo River watershed (9,963 km^2).   These three major rivers originate in the western end of the Uinta Mountains, along the eastern edge of the basin at altitudes above 3,000 m.   The Bear and Weber Rivers discharge directly in the Great Salt Lake.   The Provo River discharges into Utah Lake, a freshwater lake at the south end of the Great Salt Lake valley.   The Jordan River drains from Utah Lake north into the Great Salt Lake.   The Wasatch Region, which is the major effective drainage area to the GSL, is located along the eastern edge of the Great Basin trending north-south and rising more than 2,000 m above the floor of the Great Salt Lake Valley.   A substantial part of the Great Salt Lake basin is the west desert (14,604 km^2).   There are no perennial streams in this area.   The west desert, though, is believed to yield small amount of groundwater to GSL.   Precipitation mostly in winter has a strong orographic signature in the GSL basin.

The level of the Great Salt Lake has fluctuated dramatically over the years. In 1963, when Great Salt Lake was at its lowest water-surface elevation in recent history at about 1,277.4 m (4,191 ft), it covered about 2,460.5 km^2 (950 mi^2) and was about 7.6 m deep at its deepest point.   In 1987, when Great Salt Lake was at its highest water-surface elevation in recent history at about 1,283.8 m (4,212 ft) on April 1st, 1987, it covered about 6,216 km^2 (2,400 mi^2) and was about 13.7 m at its deepest point (Loving, Waddell, and Miller, 2000).   The large surface area and shallow depth make the lake very sensitive to fluctuations in long-term climate.

Lake level has been monitored since 1847 (Figure1-3), although the early readings are infrequent and sometimes anecdotal. The locations of present day GSL level recorders are shown in Figure 3-1.

Sub-basin Drainage Areas		
Bear	19,262	km²
Weber	6,413	km²
West Desert	14,604	km²
Jordan/ Provo	9,963	km²
Salt Lake	4,713	km²
Total	54,955	km²
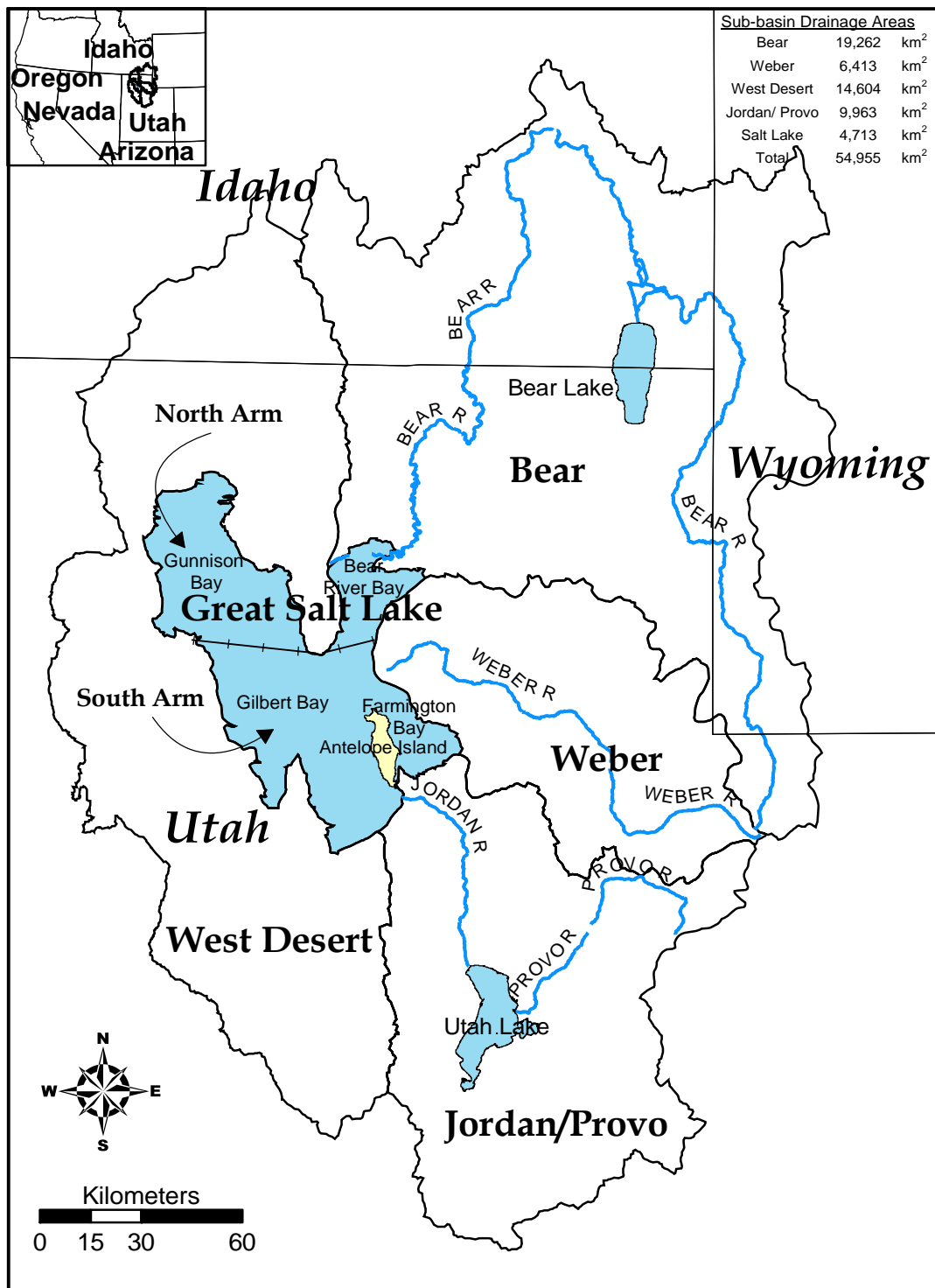
Figure 1-2.   The Great Salt Lake Basin with major sub-basins. The Great Salt Lake is located in the western United States (upper left).
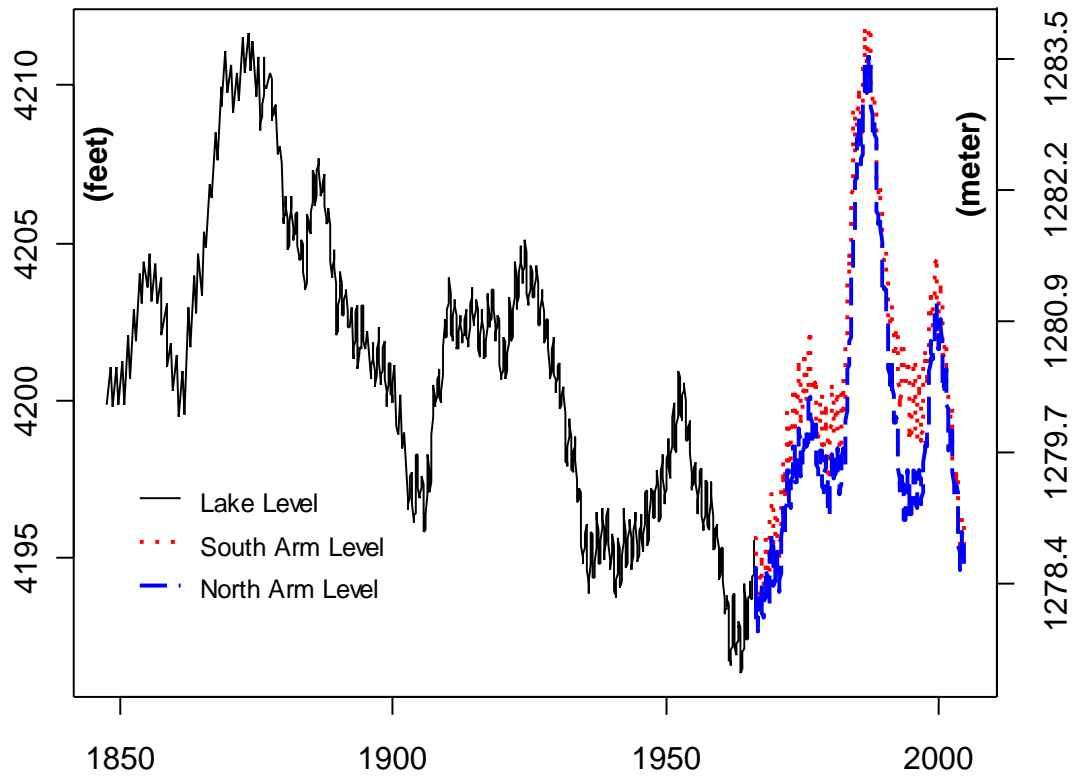
Figure 1-3. Great Salt Lake level data from the Utah Geological Survey. The lake was divided into North and South arms by a railroad causeway in 1959. Separate records of level in the North Arm and South Arm are available from 1966.

CHAPTER 2

LITERATURE REVIEW

2.1. Time Series Models

Many authors applied stochastic hydrological models to the GSL as a
hydrological system. One of the goals of James et al. (1979) was to develop a
stochastic hydrology model that would accurately represent Great Salt Lake inflow
and outflow sequences. James et al. (1979) developed two Autoregressive Moving
Average (ARMA) models to achieve that goal; namely ARMA (1, 0) and ARMA (1,
1). ARMA (1, 0) refers to a model having one autoregression and no moving average
terms, while ARMA (1, 1) has one auto regression and one moving average term.
These models simulated flow into the lake and were used as input to a water balance
model which in turn provided the basis for a damage simulation model. The water
balance model uses input sequences of evaporation, precipitation, and streamflow
(Bear, Weber, and Jordan) over a common historical period. James et al. (1979)
suggested using ARMA (1, 0) for their flow simulation model. Their choice to use
ARMA (1, 0) option was based upon its simplicity and sufficiency for meeting the
needs of the study.

Nonparametric methods for the generation of synthetic time series in
stochastic hydrology have been developed (Lall, 1995,Lall and Sharma,
1996,Sharma, Tarboton, and Lall, 1997,Tarboton, Sharma, and Lall, 1998). These
are based on the idea that stochastic simulation is resampling from the joint

distribution of streamflow over the number of time steps needed to capture the dependence structure in the Streamflow time series. In the NP1 approach Sharma, Tarboton, and Lall (1997) used kernel estimates of the joint and conditional probability density functions to generate synthetic streamflow sequences. Lall and Sharma (1996) used a nearest neighbor bootstrap method based upon k-nearest neighbors, KNN, to do the same task (synthetic time series generation). In the KNN approach, simulated streamflow is limited to be from the set of historic flows observed, but the variance of the historic sequence is preserved. In the NP1 approach streamflow values different from historic observations are obtained due to the kernel smoothing of the conditional probability distribution between observations. However, this is at the cost of inflating the variance slightly. Tarboton, Sharma, and Lall (1998) applied kernel nonparametric methods to the simulation of disaggregate streamflow (e.g. monthly or subbasins) given time series of aggregate streamflow (e.g. annual or basin aggregate). These authors argue that nonparametric methods are more flexible than the parametric models used previously in stochastic hydrology because they have the capability to capture nonlinearity, skewness, bimodality and asymmetric dependence structures.

Reconstruction of low-order nonlinear dynamics from time series of a state variable has been an active area of research in hydrology. There have been many works on forecasting the Great Salt Lake volumes and levels. Asefa et al. (2005) studied the GSL biweekly time series and applied the Support Vector Machines (SVM) method to forecast future values. The SVM method (Vapnik, 1995) is a

method that searches for solutions of differential equations that are responsible for generation of the single time series. This solution involves investigation of nonlinearity (chaos) by re-projecting (unfolding) the dynamics through representation of the data in multi-dimensional state space. The SVM method is optimized by minimizing a risk function on a generalized error (risk) measure, rather than just mean square error over a training set. Asefa et al. (2005) forecasted the GSL volume time series by splitting it to wet and dry periods. The selected dry period of their study was five years (1924-1929), while the wet period was during the major rise of the GSL (1983-1987). Asefa et al. (2005) presented SVM as an appropriate tool able to forecast the GSL dry period (4 month prediction) as well as the wet period (2 weeks prediction). Their core point to get a good forecast was estimating an appropriate imbedding dimension, d, and time delay, τ to represent the nonlinear dynamics in the GSL volume time series.

2.2. Spectral and Nonlinear Systems Analysis

Various authors have applied Spectral Analysis (Vautard, Yiou, and Ghil, 1992) to the analysis of time series. Macdonald (1989) suggested the uses of spectral peak identification for analyzing the time series periodogram. Lall and Mann (1995) implemented spectral peak identification for the GSL biweekly time series. They develop an empirical understanding of the role of climatic variability in the dynamics of the Great Salt Lake (GSL) of Utah. The goal of their work (Lall and Mann, 1995) was to relate the spectral peaks in GSL volume and driving inputs, namely

precipitation, streamflow, and temperature, to the spectra of climate indices such as the El Niño Southern Oscillation (ENSO) index. Lall and Mann's (1995) analysis of the Great Salt Lake monthly volume change data from 1847-1992 reveals decadal and interdecadal signals. The identified decadal and interdecadal signals appear to be consistent with ENSO.

Moon (1995) and Moon and Lall (1996) studied the relationships between the time variability of the volume of GSL and selected atmospheric circulation indices. Moon (1995) developed and applied nonlinear measures of dependence between selected atmospheric circulation indices and the GSL volume at various lags (presuming that these indices are considered to lead the GSL volume). In addition, he forecasted the volume of the GSL using selected atmospheric circulation indices. The indices considered in his study were the Southern Oscillation Index (SOI), The Pacific/North America (PNA) climatic pattern, and the Central North Pacific (CNP) climatic pattern.

Investigations of the GSL time series (Abarbanel et al., 1996,Lall, Sangoyomi, and Abarbanel, 1996,Mann, Lall, and Saltzman, 1995) suggest that it is one of a few geophysical series whose dynamics can be described by a low dimensional nonlinear model with limited predictability. In order to demonstrate the relationship between structured low-frequency climate variability, low-order dynamical behavior of the GSL and the enhanced long term predictability of the GSL volume Abarbanel et al. (1996) examined a long climatological record of measurements of the volume of the GSL in Utah. They use the Global False Nearest

Neighbors method to choose the embedding dimension d appropriate for describing the GSL volume in multivariate state space. They (Abarbanel et al., 1996) found that an embedding dimension of 4 is sufficient to describe the GSL volume time series, suggesting that there are four degrees of freedom active in the Great Salt Lake volume record. Abarbanel et al. (1996) findings provide direct insight into the prediction of the GSL volume.

Abarbanel et al. (1996) also suggested that physically based models of climate that are guided by low frequency spatial and temporal features observed in data and reproduce the dynamical attributes of the corresponding time-series may be more useful for analysis climate changes issues than high resolution models that lack such guidance. In this regard long time-series such as that of the GSL volume that represents a spatially averaged hydro-climate may provide a useful baseline. Abarbanel et al. (1996) analyzed the GSL volume time series, western U.S. precipitation, northern hemisphere sea level pressure and air temperature using multivariate spectral analysis to get the interannual and decadal signals. They identified signals that represent 2 year, 3-5 year, 10-12 year, and 15-20 year intermittent oscillations with slowly varying amplitude and phase characteristics. They argued that the GSL volume responds with a small phase lag to regional precipitation and temperature anomalies, which are in turn forced by large-scale atmospheric circulation anomalies.

Shun and Duffy (1999) studied the precipitation (P), temperature (T) and runoff (R) on the Wasatch Front in northern Utah. These quantities are inputs to the

GSL basin hydrologic system. Shun and Duffy (1999) identified coherent patterns (oscillatory components) of annual, interannual, and decadal oscillations in precipitation, temperature, and runoff from point observations using a space-time form of principle components analysis called Multi-channel Singular Spectrum Analysis (Plaut and Vautard, 1994) and discussed these components in terms of the hydrologic and hydrogeologic processes contributing to streamflow across the Wasatch Front. Multi-channel Singular Spectrum Analysis results from Shun and Duffy (1999) show that the variance contribution for P, R, T at all altitudes is dominated by the annual oscillations and harmonics, precipitation shows significant but weak interannual and decadal oscillations, and runoff exhibits strong interannual and decadal oscillations. Their analysis (Shun and Duffy, 1999) qualitatively links amplified low-frequency oscillations to large-scale groundwater and base flow.

2.3. Regional Climate Trends

The Great Salt Lake basin is snowmelt dominated like many of the basins in the western United States. Regonda et al. (2005) analyzed streamflow, snow mass, temperature, and precipitation in snowmelt-dominated river basins in the western United States. They found that significant declines in monthly snow water equivalent (SWE), and increases in winter precipitation are evident for many stations in the western United States. The largest declines are occurring in the Pacific Northwest region, the northern parts of Idaho, Utah, Wyoming, and the Sierra Nevada region. In addition, they found an indication of an advance in the timing of

peak spring season flows over the past 50 years. They argued that the trends in SWE can be influenced by both temperature and precipitation. They added to their findings that during recent decades more precipitation is coming as rain rather than snow.

Trends in climate are seen in several global variables. Cayan et al. (2001) documented the early onset of spring in the western United States by examining changes in the blooming of plants (lilac and honeysuckle bushes) and the timing of spring snowmelt pulses. McCabe and Wolock (2002) observed a step increase in streamflow in the conterminous United States over the period 1941-99, with pronounced increases in the eastern United States after 1970. Aguado et al. (1992) and Dettinger and Cayan (1995) reported that increasing winter temperature, as observed in several parts of the western United States, reduces the amount of snow in a basin (e.g., more precipitation falling as rain than snow). Mote (2003) studied trends of SWE in the Pacific Northwest and observed strong declines in 1 April SWE, in spite of increases in precipitation, which is consistent with an increase in spring temperature. Mote et al. (2005) extends the Mote (2003) study by incorporating the entire Western US from the Continental Divide to the pacific, and from central British Columbia, Canada, south to southern Arizona and New Mexico. In addition, they augment the long-term monthly manual observations of snow with a more recent dataset of daily-telemetered snow observations. Moreover, they corroborate the analysis of snow data using a hydrological model (the Variable Infiltration Capacity model, VIC; Liang et al., 1994) with observed daily temperature and

precipitation data. Their findings matched the previous work presented earlier in this review. Widespread declines in spring time SWE have occurred in much of the North American West over the period 1925-2000, especially since mid-century (Aguado et al., 1992,Cayan et al., 2001,Mote, 2003,Regonda et al., 2005).

2.4. Great Salt Lake Evaporation

The rate of evaporation from a water surface is a function of local meteorological conditions, the temperature, and the salinity of the water surface (Harbeck, Kohler, and Koberg, 1958,Sturrock, 1978,Brutsaert, 1982). Several factors affect evaporation from free water surfaces. Molecular activity increases with temperature hence at higher water temperature there is a greater tendency for the emission of vapor from the water surface to the atmosphere. This is reflected by an increase in the saturation vapor pressure in the boundary layer immediately above the water surface. The transport of water vapor away from the surface, due to atmospheric turbulence is proportional to the difference between the pressure of saturated vapor at the water surface and the vapor pressure of the air.

The molecular activity of water is reduced as its salinity increases because molecules of dissolved solids interfere with the motion of water molecules (Stumm and Morgan, 1981). In addition, the average number of water molecules in contact with the air becomes smaller as salinity increases because salt molecules occupy part of the surface area. These effects combine to reduce the saturation vapor pressure over a saline water surface relative to a fresh water surface. The effect of salinity on

evaporation is important for water balance computations and other engineering studies related to saline terminal lakes (e.g. evaporation ponds used to dispose of saline industrial effluents, salt production ponds, and the newly emerging technology of salt gradient solar ponds).

Evaporation from saline waterbodies was studied by Rohwer (1933), Adams (1934), Young (1947), Bonython (1966), Turk (1969,1970), Salhotra (1986,1987), and Salhotra, Adams, and Harleman (1985,1992). Turk (1969,1970) studied the hydrology of salt flats and established relative evaporation rates, under field conditions, for brines from Bonneville (GSL) containing various amounts of dissolved solids. He noted that evaporation rates of the brines whose average specific gravities varied from 1.207 to 1.333 ranged from 70% to 9.5% of the fresh water evaporation rates, respectively. Turk's (1969,1970) findings were consistent with earlier comparisons (Dickson, Yepsen, and Hales, 1965) between saturated vapor pressures over several Great Salt Lake brines and saturated vapor pressures over freshwater. Adams (1934) described approximately the same decline in evaporation rates for Great Salt Lake brine. Bonython (1966) presented evaporation measurements conducted in South Australia from two thermally insulated pans over a period of two consecutive summers. One pan contained water and the other brine with density varying from 1.07 to 1.245 g/cm^3. In each of the above studies, evaporation results were presented as the ratio of salt-water evaporation to fresh-water evaporation. This ratio is a function of the salinity or the density of the solution.

Salhotra, Adams, and Harleman (1985) used pan evaporation data to evaluate the effect of salinity and water chemistry on evaporation. They collected data from eight evaporation pans containing brines of different salinity and ionic composition from the Dead Sea and analyzed them in order to quantify the effect of salinity on evaporation. They argued that the common approach to account for the salinity effects based on ratios of salt water to fresh water evaporation rates is hard to use accurately because these ratios are also functions of the saline ionic compositions and the metrological variables over salt waters. They suggested that a better, more general method, is to use the saturated vapor pressure of the water surface as a function of the brine's ionic composition. This method also has the advantage that it can estimate evaporation rates for solutions involving several salts.

Salhotra (1987) mentioned that the computation of evaporation from a saline water body should implicitly or explicitly include both the salinity and the temperature feedback effects. The temperature feedback is related to the thermal energy budget of a freshwater body and a saline water body exposed to identical meteorological forcings. Lower vapor pressure over saline water permits less energy to escape as latent heat, thus causing an increase in temperature within the saline water body in relation to that of the freshwater body. This increase in temperature results in increases in saturation vapor pressure and enhances the rate of evaporation from the saline water body, partially compensating for the reduction in evaporation due to salinity. The salinity feedback effect as discussed in Salhotra, Adams, and Harleman (1985) is based on the feedback between salinity, ionic concentration,

saturation vapor pressure and evaporation from a lake surface. Evaporation removes water molecules from the lake surface, resulting in increased concentrations of salt ions, which reduces the vapor pressure and thereby reduces the evaporation. The increased salt ion concentration near the surface induces a salinity gradient into the lake that drives diffusive transport of salt into the lake. The evaporation rate that results is a balance of the salt diffusion into the lake and Dalton type vapor pressure gradient driven diffusion of water vapor away from the lake surface into the atmosphere.

From the previous discussion, we learn that in order to model the GSL dynamics we ought to compute the lake's output evaporation using the ionic composition of GSL brine as well as the lake temperature to incorporate the salinity and temperature feedback effects. This contribution of salinity towards evaporation will be useful in modeling the Great Salt Lake and thereby contributing to understanding of surface hydrology of the whole system that drains to the GSL.

CHAPTER 3

DATA EXPLORATION

The study area is divided into five geographic sub areas (Bear watershed, Weber watershed, Jordan/Provo watershed, Near West Desert watershed, and Great Salt Lake) as shown in Figure 1-2. Table 3-1 summarizes the data that has been used in this study. The time step for these datasets is generally one month, using month's end values. Figure 3-1 gives a map of the Ion concentration sampling sites, streamflow gages, and SNOTEL sites in the Great Salt Lake Basin that were used.

Precipitation, temperature, and wind speed datasets were obtained from the Surface Water Modeling group at the University of Washington. They are presented in gridded format (http://www.hydro.washington.edu/Lettenmaier/gridded_data/). The development of this gridded dataset is described by (Maurer et al., 2002). These datasets provided us with monthly 1/8-degree resolution gridded meteorological data for 1 Jan 1949 - 31 Jul 2000. The Maurer et al. (2002) data is available for the contiguous United States as well as Mexico and Canada grouped by USGS regions. We extracted data for our five geographic sub areas from the Great Basin region dataset. Precipitation, wind speed, and temperature time series were calculated as monthly average time series over each geographic sub area. The Appendix shows a cross comparison of this data with gage data as a spot check on the reliability of this dataset.
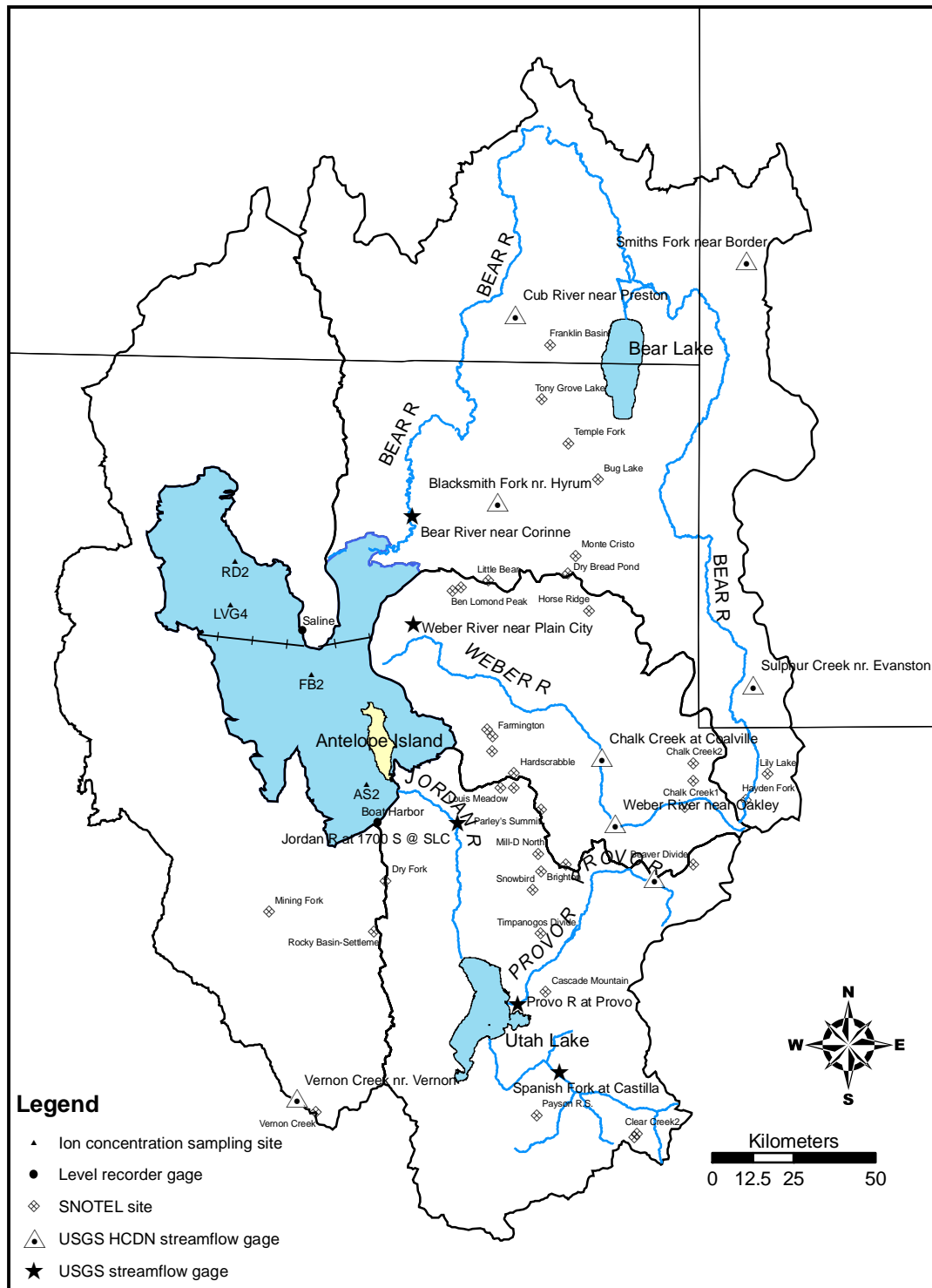
Figure 3-1.   The Great Salt Lake Basin monitoring sites.

Free-of-controls streamflow datasets, which are specifically suitable for the study of surface-water conditions throughout the United States under fluctuations in the prevailing climatic conditions, were found from Hydro-Climatic Data Network (HCDN) (Slack, Lumb, and Landwehr, 1993).

The Bear watershed has four HCDN stations. These are Blacksmith Fork (USGS #10113500), Smiths Fork near Border (USGS #10032000), Cub River near Preston (USGS #10093000), and Sulphur Cr near Evanston (USGS #10015700). In addition, the long-term stream gage where the Bear River enters the GSL, the Bear River at Corrine (USGS #10126000) which is not a HCDN station was used to quantify the aggregate outflow from the Bear River. This streamflow gage (Bear River at Corrine, USGS #10126000) has some missing data (1957-1963) that we filled using regression against the nearby station Bear River near Collinston, UT (USGS # 10118000).

The Weber watershed has two HCDN stations. These are Chalk Creek at Coalville (USGS #10131000), and Weber River at Oakley (USGS #10128500). These were both used in this study. In addition, the long-term gage near where the Weber River enters GSL, the Weber River near Plain city (USGS #10141000) was used to quantify the aggregate outflow from the Weber River.

The Jordan/Provo watershed has two HCDN stations North Fork Provo River near Kamas (USGS #10153800) and Red Butte Creek at Fort Douglas near SLC (USGS #10172200). In this study, we chose to use only North Fork Provo River near Kamas because Red Butte Creek at Fort Douglas has a very small drainage area

(7.25 sq. miles). In the Jordan/Provo watershed we also used the following non-HCDN stations: Jordan River at 1700 south at SLC (USGS #10171000), Provo River at Provo (USGS #10163000), and Spanish Fork at Costilla (USGS #10150500). The Provo River at Provo gage and Spanish Fork at Costilla gage were chosen because they both have long-term records and they capture the main tributary inflows into Utah Lake. The Jordan River at 1700 south at SLC, which is impacted by regulation of Utah Lake, has a long-term record and captures the inflow to the GSL from the outflow of Utah Lake. The Near West Desert watershed has no perennial rivers draining to the GSL. There is one HCDN station in this watershed, Vernon Creek near Vernon (USGS #10172700) which was used (Table 3-1).

Snow water equivalent (SWE) datasets were obtained form the Natural Resources Conservation Service (NRCS) automated SNOTEL system (http://www.wcc.nrcs.usda.gov/snotel/Utah/utah.html). All SNOTEL sites in the Bear, Weber, Jordan / Provo, and Near West Desert geographic sub-areas were used in this study. An average time series of end of month SWE values in each sub geographic sub area was calculated by averaging the individual SNOTEL station end of month values. These averages were adjusted to account for bias due to different lengths of record at sites that have differing average SWE. The adjustment procedure is illustrated in Figure 3-2 for four stations ranked by their period of record. Stations S1 and S2 have periods of record from year n1=n2 to present, p. Station S3 has period of record from n3>n2 to present, p and station S4 has period of record from n4>n3 to present, p. Stations S1 and S2 have full records, but S3 has a

shorter record and S4 the shortest, in this illustrative example. For each year the unadjusted average is simply the mean across all stations with data. Thus the unadjusted average in year i is represented by:

$U(i)=Ave(S(1:4,i))$ for i ranging from n4:p

$U(i)=Ave(S(1:3,i))$ for i ranging from n3:(n4-1)

$U(i)=Ave(S(1:2,i))$ for i ranging from n2:(n3-1) (recalling that n1=n2)

where Ave(.) denotes averaging and S(s,y) denotes the specific end of month snow water equivalent values for a station (or range or stations), s, and year, y and the unadjusted average in year i is denoted by U(i).

The adjusted average for the year i will be denoted by X(i). For the years n4 to p, no adjustments are needed so we have:

$X(i)=U(i)$ i in n4:p

For the years n3 to n4-1, i.e. the years when S4 does not have a record, the adjusted average is calculated as:

$X(i)=Ave(S(1:3,i))*Ave(S(1:4,n4:p))/Ave(S(1:3,n4:p))$

$=U(i)*Ave(X(n4:p))/Ave(S(1:3,n4:p))$ i in n3:(n4-1)

Similarly, the adjusted average for the year i in the range n2 to n3-1, i.e. the years when S3 and S4 do not have records, is calculated as:

$X(i)=U(i)*Ave(X(n3:p))/Ave(S(1:2,n3:p))$ i in n2:(n3-1)

Table 3-1.   Datasets used in the study

1. Bear watershed						
	Source	Type	Observed Record	Identification	No. of Grids	Comment
Precipitation **Air Temperature** **Wind speed**	Univ. of Washington[a]	Gridded	Jan 1949 – Jul 2000	Great Basin	137	Monthly average Dataset
Streamflow	HCDN[b]	Gage	Oct 1913 – Sept 2003;	USGS #10113500, Blacksmith Fork;	---	Drainage area 263 mi^2;
			Oct 1942 – Sept 2003;	USGS #10032000, Smiths Fork near Border;		Drainage area 165 mi^2;
			Oct 1940 – Sept 1986;	USGS #10093000, Cub River Near Preston;		Drainage area 31.6 mi^2;
			Oct 1957 – Sept 1997;	USGS #10015700, Sulphur Cr;		Drainage area 64.2 mi^2;
	USGS[c]		Oct 1949 – Sept 2003	USGS #10126000, Bear River Near Corinne		Drainage area 7029 mi^2
Snow Water Equivalent	Snotel[d]	Site	Oct 1978 – Sept 2004	Tony Grove Lake, Bug Lake, Franklin Basin, Hayden Fork, Lily Lake, Little Bear, Monte Cristo, Dry Bread Pond, Temple Fork	---	Daily Dataset, 9 stations
2. Weber watershed						
	Source	Type	Observed Record	Identification	No. of Grids	Comment
Precipitation **Air Temperature** **Wind speed**	Univ. of Washington	Gridded	Jan 1949 – Jul 2000	Great Basin	42	Monthly average Dataset
Streamflow	HCDN	Gage	Oct 1927 – Sept 2003;	USGS #10131000, Chalk Creek at Coalville;	---	Drainage area 250 mi^2;
			Oct 1904 – Sept 2003;	USGS #10128500, Weber River Near Oakley		Drainage area 162 mi^2;
	USGS		Oct 1907 – Sept 2003	USGS #10141000, Weber River near Plain City		Drainage area 2081 mi^2
Snow Water Equivalent	Snotel	Site	Oct 1978 – Sept 2004	Farmington, Horse Ridge, Ben Lomond Peak, Ben Lomond Trail, Chalk Creek1, Chalk Creek2, Parley's Summit, Smith & Morehouse, Hardscrabble, Thaynes Canyon, Parrish Creek, Farmington Lower	---	Daily Dataset, 12 stations

[a] http://www.hydro.washington.edu/Lettenmaier/gridded_data/index.html
[b] Hydro-Climatic Data Network--(http://water.usgs.gov/pubs/wri/wri934076/region16.html)
[c] The U.S. Geological Survey—(http://nwis.waterdata.usgs.gov/ut/nwis/sw)
[d] National Water and Climate Center—(http://www.wcc.nrcs.usda.gov/snotel/Utah/utah.html)

Table 3-1.   Continued

3. Jordan/ Provo watershed						
	Source	Type	Observed Record	Identification	No. of Grids	Comment
Precipitation **Air Temperature** **Wind speed**	Univ. of Washington	Gridded	Jan 1949 – Jul 2000	Great Basin	68	Monthly average Dataset
Streamflow	HCDN	Gage	Oct 1963 – Sept 1996;	USGS #10153800, North Fork Provo River near Kamas, UT;	---	Drainage area 24.4 mi^2;
	USGS		Oct 1903 – Sept 2003;	USGS #10163000, Provo River at Provo UT;		Drainage area 673 mi^2;
			Oct 1919 – Sept 2003;	USGS #10150500, Spanish Fork at Castilla, UT;		Drainage area 652 mi^2;
			Oct 1942 – Sept 2003	USGS #10171000, Jordan River at 1700 South at SLC		Drainage area 3438 mi^2
Snow Water Equivalent	Snotel	Site	Oct 1978 – Sept 2004	Payson R.S., Brighton, Clear Creek1, Clear Creek2, Beaver Divide, Mill-D North, Snowbird, Timpanogos Divide, Dry Fork, Lookout Peak, Louis Meadow, Cascade Mountain	---	Daily Dataset, 12 stations
4. Near West Desert watershed						
	Source	Type	Observed Record	Identification	No. of Grids	Comment
Precipitation **Air Temperature** **Wind speed**	Univ. of Washington	Gridded	Jan 1949 – Jul 2000	Great Basin	100	Monthly average Dataset
Streamflow	HCDN	Gage	Oct 1907 – Sept 2003	USGS #10172700, Vernon Creek near Vernon	---	Drainage area 25 mi^2
Snow Water Equivalent	Snotel	Site	Oct 1978 – Sept 2004	Rocky Basin-Settleme, Mining Fork, Vernon Creek	---	Daily Dataset, 3 stations
5. Great Salt Lake						
	Source	Type	Observed Record	Identification	No. of Grids	Comment
Precipitation **Air Temperature** **Wind speed**	Univ. of Washington	Gridded	Jan 1949 – Jul 2000	Great Basin	36	Monthly average Dataset
Lake level North	UGS[e]	Gage	Apr 15 1966 – Jul 15 2004	USGS #10010100 Great Salt Lake Near Saline, UT	---	The Great Salt Lake is divided by the railroad causeway (1959) into two arms
South			Oct 18 1847 – Jul 15 2004	USGS #10010000 Great Salt Lake at Saltair Boat Harbor, UT	---	

[e] Utah Geological Survey

Table 3-1.   Continued

5. Great Salt Lake							
		Source	Type	Observed Record	Identification	No. of Grids	Comment
Lake level	Average	USGS[f]	table	Apr 15 1966 - Jul 15 2004	Table A1, page A-3[g]	---	The entire lake level was interpolated using the area weight method
Lake Volume	North	USGS	table	Apr 15 1966 - Jul 15 2004	Table A1, page A-3	---	Interpolated
	South			Oct 18 1847 - Jul 15 2004		---	
	Total			Oct 18 1847 - Jul 15 2004	---	---	Summing the north and south arms volumes
Lake Area	North	USGS	table	Apr 15 1966 - Jul 15 2004	Table A1, page A-3	---	Interpolated
	South			Oct 18 1847 - Jul 15 2004		---	
	Total			Oct 18 1847 - Jul 15 2004	---	---	Summing the north and south arms areas
Lake Salinity	North	UGS	Site	Jul 1967 - Mar 2003	USGS sites in north Arm (LVG4,RD2)	---	irregular time series, various depths provided
	South			Jun 1966 - Feb 2004	USGS sites in South Arm (AS2,FB2)	---	
Lake Temperature	North	UGS	Site	Jul 1967 - Mar 2003	USGS sites in north Arm (LVG4,RD2)	---	
	South			Jun 1966 - Feb 2004	USGS sites in South Arm (AS2,FB2)	---	

[f] U.S. Geological Survey
[g] Loving, B. L., K. M. Waddell and C. W. Miller. 2000. Water and Salt Balance of Great Salt Lake, Utah, and Simulation of Water and Salt Movement through the Causeway, 1987-98. Water-Resources Investigations Report, 00-4221. U.S. Geological Survey, 2000, Salt Lake City, Utah, p.32.
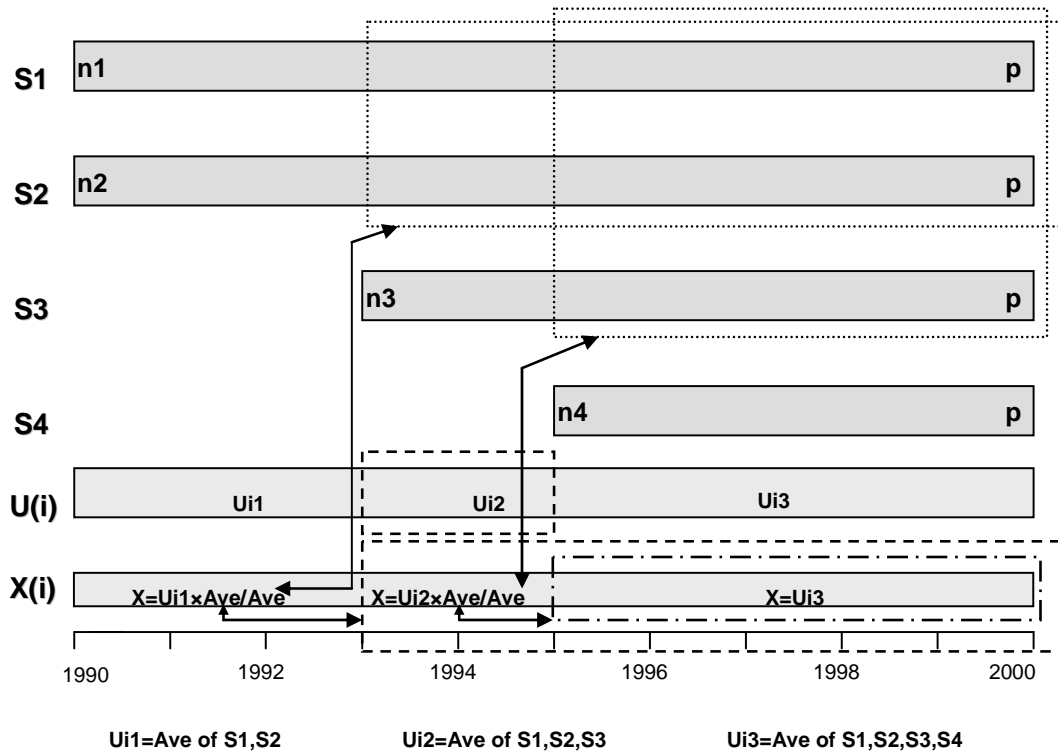
Figure 3-2.   Illustration of the adjustment procedure used in calculating an average
time series of end of month SWE values in each sub geographic area.
Four stations (S1, S2, S3, and S4) with varying length of record over
the interval (1990-2000) are used for illustrative purpose.

The GSL level dataset (10/18/1847 to 7/15/2004) was obtained from the Utah

Geological Survey (UGS).   As indicated in Table 3-1 the GSL north arm level is

monitored with the Great Salt Lake near Saline (USGS # 10010100) and the south

arm level is monitored with the Great Salt Lake at Saltair Boat Harbor (USGS #

10010000) gages. For these two north and south sites, separate records of the GSL's

level are available since April 15, 1966. During the late 1980s, rapidly rising lake

levels made it necessary for the USGS to relocate the Boat Harbor gage several times.

As the gage was relocated, new benchmarks had to be chosen to reference the gage's datum, because previously used benchmarks were submerged by the rising lake. The use of new benchmarks necessitated the correction of lake level records. For this study, we obtained the most recent corrected levels for the GSL north and the south arms from the USGS (http://ut.water.usgs.gov/gsl%20corr/gslcorrection.htm).

Figures 3-3 to 3-6 depict average monthly temperature, monthly precipitation, annual runoff, wind speed, and adjusted basin average month end snow water equivalent time series for the Bear, Weber, Jordan/Provo, and Near West Desert watersheds. Adjusted basin average month end snow water equivalent was calculated using the method discussed in Figure 3-2 earlier. Figures 3-3 to 3-6 also show seasonal subseries plots (Becker, Chambers, and Wilks, 1988) of the monthly change in adjusted basin average snow water equivalent. A seasonal subseries plot groups the values for a particular month and plots them separately as subseries in the plot for each month. For example in Figure 3-3f the squiggly line above October gives the change in snow water equivalent from the end of September to the end of October for all the years of record (1979-2000). The straight line above each month gives the average across the years of the change in Snow Water Equivalent from the end of September to the end of October. In these figures the positive changes during October to February indicate snow accumulation, while the negative changes in March and later indicate snowmelt. Figure 3-7 gives average monthly air temperature, monthly precipitation and wind speed over the Great Salt Lake.

The Great Salt Lake's volume and area values were interpolated from measured water-surface levels using area-volume data provided by the USGS (Loving, Waddell, and Miller, 2000) given in Figure 3-8. This was done separately for the north and south arms following the separation of the lake into two arms by the railroad causeway in 1959. Figure 3-9 shows the Great Salt Lake's levels, volumes, and areas.

Figure 3-1 shows four sites in the lake where salinity and water temperature data have been collected by the Utah Geological Survey (UGS). These UGS sites are RD2 and LVG4 in the north arm and FB2 and AS2 in the south arm. Due to the intermittent measurements and length of data available, we used some approximations for this study. Figure 3-10 gives times series of salinity and its chemical composition for the GSL at the four sites (RD2, LVG4, FB2, and AS2). The two ions with highest ionic composition percentages are Chlorine (Cl) and Sodium (Na). Figure 3-11 gives measurements of lake temperature at different depths measured at the same time as salinity at four sites (RD2, LVG4, FB2, and AS2).
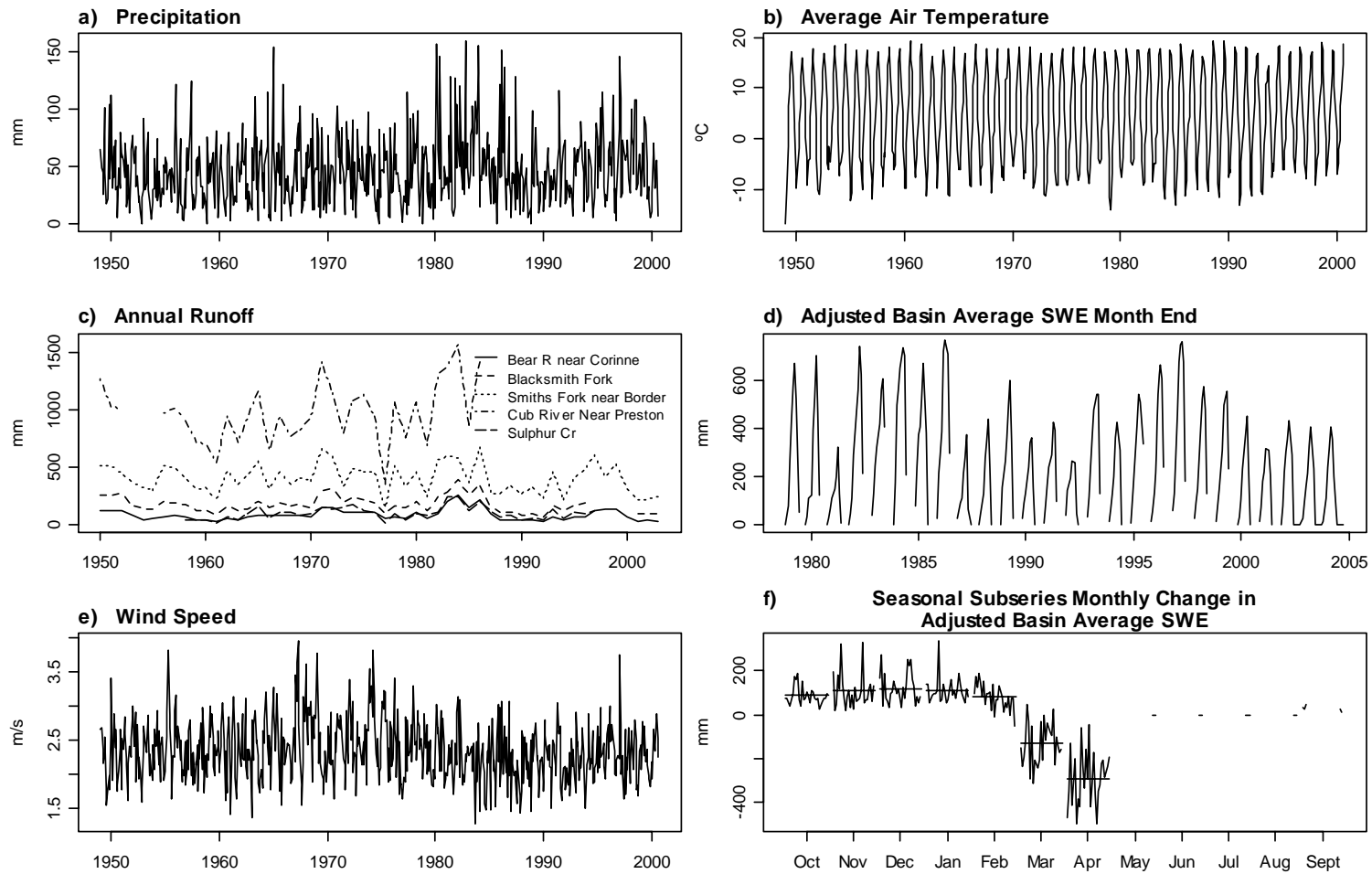
Figure 3-3. Bear watershed's (a) monthly precipitation, (b) monthly average air temperature, (c) annual runoff at five gage, (d) adjusted basin average month end SWE of nine SNOTEL stations, (e) monthly average wind speed and (f) seasonal subseries monthly change in adjusted basin average SWE.
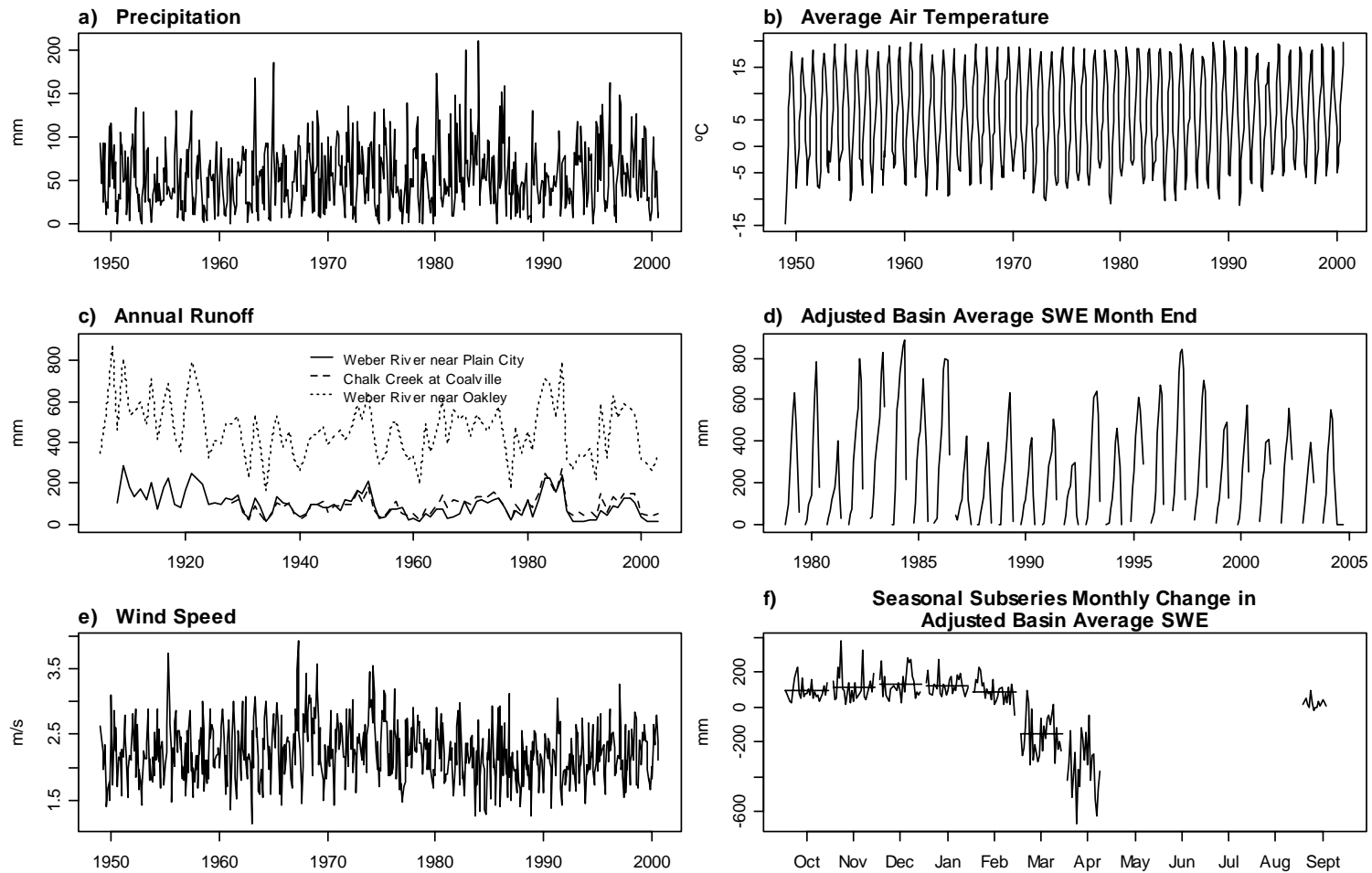
Figure 3-4.   Weber watershed's (a) monthly precipitation, (b) monthly average air temperature, (c) annual runoff at three gages, (d) adjusted basin average month end SWE of twelve SNOTEL stations, (e) monthly average wind speed and (f) seasonal subseries monthly change in adjusted basin average SWE.
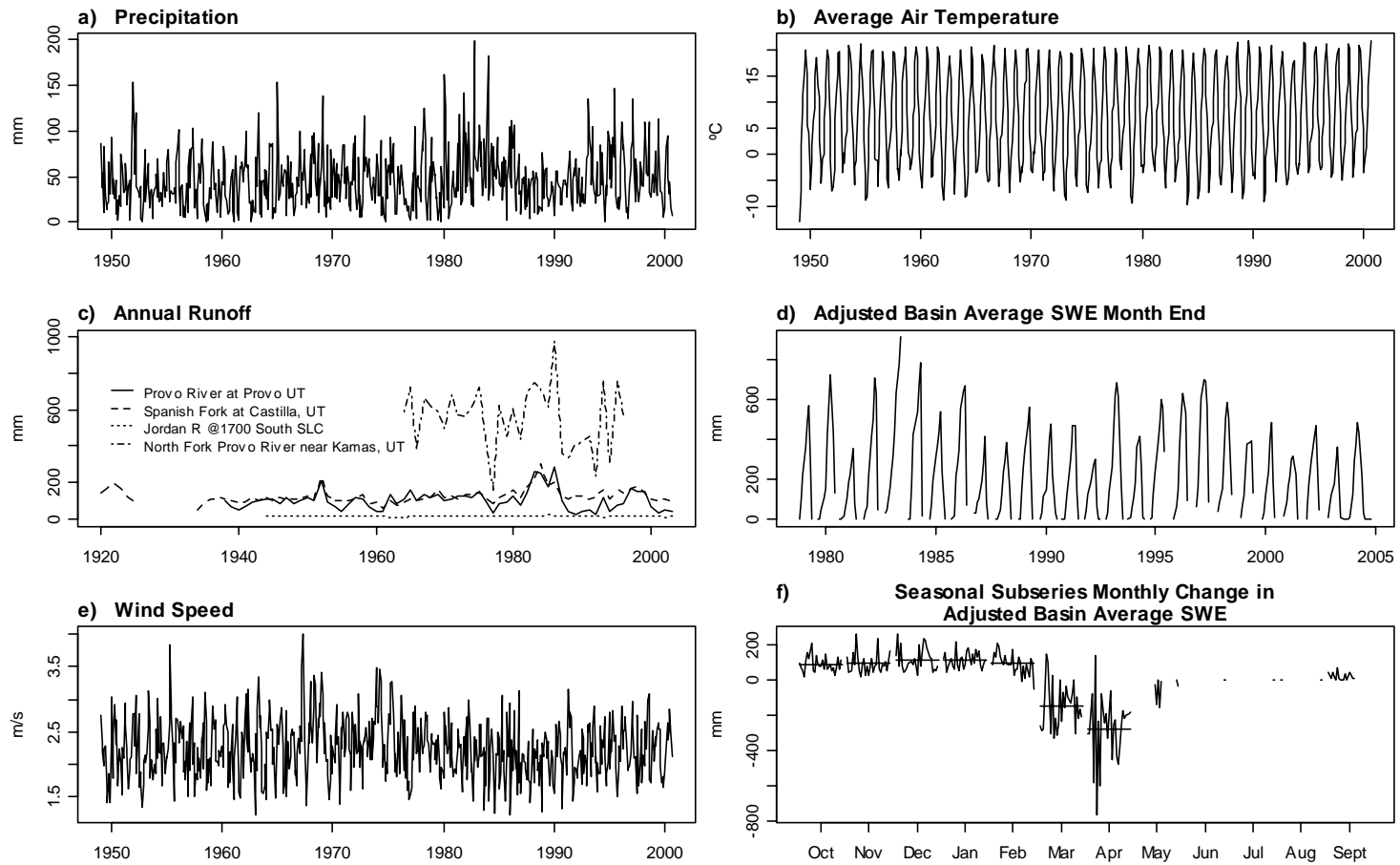
Figure 3-5.   Jordon/Provo watershed's (a) monthly precipitation, (b) monthly average air temperature, (c) annual runoff at four gages, (d) adjusted basin average month end SWE of twelve SNOTEL stations, (e) monthly average wind speed and (f) seasonal subseries monthly change in adjusted basin average SWE.
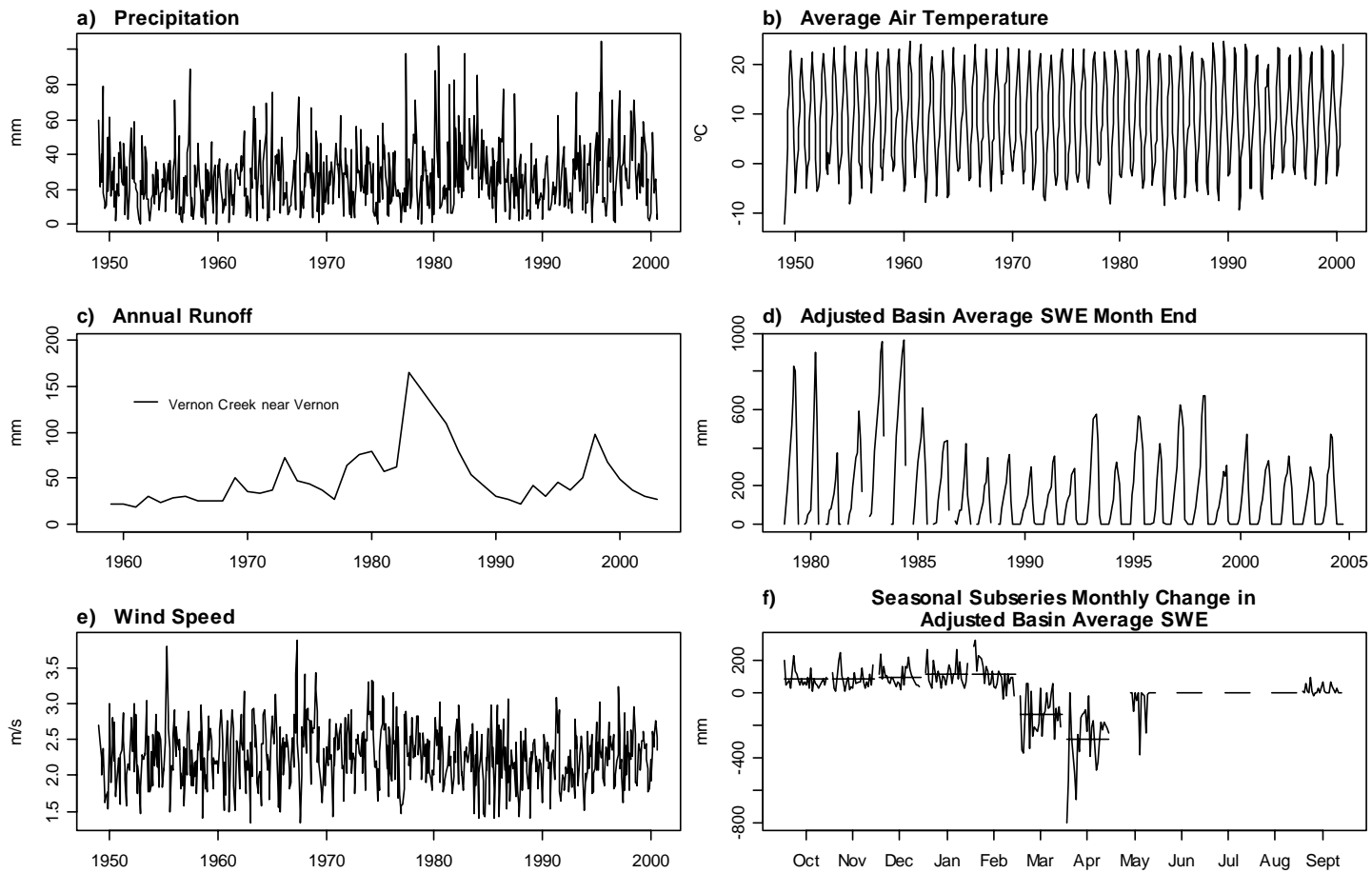
Figure 3-6.   West Desert watershed's (a) monthly precipitation, (b) monthly average air temperature, (c) annual runoff at HCDN gage, (d) adjusted basin average month end SWE of three SNOTEL stations, (e) monthly average wind speed and (f) seasonal subseries monthly change in adjusted basin average SWE.
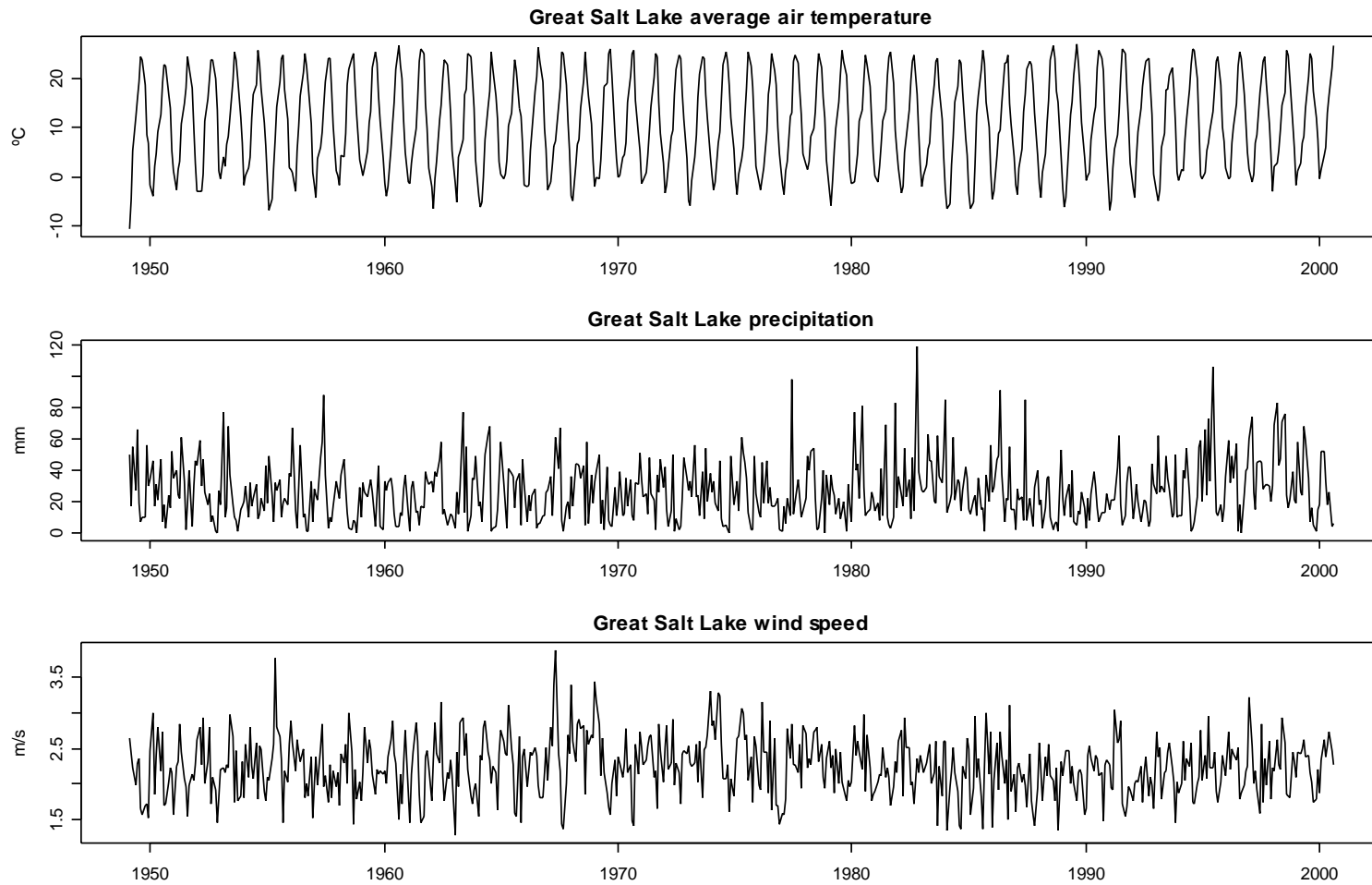
Figure 3-7. Time series of monthly average air temperature, monthly precipitation, and wind speed over the Great Salt Lake.
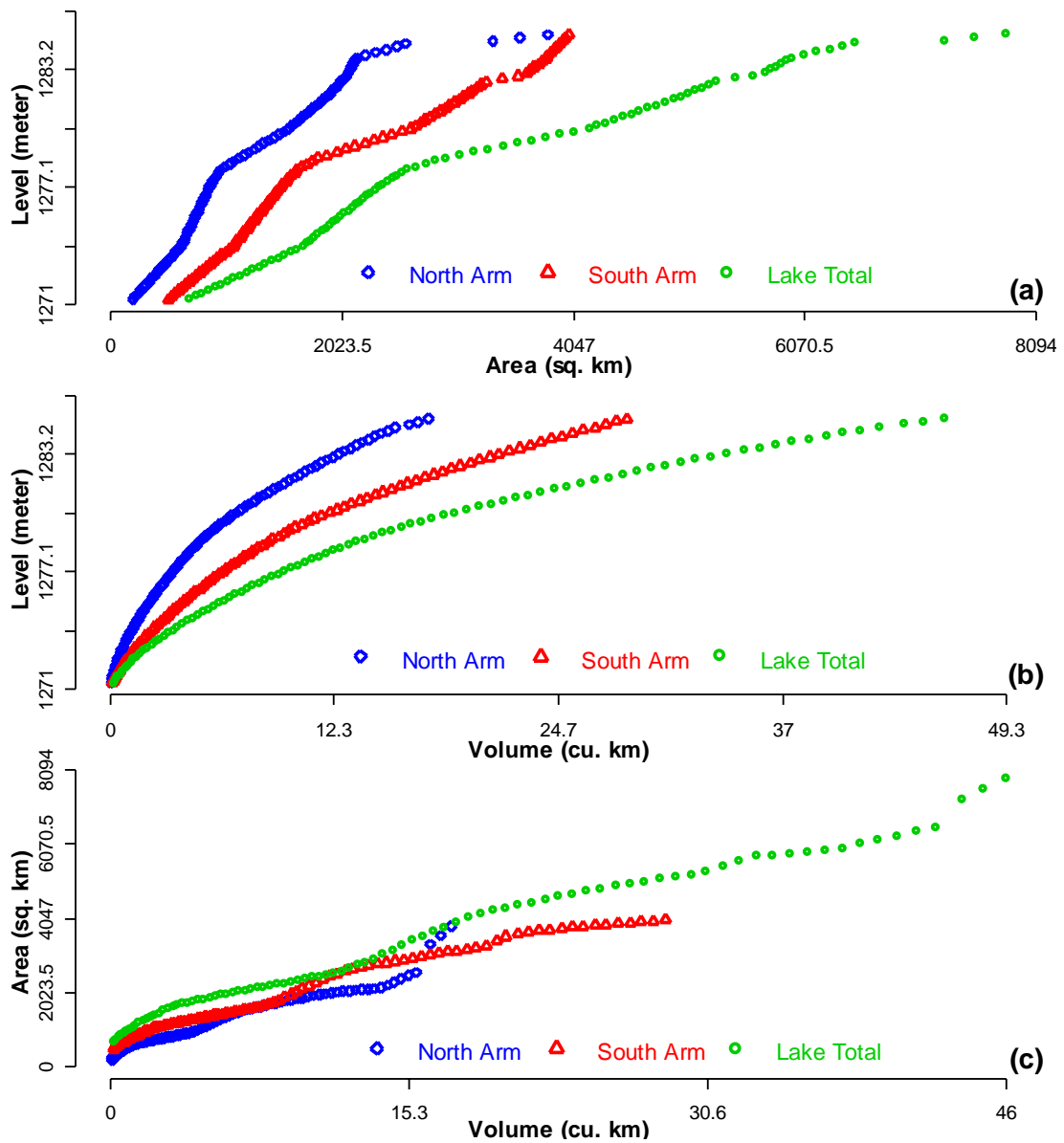
Figure 3-8.   The Great Salt Lake's bathymetry. (a) Area – Level (above mean sea level), (b) Volume – Level (above mean sea level), and (c) Volume - Area relationships. Data from Loving, Waddell and Miller (2000) table A-1.
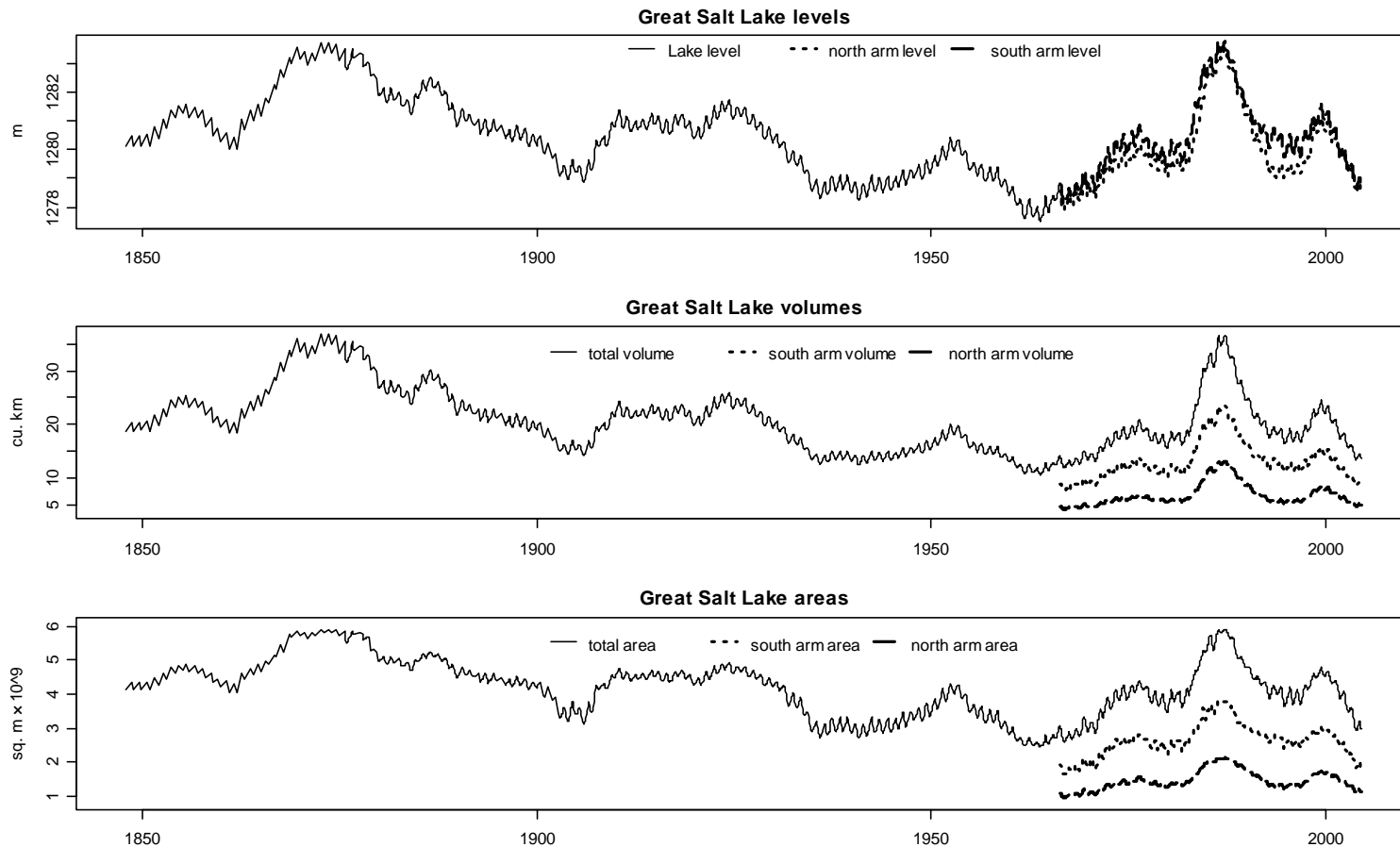
Figure 3-9.   Time series of levels, volumes, and areas for Great Salt Lake. GSL level has been monitored since 1847. The lake was divided by a railroad causeway in 1959. Separate north and south arms records are available since 15th April, 1966. Volumes and areas of GSL were interpolated from measured bathymetric area-volume data provided by USGS.
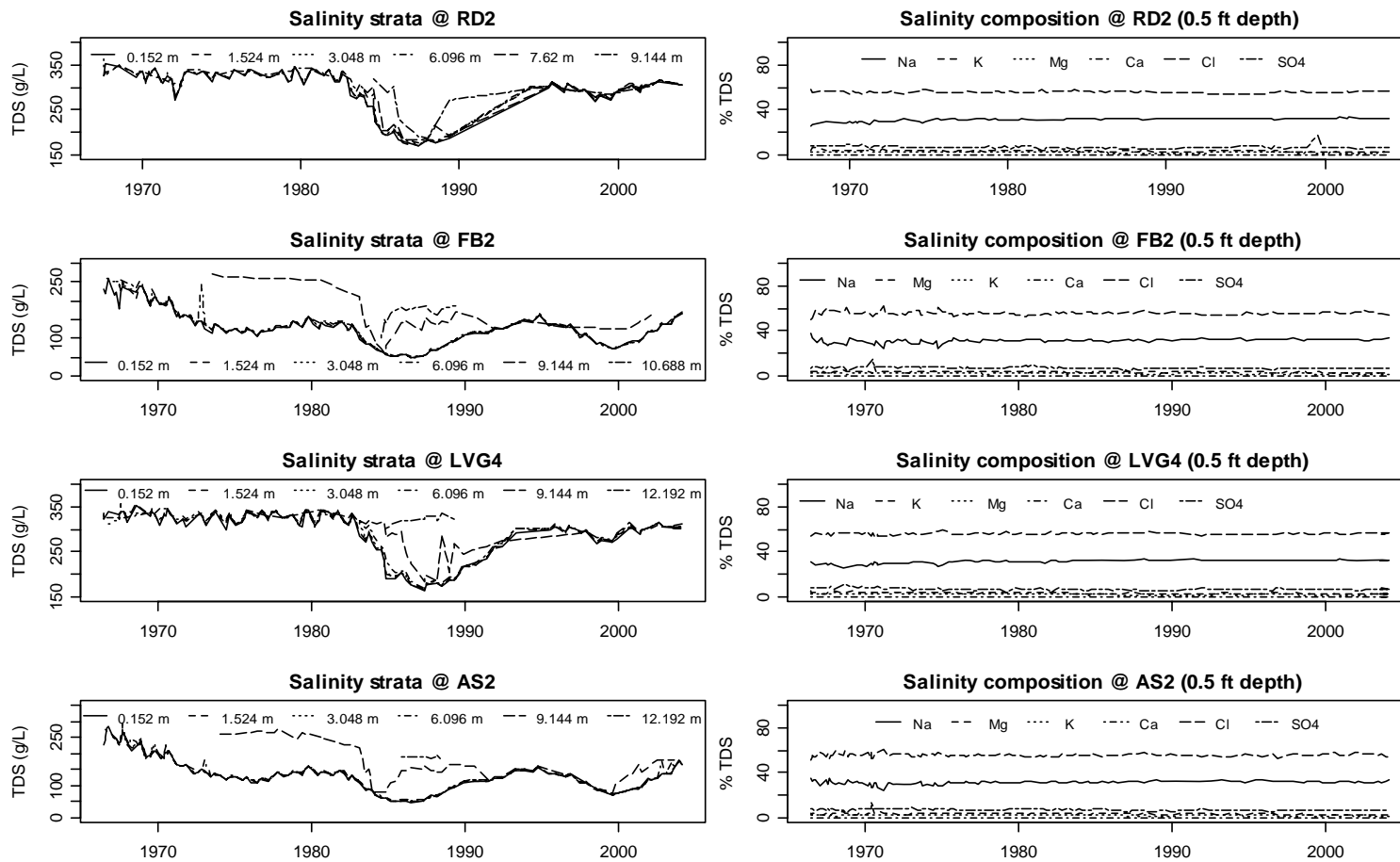
Figure 3-10. Time series of salinity and its chemical composition for the Great Salt Lake at Utah Geological Survey monitoring sites RD2 and LVG4 in the north arm and FB2 and AS2 in the south arm. Salinity was measured at various depths below the level of the lake surface. Ionic composition of the GSL brine is presented at 0.5 ft below the level of the lake surface.
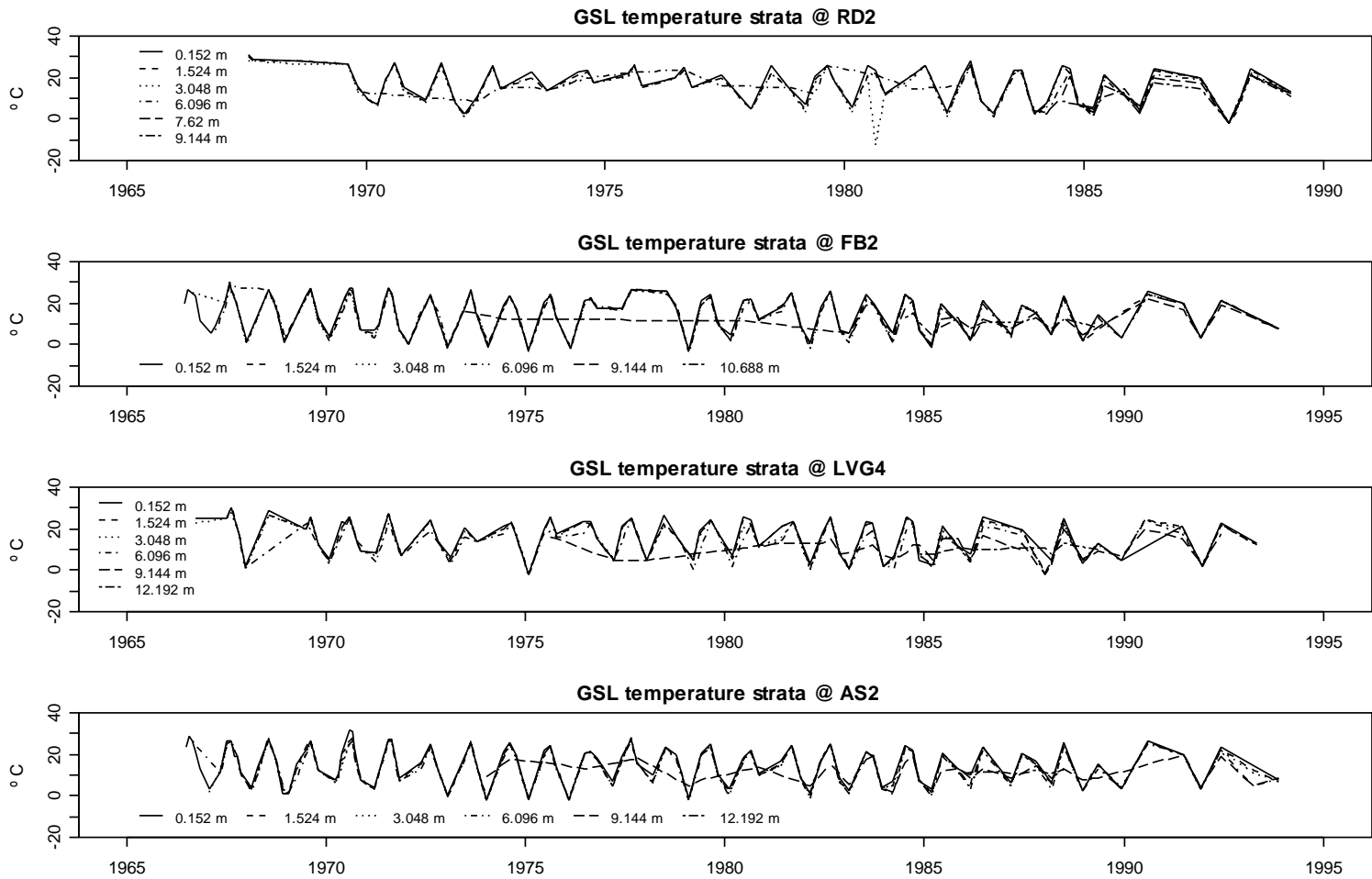
Figure 3-11. Time series of temperature strata for the Great Salt Lake. UGS four sites RD2 and LVG4 in the north arm and FB2 and AS2 in the south arm are used. Temperature is measured at various depths below the level of the lake surface as shown

CHAPTER 4

GREAT SALT LAKE VOLUME CHANGES

One goal of this study is to develop and improve the capability for modeling the changes in volume and fluctuations in level of the Great Salt Lake as they are related to topography and climate inputs. The task of modeling the changes of the GSL requires understanding the fluctuation of the GSL volume time series as well as the climate driving forces for the lake. The fluctuation in the GSL level is a response to various processes that interact together discussed and shown in Figure 1-1. In this chapter we approached the task of modeling the changes in the GSL volume by identifying the dates at which the GSL volume reaches its annual peak and annual minimum using frequency domain analysis. These dates (June 30th, and Nov. 1st) of peak and minimum of the GSL volume respectively were used to calculate the rise and fall time series of the GSL volume. The changes in volume during rise and fall periods were related to the climate and hydrological processes acting on the lake. Statistical models for the various processes acting on the GSL have been presented and discussed.

4.1. Fourier Analysis

Fourier or frequency analysis (originally developed by 18th century French mathematician, Jean Baptiste Joseph Fourier, 1768-1830) is based upon the fact that any periodic function can be represented as a sum of sine and cosine functions.

Frequency analysis represents a time series (GSL volume in this case) in terms of the amplitudes associated with oscillation wavelengths, rather than individual than individual data values. This way of representing time series has been widely used in many fields of data analysis. In this study, we concentrate on Fourier analysis of discrete and finite domain (periodic) functions. Let Z_t, $t = 1...n$, be a sequence of n numbers representing the GSL volume time series. These n values span period T with spacing Δt, such that $T = n\,\Delta t$. We can represent the sequence of n numbers, $[Z_t]$, as a linear combination of the orthogonal trigonometric functions (Wei, 1990):

$$Z_t = \sum_{k=0}^{[n/2]} [a_k \cos(2\pi kt/n) + b_k \sin(2\pi kt/n)], t=1, 2\ldots n \qquad (4.1)$$

where,

$$a_k = \begin{cases} \dfrac{1}{n}\sum_{t=1}^{n} Z_t \cos w_k t & k = 0, n/2 \text{ if n even} \\[2ex] \dfrac{2}{n}\sum_{t=1}^{n} Z_t \cos w_k t & k = 1\ldots\dfrac{n-1}{2} \end{cases}$$

$$b_k = \dfrac{2}{n}\sum_{t=1}^{n} Z_t \sin w_k t \qquad k = 1, 2, \ldots, \dfrac{n-1}{2} \qquad (4.2)$$

and:

$$w_k = 2\pi k/n\Delta t = 2\pi k/T \qquad \text{for k in the range 1 to n/2.}$$

Here the original time series of n Z_t values has been represented instead by n/2, a_k, and b_k Fourier coefficients giving the phase and amplitude associated with wavelengths w_k that make up the time series. The subscript k defines a wave number used to identify each wavelength.

The equivalent and notationally more compact complex number Fourier representation is:

$$Z_t = \sum_{k=-\text{trunc}\left(\frac{n-1}{2}\right)}^{\text{trunc}\left(n/2\right)} c_k e^{iw_k t} \text{ , where; } c_k = \frac{1}{n}\sum_{t=1}^{n} Z_t e^{-iw_k t}. \tag{4.3}$$

Here trunc denotes truncation to the integer below. Using the complex form, the original time series is represented by complex Fourier coefficients c_k, the magnitude and direction of which in the complex plane represent the amplitude and phase associated with each wavelength w_k.

In order to model the changes of the GSL volume we have chosen a consistent time period for all processes under study (temperature, streamflow, precipitation…). This time period was based upon examination of data availability. The best time period that captures all these processes was 1950-2000. Figure 4-1 shows the GSL volume time series with its Fourier transformation for this 1950-2000 time period calculated from equation (4.3). The filled dots show the Fourier coefficients associated with the annual cycle and its harmonics, i.e. wavelengths that

divide evenly into a year, or frequencies that are multiples of the annual cycle. When taken together these coefficients represent the annual seasonal cycle present in the lake time series. Other coefficients represent non seasonal effects, such as longer term cycles or trends.

Spectral analysis was used to identify time periods where on average the lake is rising or falling. Figure 4-2 depicts the annual cycle reconstructed using the Fourier coefficients that represent the annual seasonal cycle and its harmonics, i.e. those coefficients corresponding to frequencies of 1, 2, 3 ... 12 cycles per year. On this Figure we identified the date of which the annual cycle peaks as June 15th and the date at which the annual cycle troughs (reaches a minimum) as November 1st. We also performed this frequency domain analysis for the GSL total volume for the whole time span available 1847-2004. We found the same peak and trough dates (i.e., June 15th and November 1st) indicating that solution for the peak and fall periods is consistent with the longer record. From the spectral analysis we have concluded that the GSL volume goes through an annual cycle where on average the lake is rising between November 1st and June 15th, then falling from June 15th to November 1st. For the analysis in this thesis we used the annual peak date as June 30th instead of June 15th because the dataset of other variables is monthly. The periods November 1st - June 30th, and June 30th – November 1st have consequently been used to identify separate volume increase and volume decrease time series.
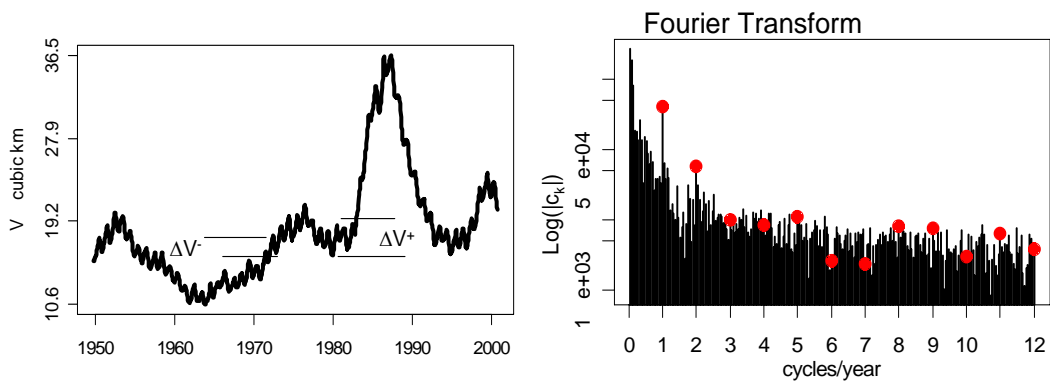
Figure 4-1.   The Great Salt Lake biweekly volume time series (1950-2000) with its Fourier transformation.
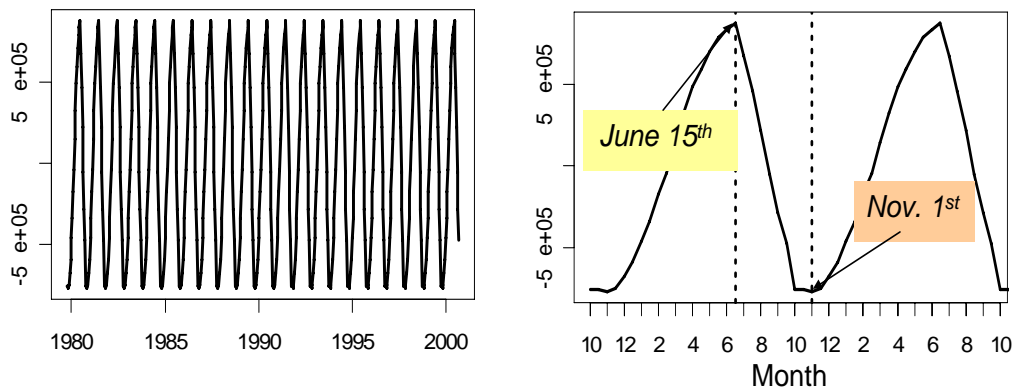
Figure 4-2.   Reconstructed GSL annual volume cycle.

Figure 4-3 depicts the time series of the GSL rise and fall period volume changes based on the November 1st - June 30th rise and June 30th – November 1st fall periods identified using spectral analysis. In Figure 4-3 spring volume increases were calculated as: GSL total volume on June 30th at year$_{i+1}$- GSL total volume on November 1st at year$_i$ (i refers to the year of the beginning period). Fall volume decreases were calculated as: GSL total volume on November 1st at year$_i$- GSL total volume on June 30th at year$_i$. Note that the deviations (rise and fall) during 1983-1986 depict the major flood during that time.
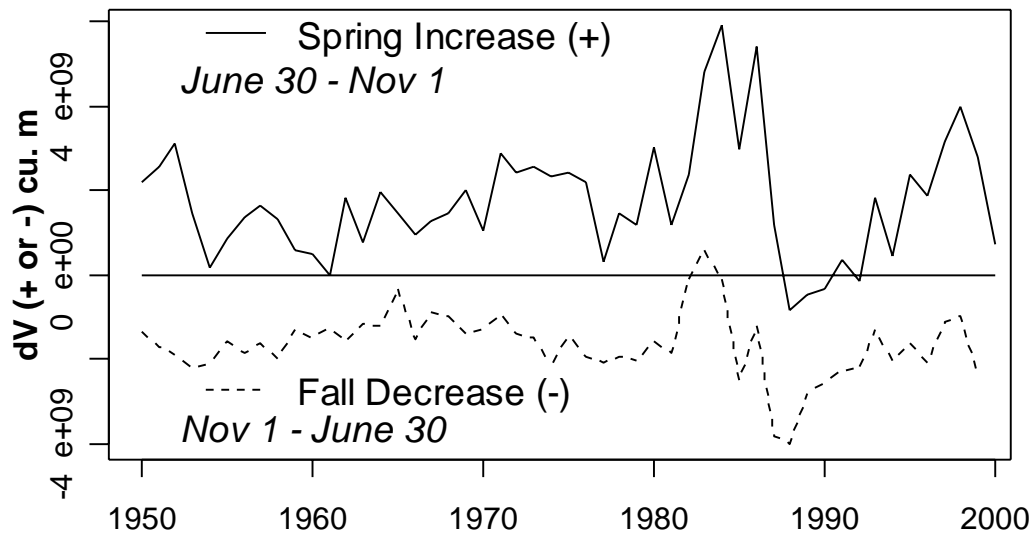
Figure 4-3. Time series of the annual rise and fall changes of the GSL's total volume.

4.2. GSL Volume Changes

One of the main drivers of changes in the GSL volume is the streamflow input to the lake. The annual average streamflow input to the GSL from stations nearer to the GSL representing the various watersheds draining to the GSL is shown in Table 4-1. These stations were used to calculate the total streamflow input to the GSL for the analysis of the GSL volume change. Other main drivers of changes in the GSL volume are precipitation on the lake and evaporation from the lake. The fluctuation in the GSL volume changes is described by the mass balance equation. Specifically, mass balance equation of the GSL suggests;

$$\Delta V = Q + AP - AE \qquad\qquad\qquad (4.4)$$

where ΔV is the change in volume, Q is the total streamflow input to the GSL, A is the total GSL area, P is the precipitation on the lake, and E is evaporation from the lake. There are observations of Q, P, and lake level that give us A and ΔV. Therefore using equation (4.4) we estimated evaporation from the GSL during rise and fall periods. The results of the mass balance analysis are summarized in Table 4-2 together with associated variables. The annual average air temperature was measured at 2 m above the lake surface, the annual average lake area and volume changes were calculated from level - area - volume relations, and the annual average evaporation from the lake was calculated from mass balance. Figure 4-4 gives a plot of evaporation depth estimated from equation (4.4) and area during the fall period.

The area in Figure 4-4 was calculated as the average for each specific fall period (June 30th –Nov 1st). The Y axis gives the evaporation depth calculated as evaporation volume divided by area. The lines on this figure are LOWESS fits from R using default parameters (http://www.r-project.org/). We had hoped in this figure to detect the effect of salinity on evaporation depth, with higher evaporation depth being anticipated for larger lake area due to the reduction in salinity with increases in lake volume. This is not observed in Figure 4-4 when all the data is considered, perhaps due to the several uncertainties in this data. However, there is a suggestion of this relationship if we fit a LOWESS line omitting the years 1983, 1984, and 1986 from the LOWESS fit. There may be some justification for this, because these are the wettest years on record with the highest total runoff into the lake. Anecdotally Lall, Sangoyomi, and Abarbanel (1996) indicated that there were reports of springs flowing into the lake from the West Desert. These inflows have not been captured in the observed Q used in equation (4.4) and this omission would bias the calculation of evaporation depth downwards.

We used scatterplots to explore possible relationships between the GSL volume changes and climate variables. To account for seasonal effects the variables plotted were standardized using the monthly mean and standard deviation. Specifically:

$$x'_{i,j} = \frac{x_{i,j} - \mu_j}{\sigma_j} \qquad (4.5)$$

where $x'_{i,j}$ is the standardized value for year i and month j, $x_{i,j}$ is the observed value for year i and month j, μ_j is the mean of $x_{i,j}$ for month j over all the years i, and σ_j is the standard deviation of $x_{i,j}$ for month j over all the years i. These scatterplots, shown in Figure 4-5 include both fall (Jul-Oct) and rise (Nov-June) records as indicated by the two symbols o "fall", Δ "rise". The strongest relationships apparent in Figure 4-5 are volume change versus streamflow and volume change versus precipitation indicating that the main drivers for the GSL volume changes are streamflow and precipitation.

Table 4-1.   Streamflow input to the GSL

Watershed	Area (km^2)	Station	Average Annual flow (M m^3/year)	Percentage of Total Annual Average Flow
Bear	19,262	USGS # 10126000, Bear River Near Corinne[a]	1600	71.2%
Weber	6,413	USGS # 10141000, Weber River near Plain City USGS	520	23.2%
Jordan / Provo	9,963	USGS # 10171000, Jordan River at 1700 South at SLC	126	05.6%

[a] The missing data (1957-1963) has been filled from the nearby station (USGS # 10118000, Collinston, UT)

Table 4-2. Average GSL volume changes, total streamflow input, total area, total precipitation, air temperature, and estimated evaporation using mass balance equation (4.4) for rise and fall periods

Variable		Average
GSL Volume Changes	Rise	1552 (M m^3)
	Fall	–1449^a (M m^3)
Total Streamflow	Rise	1748 (M m^3)
	Fall	361.1 (M m^3/yea)
GSL Area	Rise	3874 (M m^2)
	Fall	3810 (M m^2)
GSL Precipitation	Rise	0.241 (m)
	Fall	0.073 (m)
GSL Air Temperature	Rise	6.393 (°C)
	Fall	19.37 (°C)
Evaporation	Rise	1096 (M m^3)
	Fall	2094 (M m^3)

---

^{a} (-) indicates fall volume decreases from November 1st -June 30th.
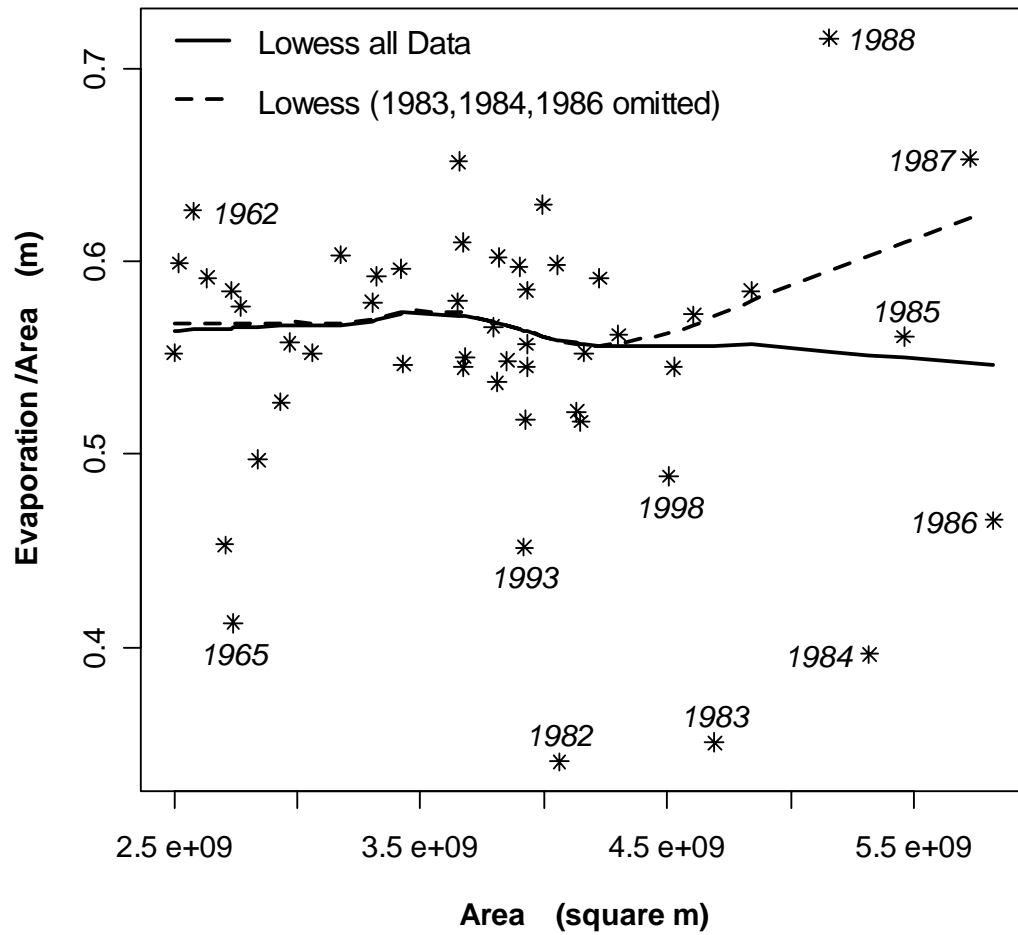
Figure 4-4. The GSL mass balance evaporation during fall period (June 30th –Nov 1st) versus lake area averaged over each specific fall period.
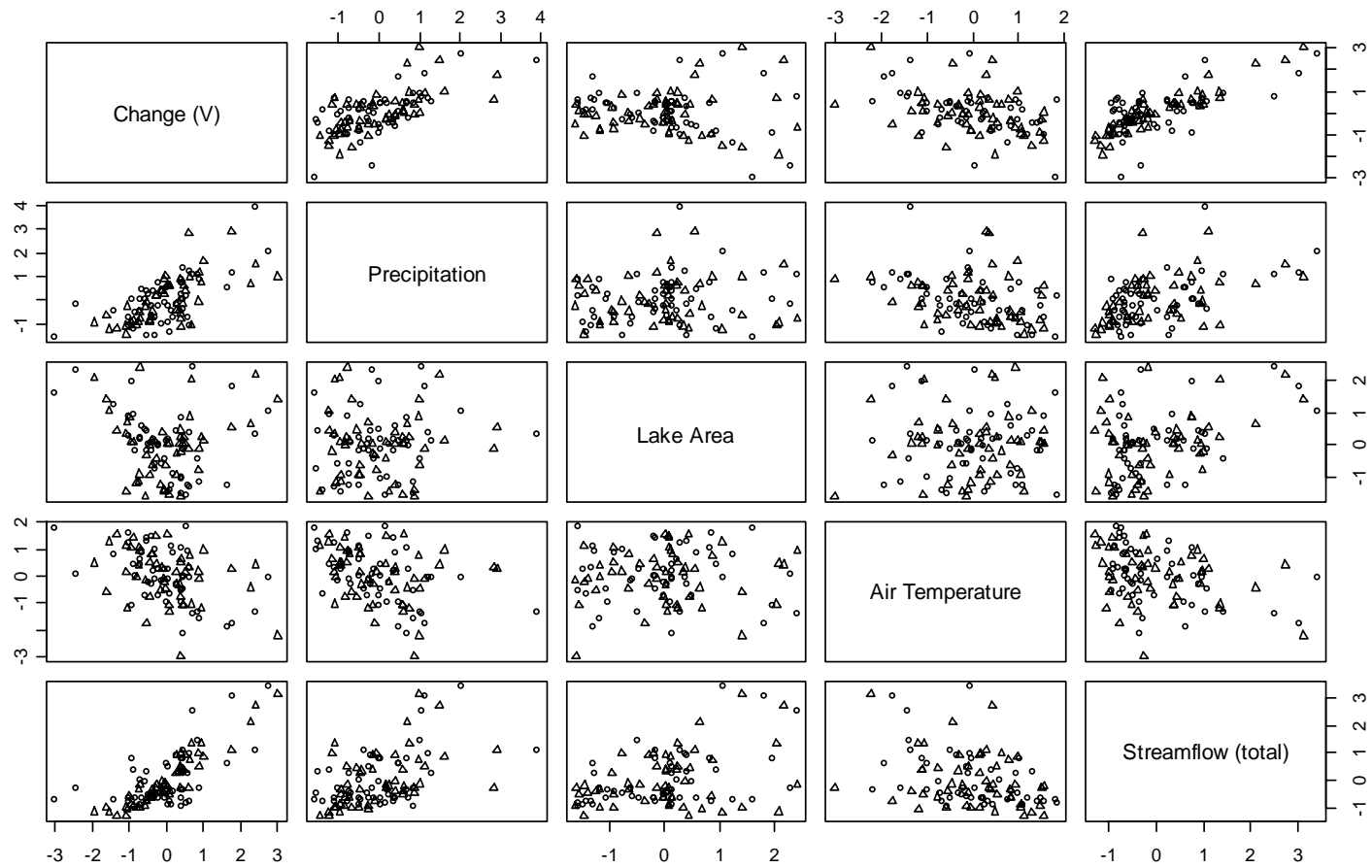
Figure 4-5.   Scatter plots of GSL volume changes with other processes (standardized). (Δ) represents rise time series (Nov-Jun) while (o) represents fall time series (Jul-Oct) for the chosen time span (1950-2000).

The changes of the GSL volume are directly connected to the climate driving forces acting on the lake. We modeled these changes of the GSL volume using regression models. Our intent was to quantify these changes with respect to the various hydrological processes acting on the lake. We used the dates (June 30th and Nov. 1st) presented earlier in Figure 4-3 to get rise and fall time series for climate processes. As stated earlier the time period for doing this analysis was based upon examination of data availability (1950-2000). We used an automated backward multivariable stepwise regression analysis to examine which variables were significant in describing the dependence of the GSL volume changes. We firstly tested the rise change of the GSL volume with the total rise streamflow draining to the lake, the rise streamflow of the Bear watershed, the rise precipitation on the lake, the rise air temperature over the lake, the rise lake area, the rise volume of the lake, and the inverse of the rise volume of the lake using the automated stepwise regression. This model is written as:

$$\Delta V_{lake}^{+} = f\left(Q_{total}^{+}, Q_{Bear}^{+}, P_{lake}^{+}, T_{lake}^{+}, A_{lake}^{+}, V_{lake}^{+}, \frac{1}{V_{lake}^{+}}\right) \qquad (4.6)$$

where (+ in the superscript denotes a quantity during the rise period);

$Q_{total}^{+} \equiv$ total streamflow during the spring increase months (i.e., Nov, Dec…June) from the Bear, Weber, and Jordan/Provo watersheds as explained from Table 4-1;

$Q_{Bear}^{+} \equiv$ streamflow during the spring increase months for the Bear watershed;

$P^+_{Lake} \equiv$ precipitation on the lake during the spring months;

$T^+_{Lake} \equiv$ temperature on the lake during the spring months;

$A^+_{Lake} \equiv$ total area of the lake during the spring months;

$V^+_{Lake} \equiv$ total volume of the lake during the spring months.

Similarly, the fall change in volume is tested with the total fall streamflow draining to the lake, the fall precipitation on the lake, the fall air temperature over the lake, the fall lake area, and the inverse of the fall volume of the lake. This model is written as:

$$\Delta V^-_{lake} = f\left(A^-_{lake}, T^-_{lake}, \frac{1}{V^-_{lake}}, Q^-_{total}, P^-_{lake} \right) \tag{4.7}$$

where (-) in superscript denotes fall decrease months (i.e., Jul, Aug…Oct) and the variables are the same as used in the rise change of volume model in equation (4.6).

The automated stepwise results of models (4.6 and 4.7) are summarized in Table 4-3. The results in Table 4-3 show that the stepwise regression selected streamflow, precipitation and lake area as explanatory variables for both periods. The regression relationships fitted are:

$$\Delta V^+_{lake} = 1.388\, Q^+_{total} + 5.656 \times 10^9\, P^+_{lake} - 0.277\, A^+_{lake} - 1.137 \times 10^9\, m^3$$
$$\Delta V^-_{lake} = 1.673\, Q^-_{total} + 7.108 \times 10^9\, P^-_{lake} - 0.588\, A^-_{lake} - 3.337 \times 10^8\, m^3 \tag{4.8}$$

The coefficient of determination, R^2, in both the rise and fall models was above 0.9 which indicates both the models did well in explaining the variance (or reduced uncertainty). Other statistics given in Table 4-3 indicate that these are good, statistically significant regressions. Figure 4-6 gives predicted versus observed plots for these regressions (equation 4.8).

Table 4-3. The GSL volume changes and climate indices stepwise regression analysis results

	Variable	Coefficient	t-stat	p-val
ΔV^+	Q^+_{total}	1.38762	22.0536	0.0000
	P^+_{lake}	5.65623e+9	06.8941	0.0000
	A^+_{lake}	-0.277014	-4.4243	0.0001
Intercept	-1.137e+009			
R-square	0.954076			
F	318.549			
RMSE	3.32367e+008			
Adj. R	0.950082			
P	0			
	Variable	Coefficient	t-stat	p-val
ΔV^-	A^-_{lake}	-0.58789	-14.349	0.0000
	Q^-_{total}	1.67361	12.5654	0.0000
	P^-_{lake}	7.10826e+9	7.4747	0.0000
Intercept	-3.3369e+008			
R-square	0.900427			
F	153.96			
RMSE	2.09583e+008			
Adj. R	0.901552			
P	0			
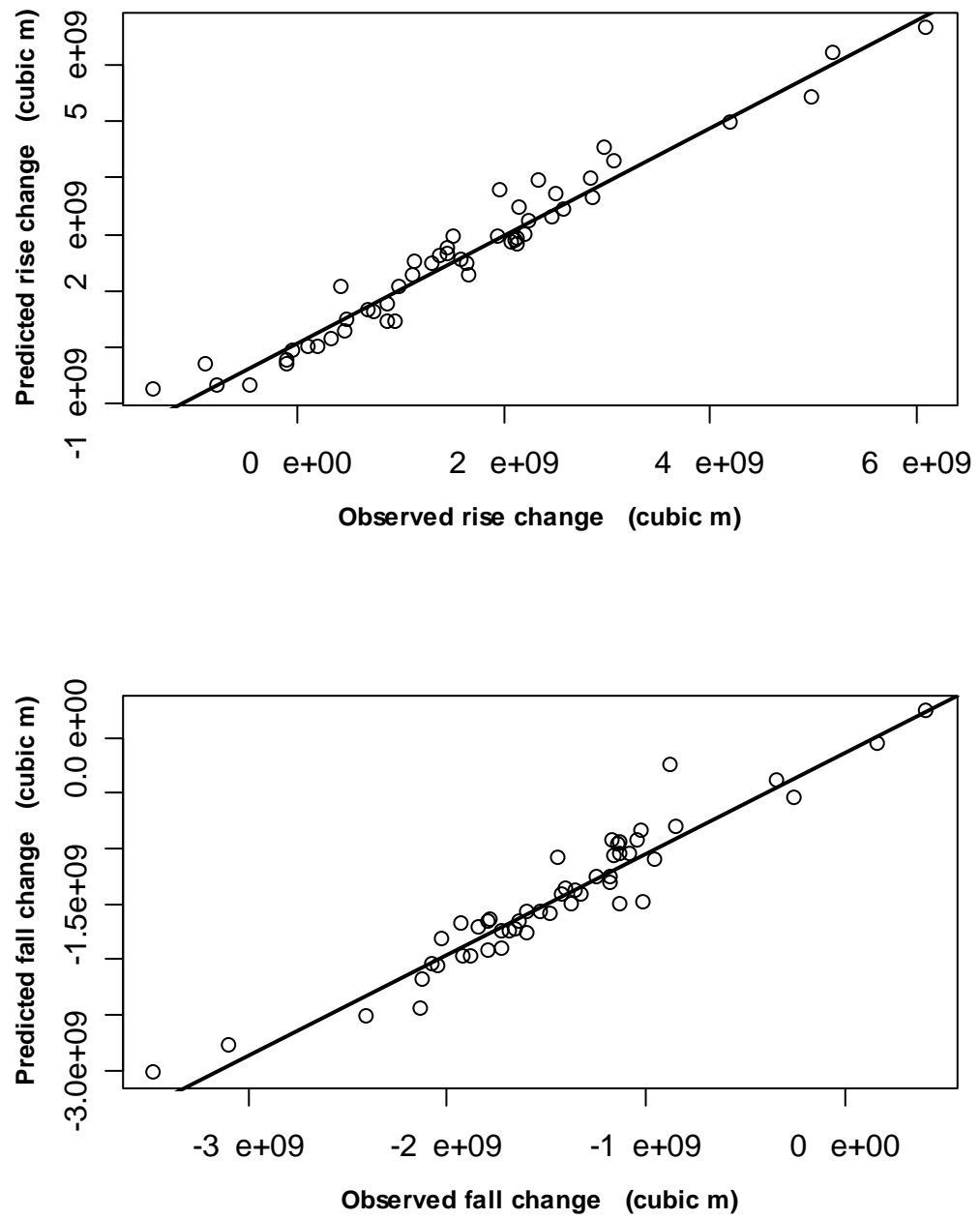
Figure 4-6.   GSL rise and fall prediction models from equation (4.8).

We infer from the regression that the GSL volume changes are highly correlated with and driven by streamflow, precipitation and lake area. The relationship between the lake volume changes and lake area represents the effect of evaporation the only outflow of the lake. It is instructive to compare these regression relationships to what we might deduce from mass balance equation (4.4). The average area of the GSL during rise and fall periods is 3.9×10^9, 3.8×10^9 m^2 respectively (Table 4-2). This is less than, but the same order of magnitude as the coefficients on P_{lake} in equation (4.8). Average annual lake evaporation during rise period is around 0.283 m, while during the fall period it is around 0.55 m. This is very comparable to the 0.277 and 0.588, the coefficients of A_{lake} during the rise and fall periods. The fact that the coefficient on A_{lake} for fall volume change is larger reflects greater evaporation when the lake is falling, even through this period is shorter. The regression coefficients on Q are larger than 1, indicating that Q is taking on a greater explanatory role than would be suggested by mass balance alone.

Figure 4-7 shows how the change in the GSL volume is strongly connected to the total streamflow to the lake during rise months (Nov - June) as well as precipitation on the lake. This relation between rise streamflow input and changes in volume is close to a 1:1 relation. The mass balance equation (4.4) could be used directly to infer the coefficients in equations similar to the regression equations (4.8). This would suggest:

$$\Delta V^+_{\text{lake}} = Q^+_{\text{total}} + 3.87 \times 10^9 \, P^+_{\text{lake}} - 0.283 \, A^+_{\text{lake}} \quad m^3$$
$$\Delta V^-_{\text{lake}} = Q^-_{\text{total}} + 3.81 \times 10^9 \, P^-_{\text{lake}} - 0.550 \, A^-_{\text{lake}} \quad m^3$$

(4.9)

Here coefficients on P, 3.87×10^9 and 3.81×10^9 are the average lake area during the rise and fall periods (Table 4-2). The coefficients on A, -0.283 and -0.55 are the average lake evaporation depth during rise and fall periods.
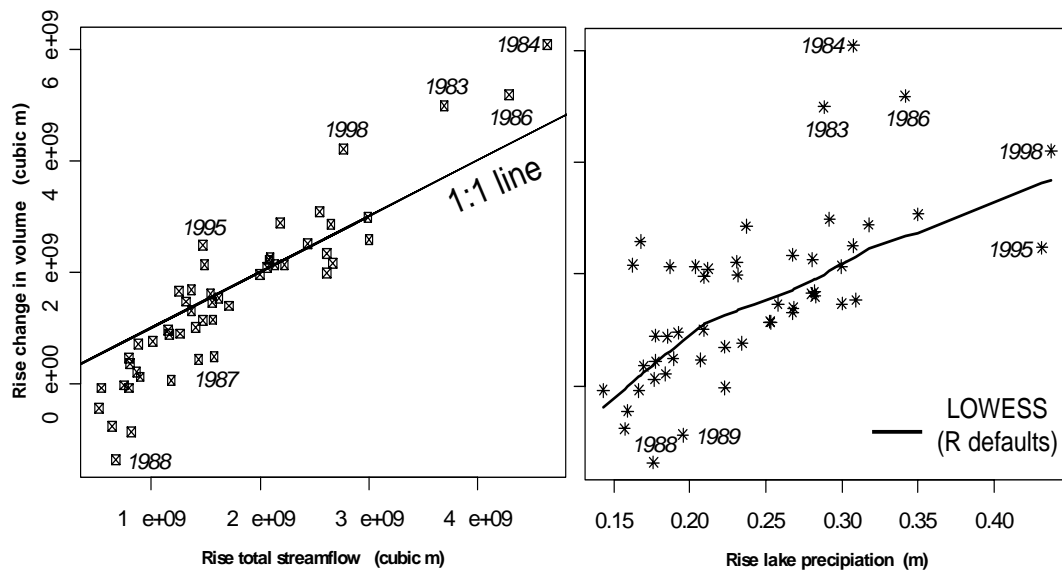
Figure 4-7. The GSL rise volume change response to the total streamflow to the lake and annual rise months precipitation on the lake.

Figure 4-8 shows the observed versus predicted plot using these equations (4.9) inferred from mass balance equation (4.4). The fraction of variance explained by this relationships (Figure 4-8) calculated from the mean square error as $1\text{-}MSE/\sigma^2$, equivalent to R^2, is 0.9499 and 0.7933 for the rise and fall models respectively. For the rise period this is only very slightly less than from regression indicating that during the rise period lake volume increases are well predicted by mass balance and the inputs P and Q. For the fall period this model has less explanatory power than the regression model, though it is still relatively good, indicating that during the fall period there is more uncertainty on lake level change perhaps due to the greater role played by evaporation that is not a direct input to the equations. This difference suggests that there may be some benefit in quantifying ΔV^- from better quantifying E.

4.3. Bear River Macro Hydrology

In Table 4-1 we mentioned that the ratio of the average annual inflow from the Bear watershed to the GSL is 71.2%. Since, the Bear watershed is the main contributor of the GSL streamflow input an analysis of the hydrology the Bear watershed has been performed to examine what drives the Bear River streamflow. Figure 4-9 shows statistical relations between the rise streamflow per unit area with rise precipitation and rise air temperature for the Bear watershed. The lines on this figure are LOWESS fits from R using default parameters. We see that the runoff ratio of the Bear River during the rise months varies between 0.13 and 0.167. Also,

the trend seen in streamflow versus precipitation is positive, while the trend in streamflow versus temperature is slightly negative.

The Bear River basin is a snowmelt dominated watershed. We examined the relationship between annual streamflow and maximum snow water equivalent (max SWE) shown in Figure 4-10. We used the method described in Figure 3-2 to get the maximum snow water equivalent (max SWE) by averaging and adjusting point SNOTEL measurements. The stations used for the averaging in the Bear watershed are listed in Table 3-1. We see that the annual streamflow is correlated with the maximum SWE as well as air temperature. The correlation between max SWE and air temperature is negative because higher temperatures reduces snow water equivalent. The average adjusted annual maximum snow water equivalent observed in the Bear watershed is 522 mm.

4.4. Conclusion

This chapter identified the periods when the GSL is rising and falling from spectral analysis as November 1 to June 15 and June 15 to November 1 respectively. The dominant drivers affecting the GSL volume are streamflow, precipitation, and lake area that controls evaporation. From the data available we developed a regression model for the GSL volume changes. Explanatory variables were streamflow, precipitation and lake area. The regression models for the rise and fall periods presented were good regressions with coefficient of determination, R^2, above 0.9. Most of the inflow to the GSL comes from the Bear watershed (71.2% on

average). The runoff ratio of the Bear River during the rise months varies between

0.13 and 0.167. The statistical relationships presented provide a broad quantitative

understanding of the GSL basin hydrology and the GSL volume changes driven by

this hydrology.
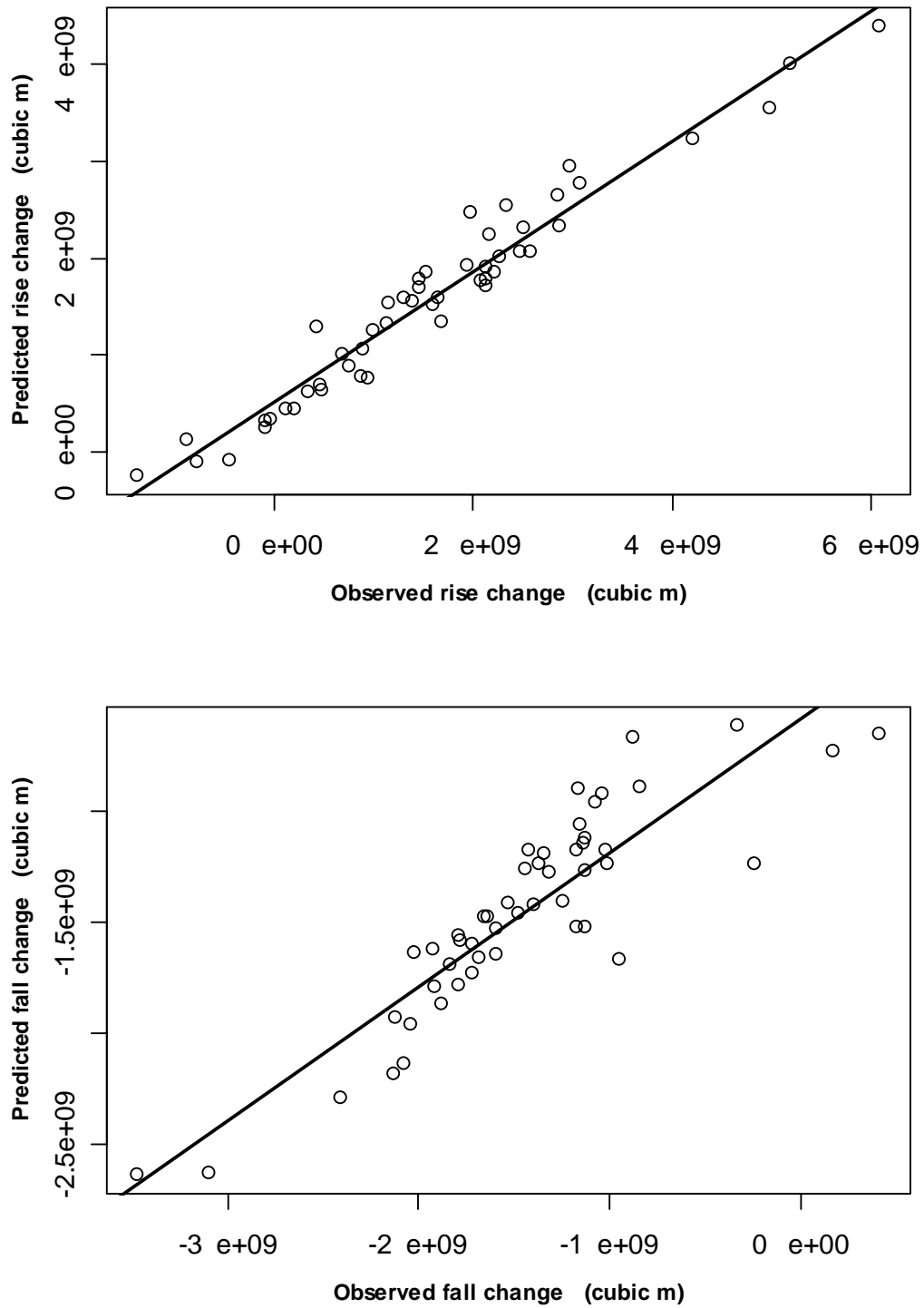
Figure 4-8. GSL rise and fall prediction models from equation (4.4) with average area and evaporation estimated to rise and fall periods.
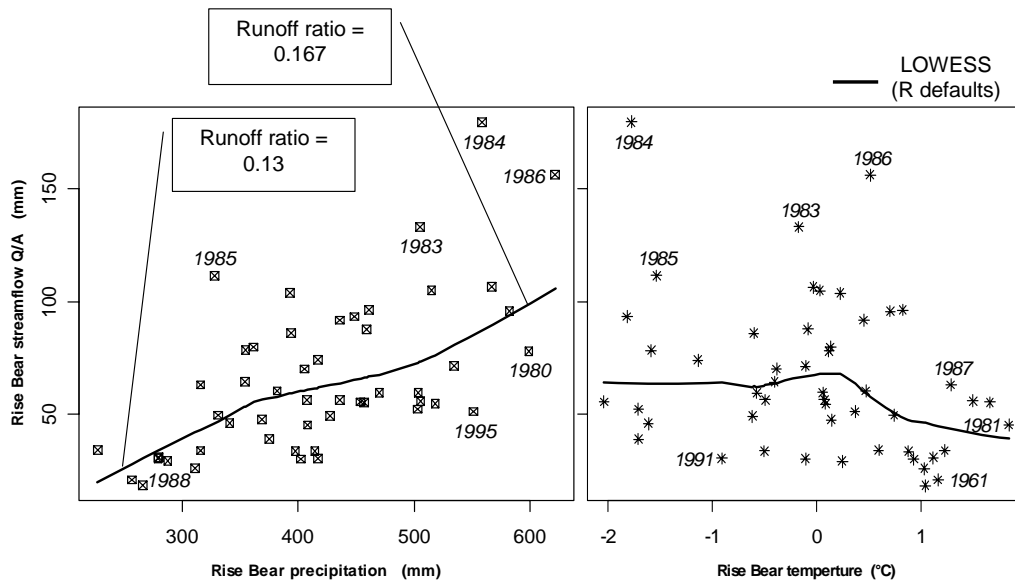
Figure 4-9.   The Bear River basin macro-hydrology. Streamflow responses to precipitation and temperature.
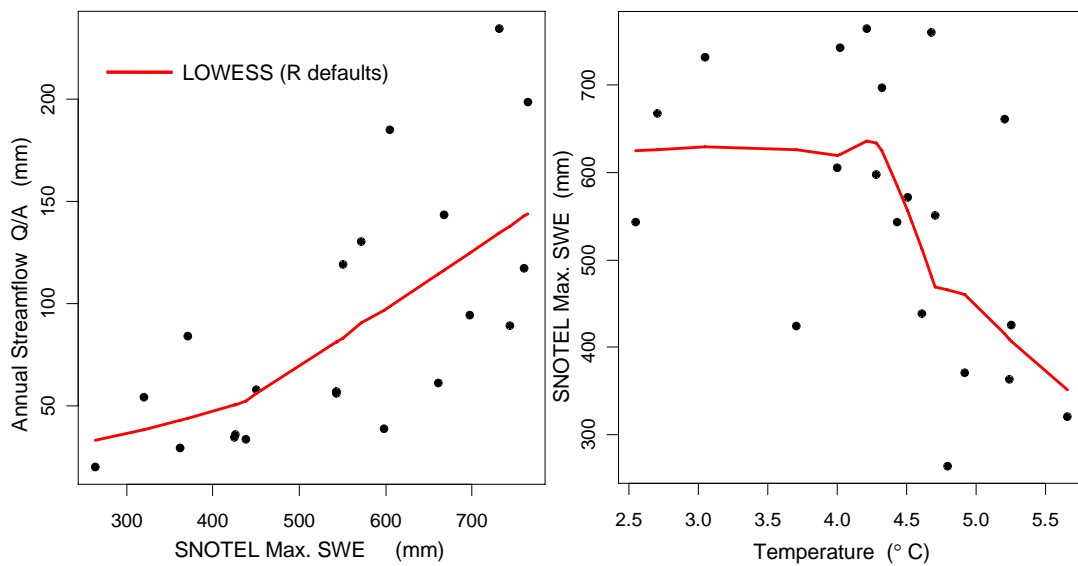
Figure 4-10. The Bear River basin macro-hydrology. Streamflow responses to snow water equivalent (SWE) and annual forcing.

CHAPTER 5

GREAT SALT LAKE MODES

The Great Salt Lake (GSL) level fluctuates due to the balance between inflows and outflows. These fluctuations are of interest whether they are high (flooding hazards) or low (economic impacts). Previous work (Lall, Sangoyomi, and Abarbanel, 1996) examined the probability distribution of historic bi-weekly lake volumes (1847-1992) and found multiple modes. These have been interpreted as potentially due to separate attractors in the nonlinear dynamics of the system. The topographic area-volume relationship in the GSL plays a role in the system dynamics because area is a control on the evaporation outflux, the only outflow from the system. The increase in lake area with increasing lake volume increases evaporation and has a stabilizing effect on the volume and level of the GSL. Where, for a given change in volume, the lake area goes through a large change, the outflux evaporation will go through a correspondingly large change, tending to stabilize the volume at that point. On the other hand, if for a given change in volume, the lake area only changes by a small amount the outflux evaporation will only change by a small amount resulting in a small stabilizing effect. These considerations suggest that modes of the lake volume distribution should coincide with peaks in the area - volume derivative. In this chapter we compared peaks in the area - volume derivative with modes in the lake volume distribution to examine which modes may be attributable to this effect.

Figure 5-1 shows the time series of biweekly GSL volumes and the representation of the frequency distribution of GSL volumes using a histogram of the GSL biweekly volumes from 1847-1992. This data was studied by Lall, Sangoyomi and Abarbanel (1996) who first noted the presence of multiple modes suggestive of preferred states in the lake dynamics. In Figure 5-1 there are three modes centered at volumes of 34.2 km^3, 21.4 km^3, and 14.8 km^3. These represent volumes at which clusters occur in the lake volume time series and the question is why do these clusters or preferred states occur.
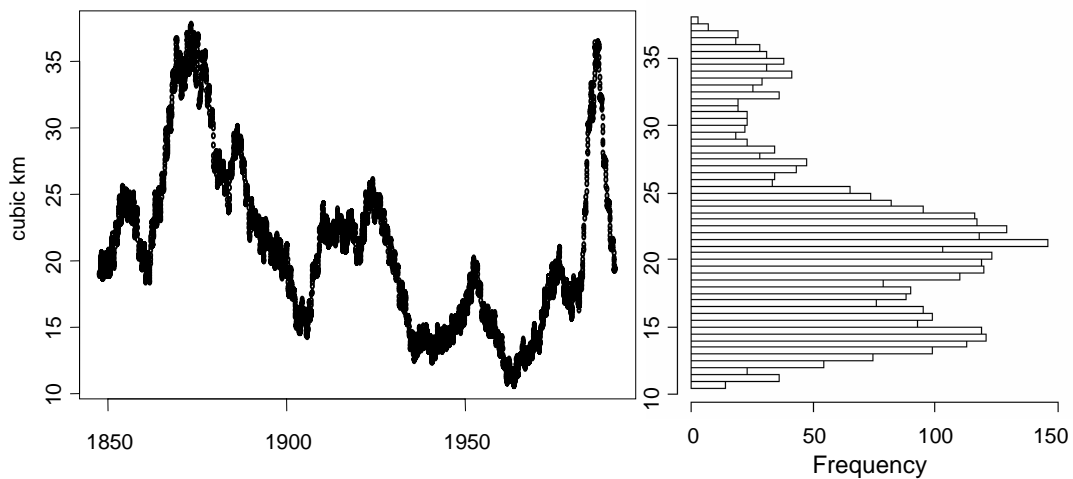
Figure 5-1. Great Salt Lake total biweekly volume and histogram (1847-1992) as studied by Lall, Sangoyomi, and Abarbanel (1996). The frequency histogram counts the number of times volume is within the volume range associated with each bin.

The distribution in Figure 5-1 is depicted using a histogram which counts the number of occurrences within predefined bins. This is the simplest way of depicting a distribution, but requires interpretation by the eye to "smooth" over the fine variability. It is therefore not very suitable for comparison of different distributions in the same graph. In recent years nonparametric density estimation methods have emerged to depict the distribution of data more generally (Silverman, 1986). Kernel methods are a popular nonparametric approach that we have used here. Kernel methods offer the advantages of being based on local neighborhoods, data driven and adaptive, requiring weak or limited assumptions about the underlying distribution. The kernel density estimate is defined as:

$$\widehat{f}(x) = \frac{1}{nh} \sum_{i=1}^{n} k\left(\frac{x - X_i}{h} \right) \qquad (5.1)$$

where X_i, i=1, 2… n represent n samples presumed to be from a probability distribution, h is the window or band width smoothing parameter, and k is the kernel function, that satisfies the conditions:

k(t)>0

and

$$\int_{-\infty}^{\infty} k(t)dt = 1. \tag{5.2}$$

Kernel based nonparametric density estimation requires selection of the kernel function k(.) and smoothing parameter h. The method is most sensitive to selection of h. Sheather and Jones (1991) presented a method for selecting the bandwidth smoothing parameter h of a Gaussian kernel density estimator that has been reported to give good results for a wide range of inputs. Here we used the default method implemented by the R density package (http://www.r-project.org/) to select bandwidth h. This estimates bandwidth following suggestions of Silverman (1986) as:

$$h = 0.9n^{-0.2}\min[\text{standard deviation}, (\text{interquartile range})/1.34] \tag{5.3}$$

where, h is the bandwidth parameter and n is sample size. Gaussian kernel functions were used.

Figure 5-2 gives kernel density estimates of the GSL's volume for the period 1847-1992 and 1847-2004. The probability density functions estimated have modes at 14.8, 21.4 and 34.2 cubic km corresponding to the modes observed in the histogram, Figure 5-1. The bandwidth that the R package estimated for the 1847-1992 data using equation (5.3) was 1.052 cubic km. The R package estimated a bandwidth for the 1847-2004 data as 0.894 cubic km. These are very close, but for

consistency, so that differences are not due to bandwidth differences Figure 5-2 is plotted using the average bandwidth of 0.973 cubic km. To check sensitivity to bandwidth we also plotted density estimates like Figure 5-2 with bandwidth 1.052 cubic km and 0.894 cubic km and obtained figures (not shown) that were very similar to Figure 5-2 with modes at the same locations. We therefore concluded that interpretations were not sensitive to the selection of bandwidth in the range resulting from different data lengths.

Examining Figure 5-2 it is apparent that the years 1993-2004 have resulted in some filling in of the trough between the lowest two modes in the density estimate, making these modes less distinct.

5.1. Bathymetry and the Probability
    Distribution of Lake Volumes

Bathymetry defines the relationship between lake volume, area and level. A simplified mass balance of the lake suggests that the rate of change in volume can be expressed as:

$$\frac{dV}{dt} = P + Q - E_v = P + Q - EA \tag{5.4}$$

where, P = Precipitation directly on the lake, Q = Streamflow entering the lake, E_v= Volumetric Evaporation rate from the lake, A= lake Area, and E = per unit area

Evaporation rate from the lake. Combining inputs P and Q into I this equation (5.4) can be generalized to:

$$\frac{dV}{dt} = I - EA \ .$$ (5.5)

If one assumes as a first approximation that the lake is in steady state, equation (5.5) suggests that area will adjust to balance lake input and output. Specifically

$$A = I/E \ .$$ (5.6)

So, if for simplicity we think of the lake as being forced primarily by variability in I with E constant, and assume that I has probability density function (PDF), f(I), then the corresponding PDF of A can be calculated. The PDF of A therefore represents the variability in climate input here represented by I. Since A and V are related through the bathymetry the PDF of V can be calculated. Specifically:

$$f_V(v) = f_A(a) \times \frac{dA}{dV}$$ (5.7)

where

$f_V(v)$ is the volume probability density function, $f_A(a)$ is the area (climate input) probability density function. The PDF of V is related to the rate of change of A with V, (expressed as a derivative) and this analysis suggests that modes in the PDF of V should correspond to peaks in the derivative dA/dV.
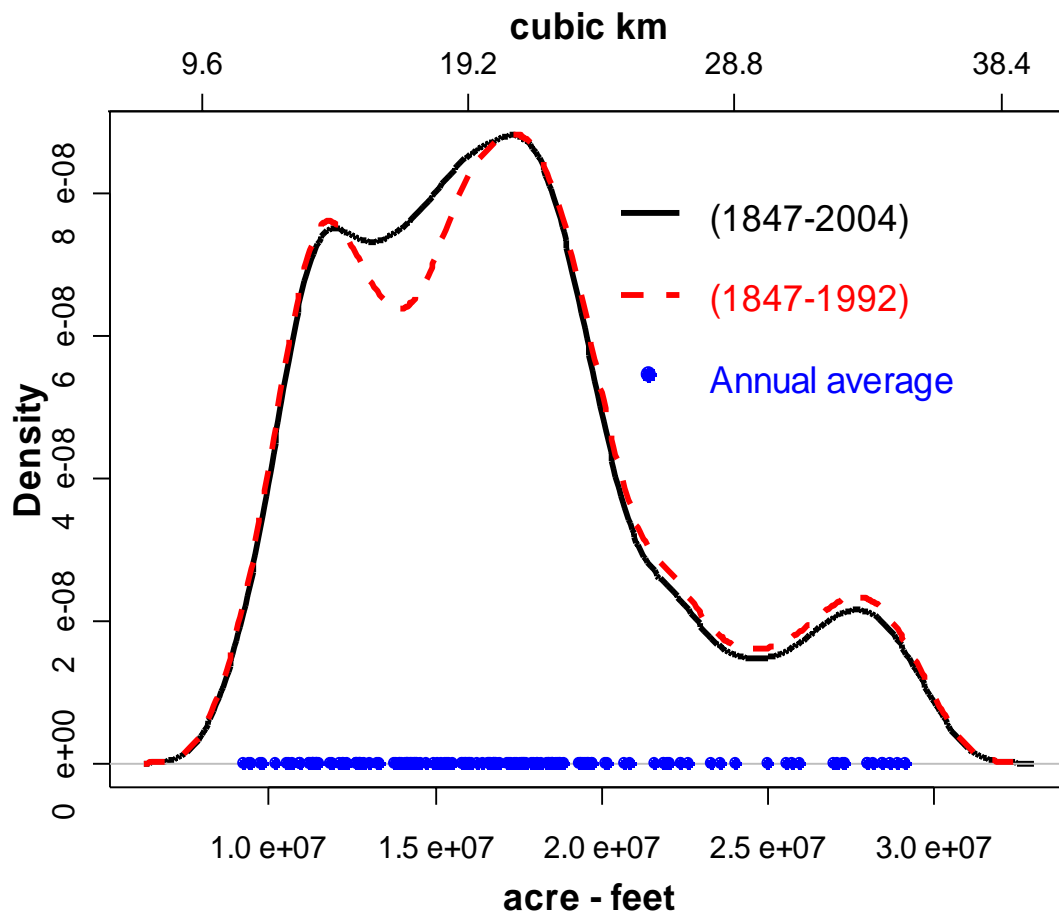
Figure 5-2. Kernel density estimate of the GSL's total biweekly volume distribution. The dots at the bottom represent the annual average total volume for the GSL. Bandwidth = 0.973 km^3.

Figure 5-3 gives kernel density estimates of the PDF of A for the periods 1847-1992 and 1847-2004. The bandwidth estimated using by R for 1847-1992 was 1.51×10^8 m^2 and for 1847-2004 was 1.445×10^8 m^2. Figure 5-3 is plotted using the average of these bandwidths, namely 1.478×10^8 m^2.
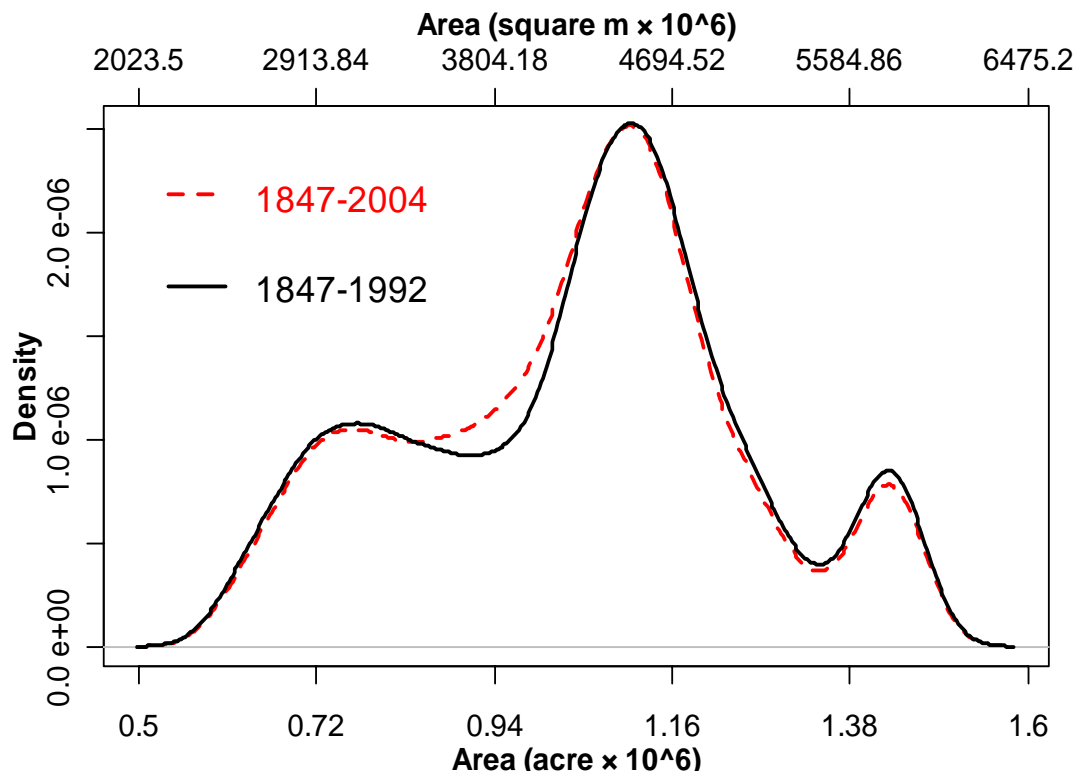
Figure 5-3.   Kernel density estimate of the GSL's total biweekly area (climate inputs) distribution. Bandwidth = 1.478×10^8 m^2.

Figure 5-4 gives the topographic derivative, $\frac{dA}{dV}$ of the Great Salt Lake

evaluated numerically from the data in Figure 3-8. In principle equation (5.7)

suggests that $f_V(v)$, Figure 5-2, should be obtained from the product of Figures 5-3

and 5-4. We performed a sequence of calculations to evaluate the applicability of

this. The results are given in Figure 5-5. The line labeled f1 is the volume density

estimate from the actual data, 1847-2004 repeated from Figure 5-2.

The first test was to evaluate the impact of the multimodality of the $f_A(a)$

distribution only. A constant $\frac{dA}{dV}$ was assumed in equation (5.7). This resulted in

line f2 that has shape very similar to Figure 5-3 but does not match f1. The density

function $f_A(a)$ is therefore alone not sufficient to produce multimodality in $f_V(v)$.

The second test was to evaluate the impact of $\frac{dA}{dV}$ only. A Gaussian

distribution was assumed for $f_A(a)$. This resulted in line f3. We see that

multimodality does emerge, so part of our hypothesis that bathymetry is responsible

for multimodality is true. However, comparing to f1 the modes are not in the correct

position and the main mode is not reproduced. Therefore, $\frac{dA}{dV}$ alone is not sufficient

to produce multimodality in $f_V(v)$.

The last test used the product of $f_A(a)$ from Figure 5-3 and $\frac{dA}{dV}$ from Figure

5-4. This resulted in line f4. We see that this line is generally close to f1. The

differences between f4 and f1 we believe are due to numerical differences between

kernel smoothing over area and over volume. The conclusion is that multimodality in the input and the bathymetry, manifested by $\dfrac{dA}{dV}$ are necessary to explain the multimodality and shape of $f_V(v)$.
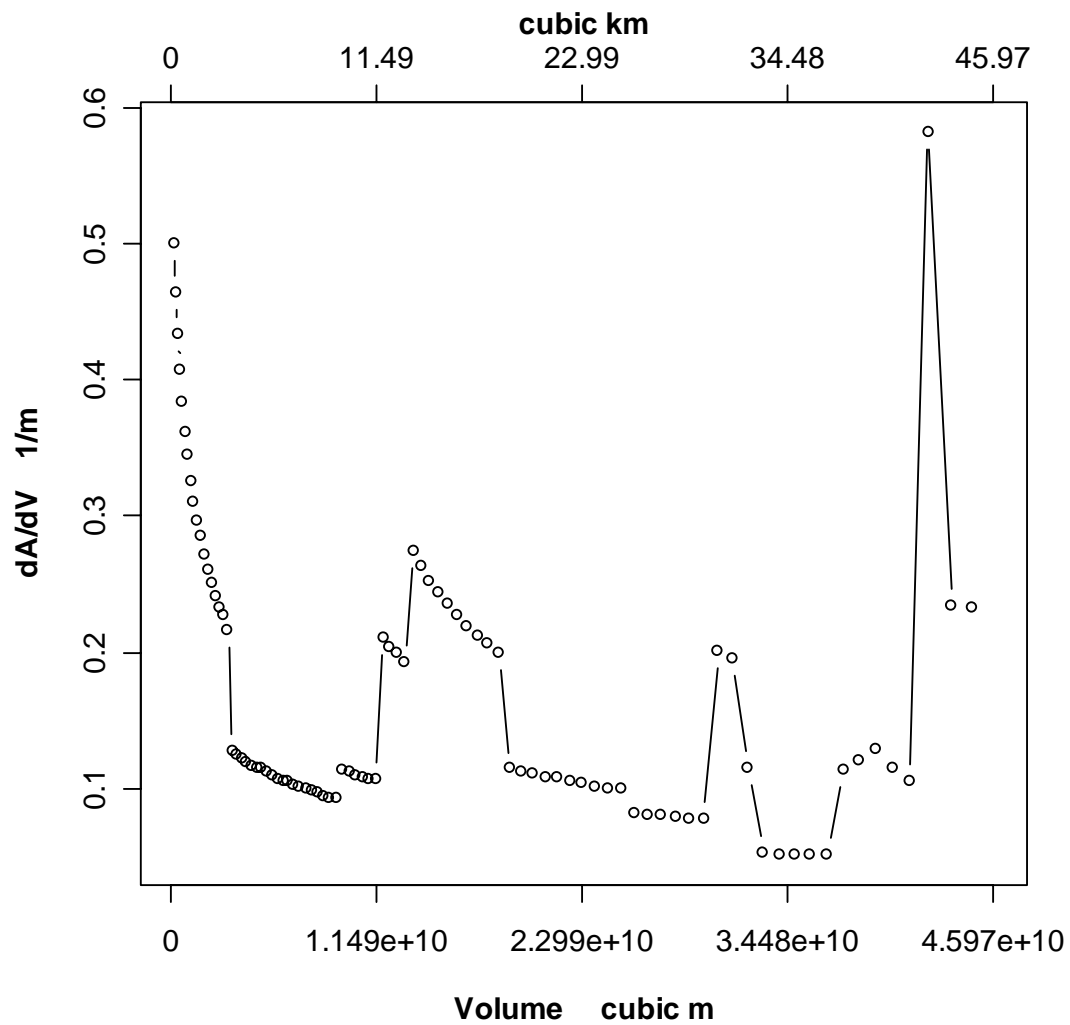
Figure 5-4. The topographic derivative, $\dfrac{dA}{dV}$ of the Great Salt Lake.
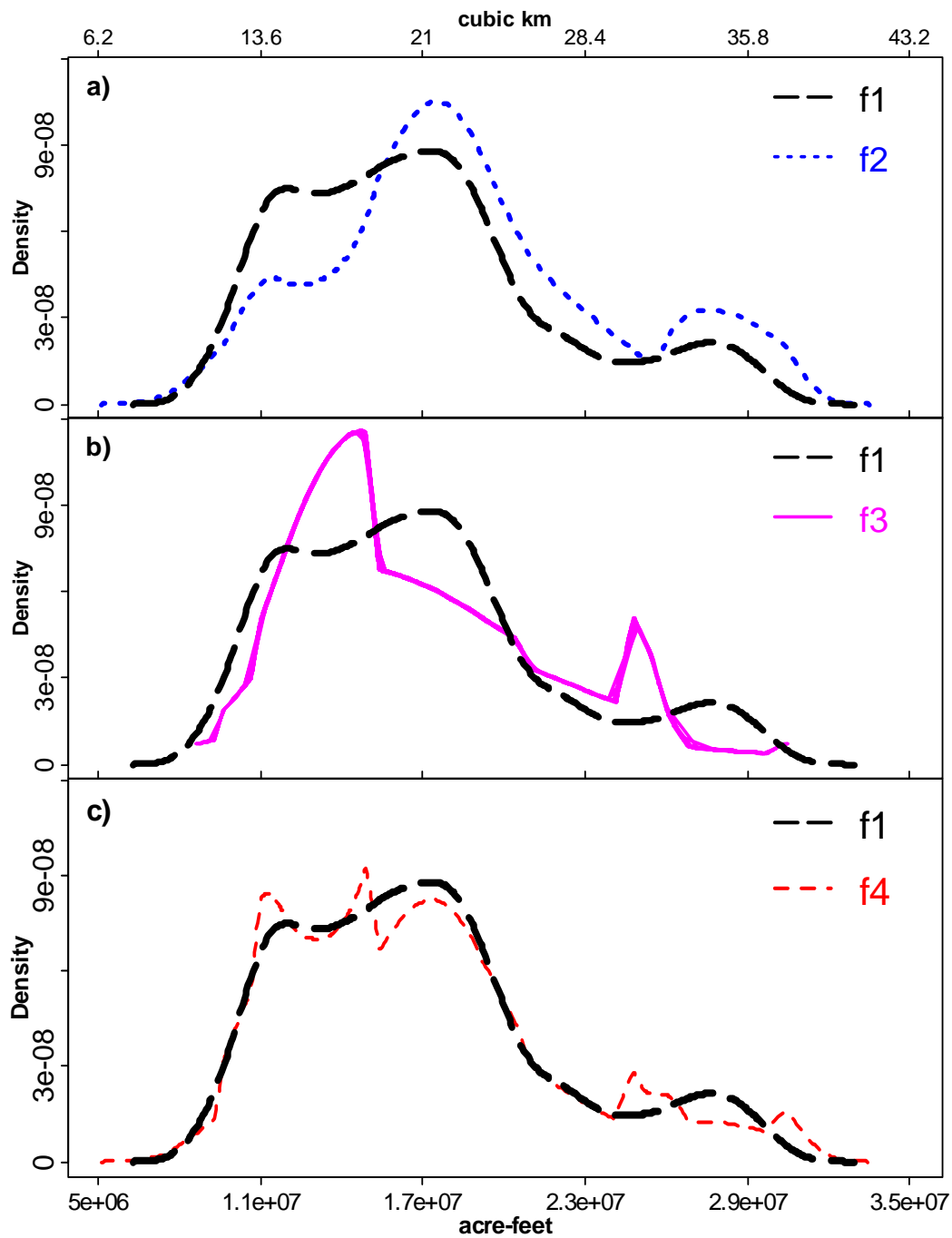
Figure 5-5. GSL volume density function comparisons: (a) density directly from data (f1) and density assuming constant dA/dV in Equation 5.7 (f2), (b) density directly from data (f1) and density assuming $f_A(a)$ is Gaussian in Equation 5.7 (f2), (c) density directly from data (f1) and observed $f_A(a)$ and dA/dV used in Equation 5.7 (f4).

5.2. Conclusion

This examination of the modes in the GSL volume and area distribution is part of our effort to understand lake dynamics and the different roles played by bathymetry and inputs from the hydrologic and climate system. We see that bathymetry, in addition to input multimodality is necessary to obtain the $f_V(v)$ distribution that Lall, Sangoyomi, and Abarbanel (1996) interpreted as suggestive of preferred states. We see that data acquired over the 14 years since the Lall, Sangoyomi, and Abarbanel (1996) work was done has changed our estimate of the shape of the volume PDF. We see, comparing Figures 5-2 and 5-3, that multimodality in the distribution of lake area is more pronounced than multimodality in lake volume. According to the simplified steady state analysis presented, lake area is more directly reflective of the balance between lake evaporation and input forcing. The pronounced multimodality in $f_A(a)$ is therefore even further suggestive of preferred states in the hydroclimatic forcing. However, this interpretation hinges on steady state, presuming that the area has had time to adjust to the forcing. A time scale for this adjustment can be estimated from the ratio of active volume to average flux rate. For the GSL the active volume is estimated as the range of volume values in Figures 5-1 and 5-2 as 27.1 km^3. The average annual input, I, is 3.3 km^3/year. This is balanced by evaporation. The resulting time scale is 8.1 years. The biweekly data interval used here is a lot shorter than this, and when the period of record is divided by the time scale, we get 19. This is an estimate of the effective number of

independent data points in this analysis and needs to be borne in mind in interpreting

the strength of these results and conclusions.

CHAPTER 6

EVAPORATION AND SALINITY

The Great Salt Lake is the fourth largest terminal lake in the world (the Caspian Sea is the largest lake in the world by volume). The only outflow from the GSL is evaporation, so lake level is determined by the balance between inflows and outflows. Evaporation from the GSL is sensitive to salinity which changes the saturation vapor pressure above the lake's surface. Salinity decreases as volume increases and visa versa. Salinity changes with lake volume as the total salt load in the lake becomes concentrated or diluted. The effect of salinity on evaporation is important for water balance computations and other engineering studies related to terminal lakes. This chapter presents a modification to the Penman equation that accommodates the reduction in saturation vapor pressure due to salinity. This is then tested against mass balance calculations of evaporation. In addition, the relationship between evaporation depth and area is presented.

6.1. Salinity and Total Salt Load

The GSL is a saline lake divided by the causeway into two arms (north and south) that have different salinity because all the river inflow (Bear, Weber, and Jordon/Provo rivers) enters the southern arm. As indicated in chapter 3, Figure 3-1, salinity was measured intermittently at 4 locations: AS2 (40.835˚N, 112.255˚W), and FB2 (41.135˚N, 112.46˚W) in the south arm and LVG4 (41.3241˚N, 112.7608˚W)

and RD2 (41.4416˚N, 112.7475˚W) in the north arm. Measurements were made at 5 depths. These measurements did not occur at the same time at all stations.

Salinity in the GSL has been affected by the West Desert pumping project (http://www.water.utah.gov/construction/gsl/index.htm) that during 1987-1989 removed more than 2.5 million acre-ft of water (3084 million cubic meters) and about 695 million tons of salt from the lake (Wold, Thomas, and Waddell, 1997). The pumps only operated for a 27-month period from April 1987 to June 1989, but from January 1990 to June 1992, 200,000 acre-ft of water (246.7 million cubic meters) and 94 million tons of salt flowed back to the lake from the West Pond.

Because it is the salinity at the lake surface that directly affects evaporation we first examined the salinity measured at the surface (top 0.2 m). Figure 6-1 shows how the surface salinity of the GSL differs in its two arms as a function of lake level. In this figure no distinction is made between the salinity measured at separate stations in the same arm of the lake. In Figure 6-1 we used different symbols for the pre and post 1987 salt concentrations so as to be able to examine the impact of the West Desert Pumping Project. There is an apparent relationship between salinity and lake level reflected by the fact that salinity declines as the volume increases with increasing level, the effect of the lakes salt load being diluted. The post 1987 surface salinities appear to be slightly reduced from the pre 1987 ones reflecting some measurable impact from the West Desert pumping. The relationship between salinity and lake level in Figure 6-1 was approximated separately for each arm of the lake using LOWESS (R-defaults).
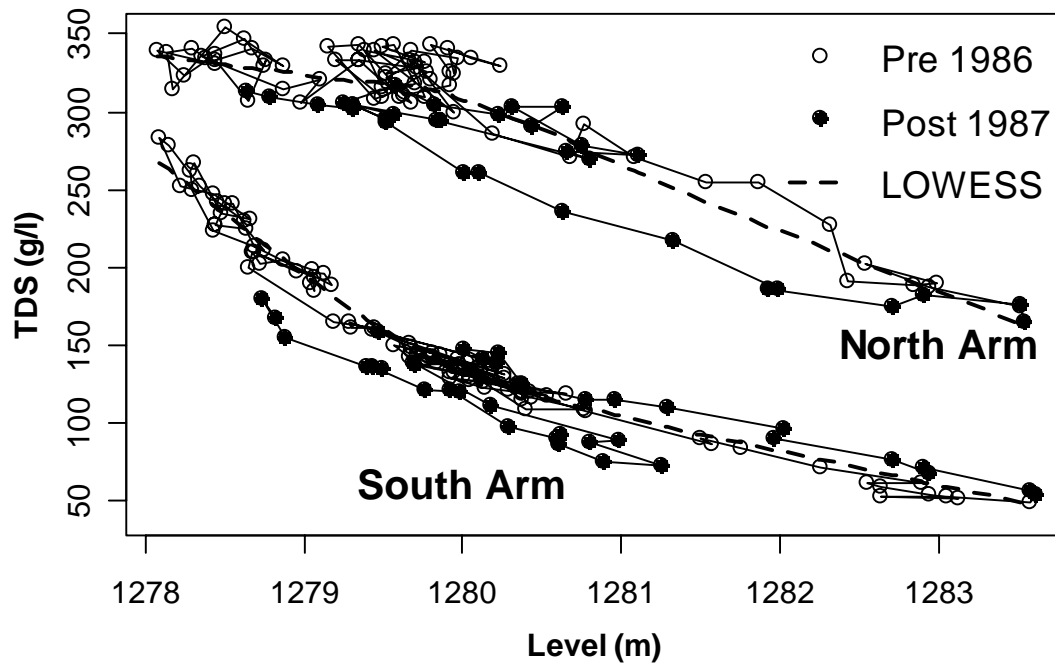
Figure 6-1.   Great Salt Lake surface salinity time series. Pre and post 1987 show
the effect of the West Desert pumping project.

　　　　To better understand the volume and dilution effects on salinity we examined

the GSL salinity fluctuations in terms of total dissolved salt load. This examination

of salt dynamics is important to understand the GSL's salt - level fluctuations as well

as the impact on evaporation. At each of the 4 measurement stations salinity has

been recorded at 5 depths.   To estimate total salt load we therefore used the

following procedure. For each station, be it in the north or south arm, a load was

calculated at the time of observation as:

$$\text{Load}_t = \sum_{i=1}^{5} C_{i,t} V_{i,t} \tag{6.1}$$

where Load$_t$ is the salt load at time t, C$_{i,t}$ is the total dissolved solids concentration at time t for layer i, i = 1, 2, ...5 , and V$_{i,t}$ is the layer i volume at time t calculated from the bathymetry using the top and bottom levels of layer i. We used the following depth ranges to define layers to perform the salt load calculation: (0 - 0.762 m), (0.762 - 2.286 m), (2.286 -3.810 m), (3.810 - 6.858 m), and (6.858 - bottom). These depth ranges were chosen to bracket the depths at which salinity was regularly measured (Figure 6-2). The occasional measurements at depths of 7.62 m, 10.69 m and 12.19 m were not used. The volume associated with each layer was determined from the lake level at the time of observation and the bathymetry for the arm of the observation. In other words we are assuming that each single salinity measurement is representative of the salinity of the entire arm of the lake at the depth at which it was taken. Linear interpolation was then used to infer a continuous load from the observations at each of the 4 stations separately (LVG4, RD2 in the north and AS2, FB2 in the south). The load for each arm was then approximated by averaging these continuous load interpolations for the stations in each arm. Figure 6-3 gives the total salt load calculated at each station and the continuously approximated load for each arm as well as the total salt load for the entire lake calculated by adding the continuously approximated loads from each arm. The north arm salt load behavior is different from the south arm. As the GSL rose due to inflows in the south arm, the south arm became more dilute. However, saline waters adjacent to the causeway moved to north arm through causeway. That movement carried a load of salt into the north arm resulting in an increase in north arm salt load

and decrease in south arm north load seen in the period going up to 1985 in Figure 6-3. When the Pumping Project started in April 1987 the north arm salt load began to decrease. This is due to the fact of pumping was from the north arm. While the north arm salt load decreased the south arm salt load increased. This may be due to density driven circulation across the causeway, or dissolution of salt deposits within the lake. The dotted lines in Figure 6-3 are the average total salt load before and after the West Desert Pumping Project. These averages were calculated only within the time presented in the figure. The approximated average total salt load is different before and after the West Desert pumping project. This reflects a reduction in salt load of around 320 M tons due to the pumping project. The pumping project is reported to have removed about 695 M tons of salt, with 94 M tons being returned with the recirculated brine. There are considerable uncertainties in these calculations because they were based on point measurements at two locations in each arm and a limited number of depths, so this level of discrepancy is not surprising. These calculations of the salt balance of the GSL as well as movement through the causeway are consistent with similar results well documented by Loving, Waddell, and Miller (2000).

We also examined the constituents that comprise the salt load in the north and south arms. Table 6-1 shows the constituents of the GSL on different dates spanning the range of salinity observed in the north and south arms from the Utah Geological Survey data (Table 3-1). The lowest total dissolved solids (TDS) in the north arm observed was 175.7 g/l on June 9th, 1987, while in the south arm was 49.3 g/l on Jan

20th, 1986. The highest TDS observed in the north arm was 354.5 g/l on July 16th,

1968, while in the south arm was 282.84 g/l on Oct 27th , 1966. The dominant ions

are Na and Cl which comprise about 80 % of the ionic mass in both arms. Across

the range of salinity observed the percentages of ionic mass contributed by each ion

remain essentially constant. This was also apparent in Figure 3-10.
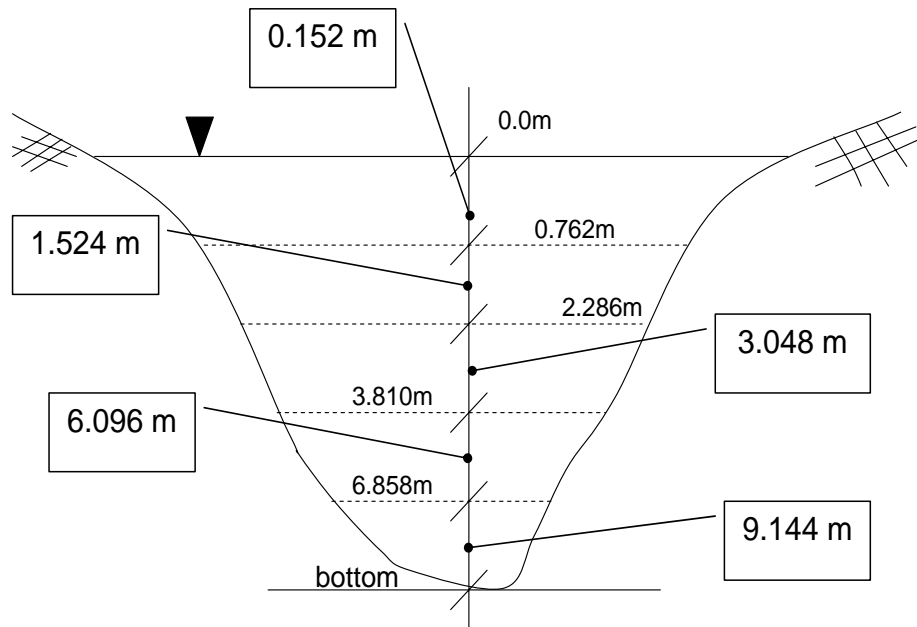
Figure 6-2.   Depth ranges used to evaluate the GSL Salt Load.
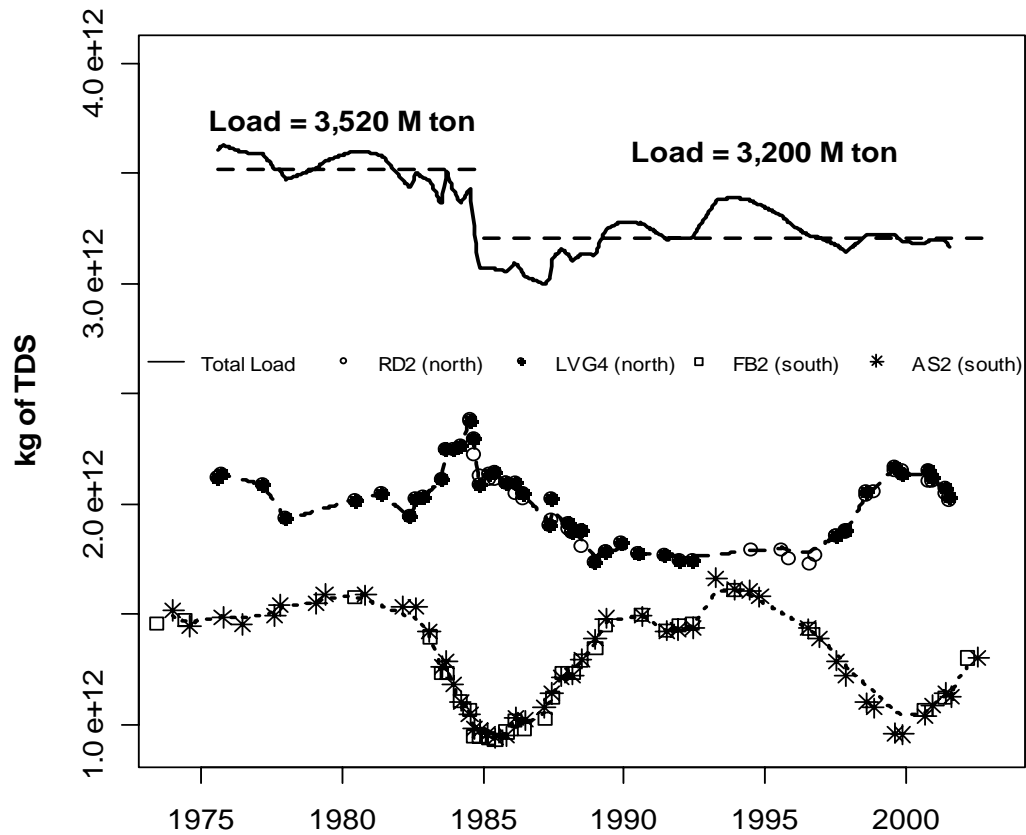
Figure 6-3.   The GSL salt load for the north arm, the south arm and the total for the entire lake.

6.2. Salinity Impact on Evaporation

Stumm and Morgan (1981) defined the activity coefficient, β, of water with salinity, S, as the ratio of vapor pressure over salt water to vapor pressure over fresh water at the same temperature. This activity coefficient of water (β) in a solution of known chemical composition can be calculated using a composite reduction factor obtained by summing the weighted reduction in saturation vapor pressure due to each of the constituent salt ions. Therefore, the saturation vapor pressure above a

saline surface $e'_{sat}(T_s, S_s)$ is less than saturation vapor pressure $e_{sat}(T_s)$ of fresh water at the same temperature. The GSL brine has high salinity (175.7 g/l - 354.5 g/l) presented in Table 6-1 which gives high ionic strength. The estimation of the activity of water coefficient for brine such as the GSL brine requires solving a set of equations known as the Pitzer equations (Pitzer, 1973). We used the USGS software PHREEQC (Parkhurst and Appelo, 1999) to solve the Pitzer equations and calculate the water activity coefficient. This was done for a range of temperature and salinity values consistent with ranges observed in the GSL. This was then combined with a standard saturation vapor pressure-temperature function for fresh water to calculate saturation vapor pressure adjusted for salinity. The results are shown in Figure 6-4. The reduction in saturation vapor pressure due to salinity varies from 10% to 40% depending upon salinity.

6.3. Modified Penman

The Penman equation, e.g. Dingman (2002), is an energy balance equation for the calculation of evaporation from a water body based upon meteorological conditions above the water surface. It is derived based on an assumption that the surface temperature and vapor pressure can be approximated using air temperature and humidity and the gradient of the saturation vapor pressure-temperature curve. The surface vapor pressure is then used to determine the vapor pressure gradient that drives evaporation. Over a saline water body where the saturation vapor pressure also depends upon salinity, this derivation needs to be modified to account for the

modifications to the saturation vapor pressure-temperature curve indicated above in Figure 6-4. This derivation is presented here.
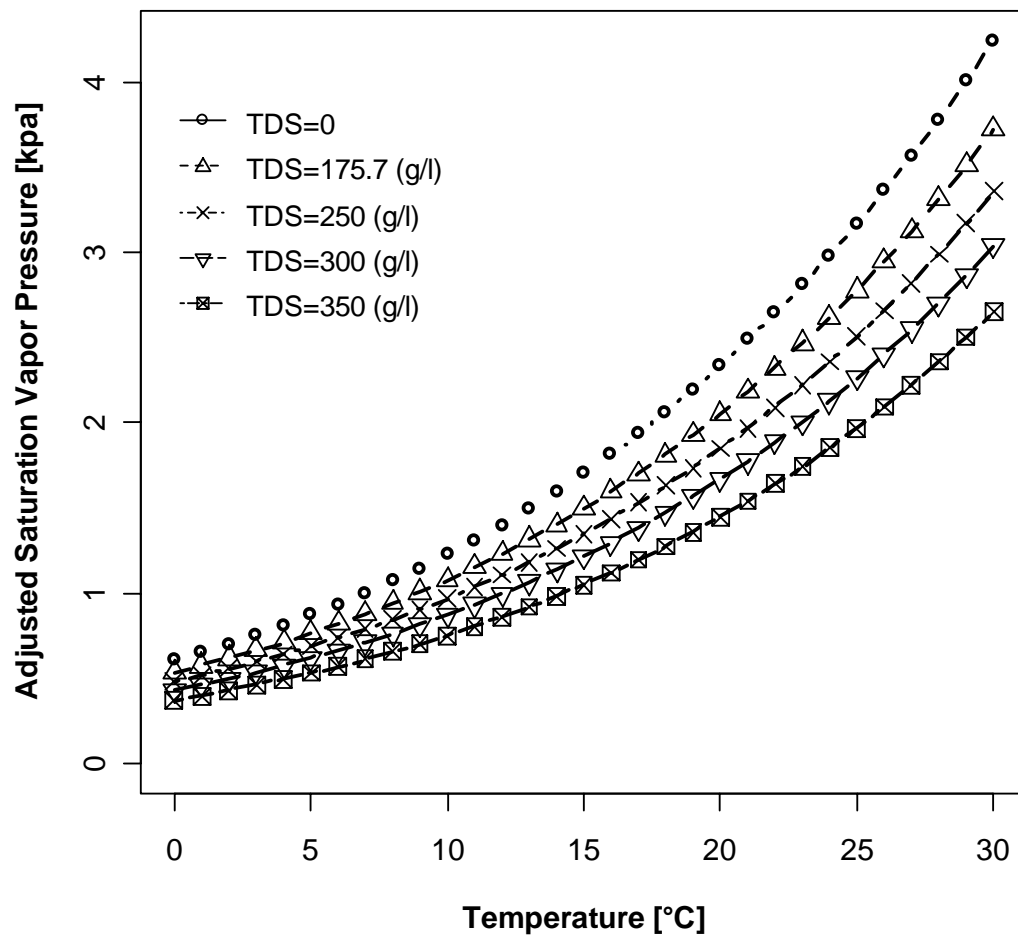
Figure 6-4.   Saturation vapor pressure adjusted for salinity based upon the salt ion composition of the GSL.

Table 6-1.   The constituents percentages of the Great Salt Lake at its north and south arms

Arm	Date	TDS g/L	Level ft	Na % WT	K % WT	Mg % WT	Ca % WT	Cl % WT	SO$_4$ % WT
North	1987, June 9th	175.70	4210.7	32.2	3.3	1.9	0.2	56.5	5.9
	1991, June 12th	236.10	4201.0	33.5	2.9	1.7	0.2	55.7	6.0
	1993, April 27th	293.70	4197.4	32.5	3.3	2.1	0.1	55.7	6.3
	1970, August 4th	347.00	4194.8	31.4	3.9	3.0	0.1	53.4	8.2
	1968, July 16th	354.50	4194.4	25.6	4.2	2.7	0.1	56.4	11.0
	Average			**31.0**	**3.5**	**2.3**	**0.1**	**55.5**	**7.5**
South	1986, January 20th	49.30	4211.45	31.1	2.0	3.6	0.3	56.1	6.9
	2001, July 18th	97.63	4200.40	32.7	2.0	2.6	0.2	55.9	6.7
	1972, October 27th	149.33	4198.10	30.1	2.6	2.9	0.1	56.6	7.7
	1970, August 26th	202.22	4195.30	30.6	2.1	3.5	0.1	55.7	7.8
	1967, January 27th	251.71	4193.70	27.8	2.6	3.0	0.2	58.0	8.6
	1966, October 27th	282.84	4193.2	33.2	2.4	2.9	0.1	54.1	7.3
	Average			**30.9**	**2.3**	**3.1**	**0.2**	**56.1**	**7.5**
GSL Total				**30.95**	**2.90**	**2.70**	**0.15**	**55.80**	**7.50**

The energy balance for an evaporating water body can be written as:

$$E = \frac{R_n - H}{\rho_w \lambda_v}$$

(6.2)

where, E is evaporation $[LT^{-1}]$, R_n is net energy available at the water surface $[EL^{-2}T^{-1}]$, H is net sensible heat exchange with atmosphere $[EL^{-2}T^{-1}]$, ρ_w is density of water $[ML^{-3}]$, and λ_v is the latent heat of vaporization $[EM^{-1}]$; $\lambda_v = 2.5 - 2.36 \times 10^{-3} T$; T in °C. R_n, the net energy available at the water surface is comprised of the net radiation minus conduction in to the lake. Conduction in to the lake is a quantity that is hard to obtain, so for longer time scales is often neglected. The sensible heat exchange H can be written as:

$$H = K_H v_a (T_s - T_a)$$

(6.3)

where, K_H is bulk sensible heat transfer coefficient $[EL^{-3}T^{-1}]$, v_a is wind speed over the surface $[LT^{-1}]$, T_s and T_a are surface and air temperatures respectively. Similar to sensible heat, evaporation is proportional to the difference between the pressure of saturated vapor at the water and vapor pressure of the air, expressed as:

$$E = K_E v_a (e_s - e_a)$$

(6.4)

where, e_s and e_a are vapor pressures of the water surface and of the air, respectively; K_E is bulk latent heat transfer coefficient $[LT^2M^{-1}]$; E is evaporation. In the latent heat equation e_s is written as a function of T_s based on the fresh water saturation vapor pressure function. Here however we write e_s in terms of the saturation vapor pressure of a saline water surface:

$$E = K_E v_a (e'_{sat}(T_s,S_s) - e_a) \qquad (6.5)$$

where, $e'_{sat}(T_s,S_s) = e_s(T_s)\beta(S,T_s)$ gives the saturation vapor pressure of a saline water surface in terms of the water activity coefficient $\beta(S,T_s)$, a function of temperature T_s and salinity S. Then following the standard approach used in deriving the Penman equation the saturation vapor pressure of the saline surface is approximated based on the saturation vapor pressure gradient and air temperature using a Taylor series approximation:

$$e'_s(T_s,S_s) \cong e'_s(T_a,S_s) + \Delta'(T_s - T_a)$$

$$\Delta' = \frac{de'_s}{dT}\bigg|_{T_a,S} \qquad (6.6)$$

$$\Delta' = \frac{\partial e_s}{\partial T_s}\beta + e_s\frac{\partial \beta}{\partial T_s}\bigg|_{T_a}$$

where, is Δ' is the gradient of the saturated vapor pressure for a saline surface [kPa°C^{-1}], here expressed in terms of the fresh water $e_s(T_s)$ gradient and water activity coefficient gradient.

Equation (6.5) can then be rewritten as:

$$E = K_E v_a (e'_{sat}(T_a, S_s) - e_a + \Delta'(T_s - T_a)) \tag{6.7}$$

and from equation (6.3) (T_s-T_a) can be replaced by:

$$(T_s - T_a) = \frac{H}{K_H v_a}. \tag{6.8}$$

Substituting equation (6.8) in equation (6.7) and arranging equations (6.2) to (6.6) we can derive a modified Penman evaporation equation accounting for salinity:

$$E_{sal} = \frac{\Delta'}{\gamma + \Delta'} \cdot \frac{R_n}{\lambda_v \rho_w} + \frac{\gamma}{\gamma + \Delta'} \cdot K_E v_a (e_a \beta(T_a) - e_a) \tag{6.9}$$

where

$$\gamma = \frac{K_H}{\lambda_v \rho_w K_E} = \text{psychrometric constant [kPa°C}^{-1}\text{]}.$$

Net radiation measurements are not available over the GSL. To implement this equation we therefore used the Hargreaves and Samani method (Allen et al., 1998) for estimating the net radiation R_n. The method can be summarized as:

$$R_n = R_{ns} - R_{nl} \qquad (6.10)$$

where, R_{ns} is the net solar or short wave radiation [MJ m^{-2} day^{-1}]; R_{nl} is the net outgoing long wave radiation [MJ m^{-2} day^{-1}] as calculated below. The net solar or short wave radiation R_{ns} mentioned in equation (6.10) is estimated from Hargreaves and Samani method using the following:

$$R_a = \frac{24(60)}{\pi} G_{sc} d_r \left[\omega_s \sin(phi) \sin(\delta) + \cos(phi) \cos(\delta) \sin(\omega_s) \right] \qquad (6.11)$$

where, R_a is the extraterrestrial radiation [MJm^{-2}day^{-1}], G_{sc} is the solar constant; G_{sc} = 0.082 [MJm^{-2}min^{-1}]; d_r is the relative earth to sun distance; $d_r = 1 + 0.033 \cos\left(\frac{2\pi}{365} J \right)$ with (J) as Julian date; phi is the latitude [rad], ω_s is the sunset hour angle [rad] ; $\omega_s = \arccos\left[-\tan(phi)\tan(\delta) \right]$; δ is the solar declination $\delta = 0.409 \sin\left(\frac{2\pi}{365} J - 1.39 \right)$ with (J) as Julian date. Hargreaves suggested the following formula for incoming solar radiation, R_s:

$$R_s = K_{RS} \sqrt{(T_{max} - T_{min})} R_a \tag{6.12}$$

where, K_{RS} is the adjustment coefficient applied as 0.16 to interior locations and 0.19 to coastal locations, T_{max} and T_{min} are in degrees Celsius. Hence, the net short wave radiation R_{ns} introduced in equation (6.10) can be estimated as:

$$R_{ns} = (1 - \alpha) R_s \tag{6.13}$$

where, α is the short wave radiation reflection coefficient (albedo) which Shuttleworth (1993) suggests as 0.08 for open water. The other term in equation (6.10) is net long wave radiation R_{nl} which Hargreaves and Samani suggest being calculated as:

$$R_{nl} = \sigma \left[\frac{T_{max,K}^4 + T_{min,K}^4}{2} \right] \left(0.34 - 0.14\sqrt{e_a} \right) \left(1.35 \frac{R_s}{R_{so}} - 0.35 \right) \tag{6.14}$$

where, σ is the Stefan – Boltzmann constant taken as 4.903×10^{-9} [MJ K^{-4} m^{-2} day^{-1}], $T_{max,K}$ and $T_{min,K}$ are maximum and minimum air temperature in degrees Kelvin; $K = °C + 273.16$; e_a is actual vapor pressure calculated from dew point air temperature, R_s is the incoming solar radiation [$MJm^{-2}day^{-1}$] from equation (6.12), R_{so} is clear sky solar radiation; $R_{so} = (a_s + b_s) R_a$ [$MJm^{-2}day^{-1}$] with $a_s = 0.25$ and $b_s = 0.5$ (Shuttleworth, 1993).

In equation (6.9) the bulk latent heat transfer coefficient (K_E) reflects the efficiency of vertical transport of water vapor by the turbulent eddies of the wind. It is calculated as (Dingman, 2002):

$$K_E = \frac{0.622 \cdot \rho_a}{P \cdot \rho_w} \cdot \frac{1}{6.25 \times \left[\ln\left(\frac{z_m - z_d}{z_o} \right) \right]^2} \qquad (6.15)$$

where, ρ_a is the density of air [ML^{-3}], P is the atmospheric pressure [$MT^{-2}L^{-1}$];

$P = 101.3 \left(\frac{293 - 0.0065z}{293} \right)^{5.256}$ with z [m] the elevation above sea level; ρ_w is the

density of water [ML^{-3}], z_m is the height at which wind speed and air vapor pressure are measured [L], z_d is the zero – plane displacement [L], and z_o is the roughness height of the surface [L]. Brutsaert (1982) suggested that using z_o as 2.30×10^{-4} m, z_d as 0 m and z_m as 2 m over a typical water surface with standard values for air and water properties in equation 6.15, K_E could be approximated as 1.26×10^{-3} [$msm^{-1}kPa^{-1}day^{-1}$]. We used this approximation because the Maurer et al. (2002) climate data represents variables measured at 2 m above the GSL surface but with P as 87.03 [kPa], K_E was then approximated as 1.28×10^{-3} [$msm^{-1}kPa^{-1}day^{-1}$]. This approximation of the bulk latent - heat transfer coefficient suggestion is reported in Dingman (2002). The modified Penman model above, equation (6.9), differs from Penman method described by (Dingman, 2002) in the correction made by the activity

water coefficient. In this work, we used equation (6.9) in estimating the evaporation over the Great Salt Lake. The adjusted saturation vapor pressure from Figure 6-4 was incorporated in equation (6.9).

6.4. Evaluation in Comparison to Mass Balance

Evaporation estimated from the GSL mass balance equation was presented in Chapter 4 during the fall period. In this chapter we used equation (4.4) on an annual basis to estimate the annual evaporation volume. Specifically,

$$E_v = Q + PA - \Delta V \tag{6.16}$$

where Q is the annual streamflow volume, P is the annual precipitation depth over the lake, A is the lake area averaged for each specific year based on lake level records and ΔV is the change in lake volume based on lake level records.

We calculated the depth of evaporation from the GSL with the Penman and modified Penman equation (4.9) using a monthly time step and monthly climate data (Table 3-1), separately for each arm. The surface salinity was taken as the average of any measurements that occurred in each month in each arm. For months that did not have any surface salinity measurements, surface salinity was estimated from level using the LOWESS line in Figure 6-1. The surface salinity and average air temperature over each arm was then fed to the USGS software PHREEQC

(Parkhurst and Appelo, 1999) to get the water activity coefficient required to adjust the saturation vapor pressure over the water surface for that specific month. The derivative of water activity coefficient needed for equation (6.6) was evaluated numerically based on output from PHREEQC. Monthly evaporation depth values were then multiplied by the respective arm area to obtain volumes that were then aggregated for all months and the arm volumes added together to get the lake total annual evaporation volume estimates.

Figure 6-5 compares the calculations of annual evaporation volume from the Penman and modified Penman equations to the evaporation volume obtained from mass balance. Figure 6-5 shows that without accounting for salinity the Penman equation overestimates evaporation in comparison to mass balance, but that with the adjustments for salinity the modified Penman and mass balance calculations compare well. There are outliers that occur in 1983 and 1984 where, as discussed earlier, we surmise that there were other inflows (such as West Desert inflows) to the lake resulting in the mass balance calculations being too low.

The relation between evaporation and area is important, since evaporation is the only outflow from the GSL. Salinity affects the evaporation of the GSL by from 10% to 40%. We mentioned in Chapter 4 that during the fall period (July - October) the relation between evaporation depth calculated from mass balance and area did not show the salinity effect. In this chapter we used the modified Penman equation (6.9) to examine this question again. Figures 6-6 and 6-7 give the relation between evaporation depth with area for the rise (Nov. – June) and the fall (Jul. – Oct.)

periods respectively. In Figures 6-6 and 6-7 we used the mass balance equation (4.4) to get the rise and fall evaporation depth estimates on the right plots in each figure. The mass balance evaporation depth with area estimate relationship used during the fall period in Figure 6-7 is same as Figure 4-4. The left plots in Figures 6-6 and 6-7 present the modified Penman evaporation calculations aggregated for the rise and fall periods separately. The calculations for each arm were averaged, weighted by area. Salinity inputs were the same as used for Figure 6-5.
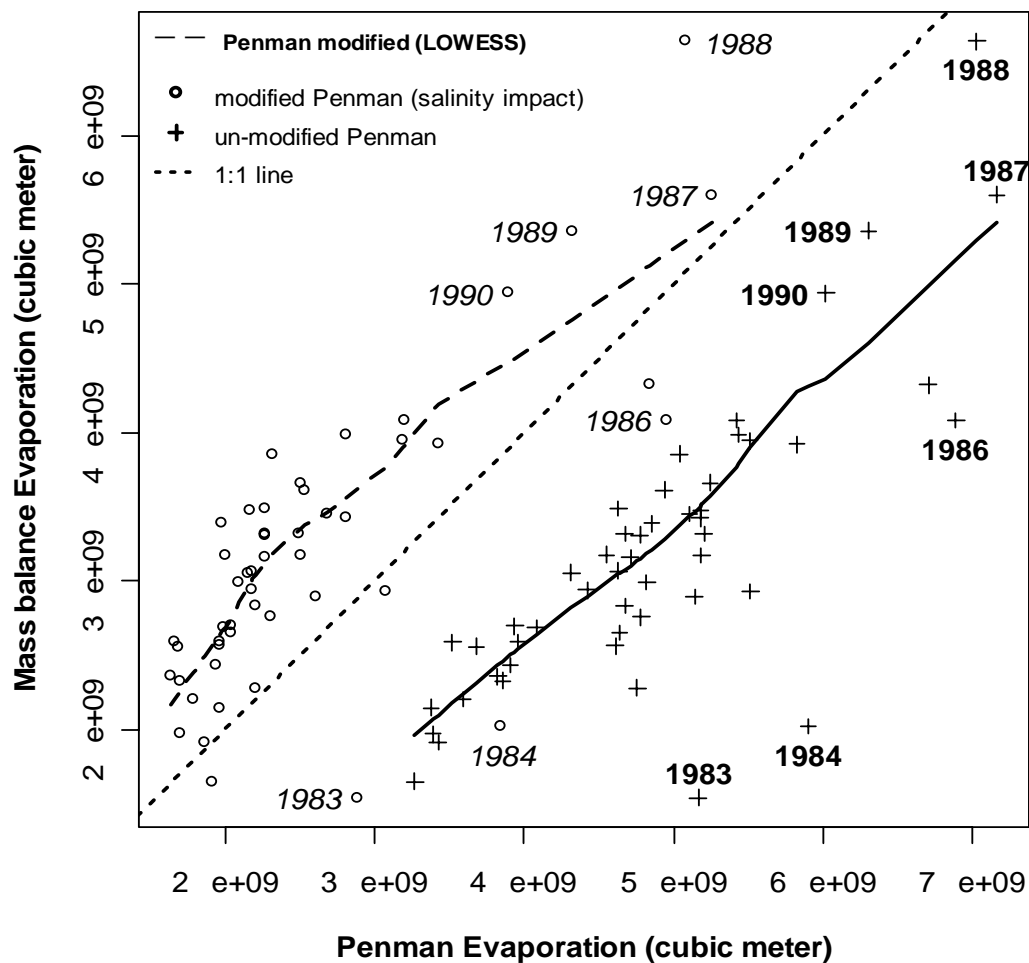
Figure 6-5.   Salinity impact on the GSL evaporation using LOWESS relations.

There are three observations to note in examining these figures. First, the scatter on the modified Penman graphs is less than in the mass balance plot, indicating less variability in the climate inputs that drive evaporation. Some of the variability in the mass balance E estimates may be due to uncertainties in the mass balance approach associated with uncertainties in Precipitation, P, Lake Inflow, Q and Lake Area, A used in equation 6.16. Secondly, the Penman estimates are greater than the mass balance estimates during the rise period, but less than the mass balance estimates during the fall. This may reflect storage of energy in the lake during the time it is rising, coming out of the winter when the lake is cold. During this period there is less energy available for evaporation than anticipated by the Penman method, so the Penman method overestimates evaporation relative to mass balance. The opposite holds in the fall when the lake is warm and losing heat, some of it contributing to evaporation. Variability in these heat storage effects may also explain some of the variability in the mass balance estimates. Thirdly, it is possible to discern in the modified Penman calculations an increasing trend with area that is due to the reduction in salinity with increases in lake volume due to dilution. The magnitude of this effect can be up to a 40% difference in evaporation depth over the range of lake area and salinity present in the GSL.

6.5. Conclusion

This chapter has explored the relationships between evaporation and salinity. We introduced a modification to the Penman equation for estimating the evaporation

from a saline water surface. This modification involves adjusting the saturation vapor pressure using the water activity coefficient. The salinity of the GSL results in reduction of the saturation vapor pressure over the GSL surface from between 10% - 40% depending upon the salinity which varies with lake level. We compared (Figure 6-5) evaporation estimates based on salinity using the modified Penman equation (6.9) with the mass balance estimate from equation (4.4). We found that annual evaporation calculated from the modified Penman equation compared well to mass balance evaporation estimates, whereas without the salinity modifications the Penman equation overestimates lake evaporation. We found some seasonal differences between fall and rise period modified Penman and mass balance calculation of evaporation that may be due to heat storage. Further examination of these potential heat storage effects is suggested for future research. We found that the salt concentration in the GSL varies with lake volume, with total salt load remaining roughly constant. This variation in salinity is therefore essentially a dilution effect and can result in up to 40% variation in the depth of evaporation from the GSL. Our findings indicate the importance of accounting for salinity and how it varies with lake volume and area in modeling the overall evaporation from and hydrology of the Great Salt Lake.
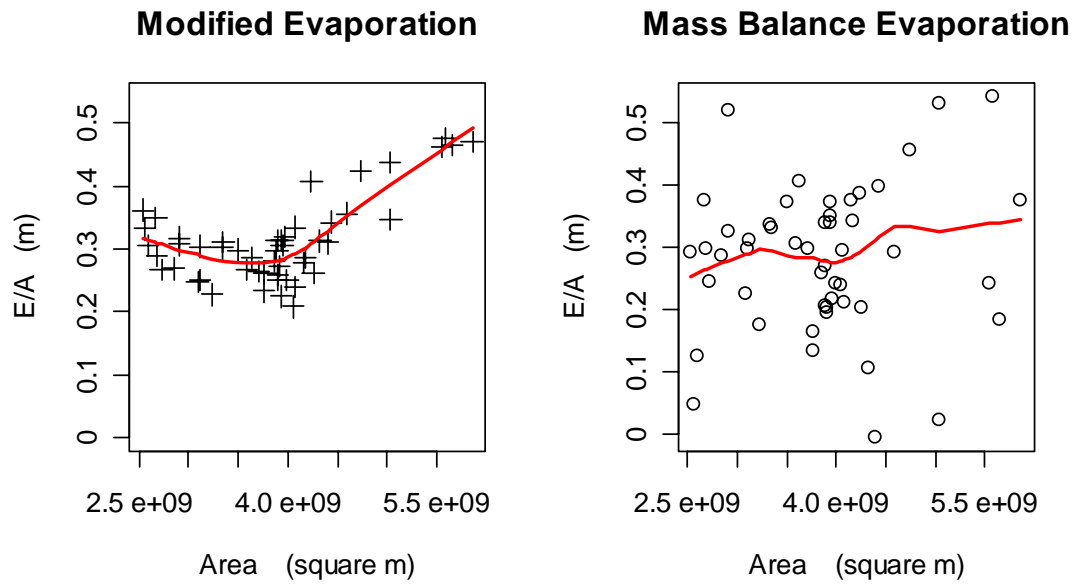
Figure 6-6.   GSL area and evaporation relationship using two methods (mass balance, modified Penman) during the rise period (Nov. – June).
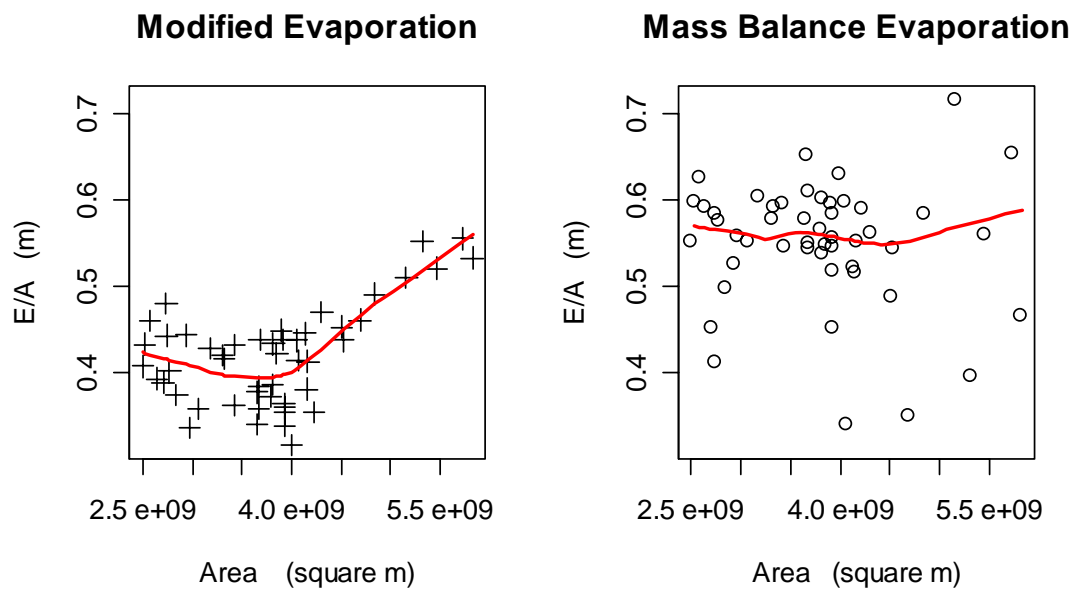
Figure 6-7.   GSL area and evaporation relationship using two methods (mass balance, modified Penman) during the fall period (Jul. – Oct.).

CHAPTER 7

SUMMARY AND CONCLUSIONS

Applying stochastic methods in the Great Salt Lake study basin helped us in understanding and interpreting the underlying dynamics that cause the GSL level/volume to change.   Understanding the observed variability in the GSL level/volume was the main objective of this work. The major issue in understanding the variability associated with the GSL level/volume changes is the complex interactions between various variables that affect the GSL level/volume. In order to contribute to the effort to understand this variability we undertook the following three tasks: a) predicting the GSL volume variability, b) examination of how modes, representing preferred states in the GSL volume series are connected to the bathymetry, and c) a methodology to estimate the outflow, i.e. evaporation, from the GSL.

In the first task, the changes of the GSL volume were studied. The GSL goes through an annual cycle rising in the winter and spring due to precipitation and streamflow inputs and falling in the summer and autumn due to evaporation. Spectral analysis was used to identify the dates when the lake reaches its maximum volume (peak) and minimum volume (trough) on average over the annual cycle. We found that on an average the lake is rising between November 1 and June 15, then falling from June 15 to November 1. The changes in volume during these periods of fall and rise were then predicted through a regression model.   The explanatory

variables of the regression model were streamflow, precipitation, and lake area. The order of these variables is according to their importance in a stepwise regression model. The values of the coefficients in the regression were found to be generally consistent with mass balance. This model is not a complete predictive model because it requires inputs that occur at the same time as the volume change being predicted. Nevertheless this model serves to quantify some of the internal workings of the GSL system that when combined with forecasts for streamflow and precipitation could be used for prediction.

The next task focused on the shape of the GSL volume probability density function and how it relates to the lake bathymetry. Lall, Sangoyomi, and Abarbanel (1996) studied the GSL volume data from 1847 to 1992 and observed multimodality in the probability density function (PDF) of the GSL volume. Modes in the GSL volume distribution were interpreted as preferred states in the GSL dynamic system. We constructed the PDF of the GSL volume using volume data from 1847 to 2004 and observed that the multimodality was not as pronounced as shown by Lall, Sangoyomi, and Abarbanel (1996). The data collected during the 14 years following Lall, Sangoyomi, and Abarbanel (1996) did not change the main modes but rather changed the trough between the two main modes. Bathymetry plays a role in the dynamics of the GSL and occurrence of modes in the GSL volume distribution, because it relates lake volume to area that controls the outflow evaporation. We examined this effect and found that the derivative of the area-volume function was important for explaining the lake volume distribution. The lake volume distribution

was also found to be related to the distribution of lake area which is more directly connected to the driving climate processes.

The last task was estimating evaporation from the GSL. Evaporation from a saline water body has been a challenge in hydrology because several factors interact and affect the evaporation process. Dickson, Yepsen, and Hales (1965) as well as Turk (1970) studied the hydrology of salt flats and established relative evaporation rates for brines from the GSL containing various amounts of dissolved solids. We developed a modified Penman equation that incorporates a salinity parameter to estimate evaporation from the GSL. The modified Penman equation was evaluated using the mass balance estimate of the GSL evaporation. Due to the salinity observed in the GSL brine the estimate of the GSL saturation vapor pressure was found to be 10% - 40% less compared to a fresh water surface. Variability in the GSL volume results in changes in salinity due to dilution. These salinity changes are responsible for relative variability of evaporation depths from the GSL up to 40%.

The results from this study that merit further investigations are: (1) The causes of the probability density function modes and why we experienced a change in the multimodality in the last 14 years. (2) When we assume the lake is not under steady state, does bathymetry still play a major role in shaping the multimodality. (3) Can the models and understanding of lake behavior that has been developed be used to understand how lake levels and volumes might respond to climate change that has been argued recently. Have risks of flooding from the lake changed due to climate change. (4) Evaluating the modified Penman equation for estimating evaporation by

testing its results with real measurements. (5) The formation of salt crusts sometimes experienced in the north arm and the effects these have on inhibiting evaporation. (6) The heat dynamics of the lake and how they affect evaporation.

This study contributed towards an active area of research which is the Great Salt Lake. Our methods form an additional application of stochastic hydrology in the Great Salt Lake basin. It has provided better understanding on how external forcings, lake characteristics, and outflow process are interacting in the GSL basin system dynamics.

REFERENCES

Abarbanel, H. D. I., U. Lall, Y. I. Moon, M. E. Mann, and T. Sangoyomi. 1996. Nonlinear dynamics and the great salt lake: A predictable indicator of regional climate. Energy 21(7-8): 655-665.

Adams, T. C. 1934. Evaporation from great salt lake. Bulletin of the American Meteorological Society 15(2): 35-39.

Aguado, E., D. Cayan, L. Riddle, and M. Roos. 1992. Climatic fluctuations and the timing of west-coast streamflow. Journal of Climate 5(12): 1468-1483.

Allen, R. G., L. S. Pereira, D. Raes, and M. Smith. 1998. Crop evapotranspiration - guidelines for computing crop water requirements. FAO Irrigation and drainage (56): 328.

Asefa, T., M. Kemblowski, U. Lall, and G. Urroz. 2005. Support vector machines for nonlinear state space reconstruction: Application to the great salt lake time series. Water Resources Research 41(12): W12422.

Becker, R. A., J. M. Chambers, and A. R. Wilks. 1988. The new S language: A programming environment for data analysis and graphics. Wadsworth & Brooks/Cole Advanced Books & Software, Pacific Grove, California. 702 p.

Bonython, C. W. 1966. Factors determining the rate of solar evaporation in the production of salt. 2nd Symposium on Salt. May 3-5, 1963, Cleveland, Ohio, p.152-167.

Brutsaert, W. 1982. Evaporation into the atmosphere: Theory, history, and applications. Kluwer Boston, 299 p.

Cayan, D. R., S. A. Kammerdiener, M. D. Dettinger, J. M. Caprio, and D. H. Peterson. 2001. Changes in the onset of spring in the western united states. Bulletin of the American Meteorological Society 82(3): 399-415.

Dettinger, M. D., and D. R. Cayan. 1995. Large-scale atmospheric forcing of recent trends toward early snowmelt runoff in california. Journal of Climate 8(3): 606-623.

Dickson, D. R., J. H. Yepsen, and J. V. Hales. 1965. Saturated vapor pressure over great salt lake brine. Journal of Geophysical Research 70(2): 500-503.

Dingman, S. L. 2002. Physical hydrology, Second Edition. Prentice Hall, Upper Saddle River, New Jersey. 646 p.

Fan, Y., and C. J. Duffy. 1993. Monthly temperature and precipitation fields on a storm-facing mountain front - statistical structure and empirical parameterization. Water Resources Research 29(12): 4157-4166.

Harbeck, G. E., M. A. Kohler, and G. E. Koberg. 1958. Water-loss investigations: Lake mead studies. Professional Paper 298. U.S. Geological Survey, Washington, D.C,

James, L. D., D. S. Bowles, W. R. James, and R. V. Canfield. 1979. Estimation of water surface elevation probabilities and associated damages for the great salt lake. UWRL/P-79/03. Utah Water Research Laboratory, Utah State University, Logan, Utah.182 p.

Lall, U. 1995. Recent advance in nonparametric function estimation - hydrologic application. Reviews of Geophysics 33: 1093-1102.

Lall, U., and M. Mann. 1995. The great-salt-lake - a barometer of low-frequency climatic variability. Water Resources Research 31(10): 2503-2515.

Lall, U., T. Sangoyomi, and H. D. I. Abarbanel. 1996. Nonlinear dynamics of the great salt lake: Nonparametric short-term forecasting. Water Resources Research 32(4): 975-985.

Lall, U., and A. Sharma. 1996. A nearest neighbor bootstrap for resampling hydrologic time series. Water Resources Research 32(3): 679-693.

Liang, X., D. P. Lettenmaier, E. F. Wood, and S. J. Burges. 1994. A simple hydrologically based model of land-surface water and energy fluxes for general-circulation models. Journal of Geophysical Research-Atmospheres 99(D7): 14415-14428.

Loving, B. L., K. M. Waddell, and C. W. Miller. 2000. Water and salt balance of great salt lake, utah, and simulation of water and salt movement through the causeway, 1987-98. Water-Resources Investigations Report, 00-4221. U.S. Geological Survey, 2000, Salt Lake City, Utah. 32 p.

Macdonald, G. J. 1989. Spectral-analysis of time-series generated by nonlinear processes. Reviews of Geophysics 27(4): 449-469.

Mann, M. E., U. Lall, and B. Saltzman. 1995. Decadal-to-centennial-scale climate variability - insights into the rise and fall of the great-salt-lake. Geophysical Research Letters 22(8): 937-940.

Maurer, E. P., A. W. Wood, J. C. Adam, D. P. Lettenmaier, and B. Nijssen. 2002. A long-term hydrologically based dataset of land surface fluxes and states for the conterminous united states. Journal of Climate 15(22): 3237-3251.

McCabe, G. J., and D. M. Wolock. 2002. A step increase in streamflow in the conterminous united states. Geophysical Research Letters 29(24): Art. No. 2185.

Moon, Y.-I. 1995. Large scale atmospheric variability and the Great Salt Lake. Unpublished Ph.D. Thesis. Utah State University, Logan, Utah. 140 p.

Moon, Y.-I., and U. Lall. 1996. Atmospheric flow indices and interannual great salt lake variability. Journal of Hydrologic Engineering 1(2): 55-62.

Mote, P. W. 2003. Trends in snow water equivalent in the pacific northwest and their climatic causes. Geophysical Research Letters 30(12): Art. No. 1601.

Mote, P. W., A. F. Hamlet, M. P. Clark, and D. P. Lettenmaier. 2005. Declining mountain snowpack in western north america. Bulletin of the American Meteorological Society 86(1): 39-49.

Parkhurst, D. L., and C. A. J. Appelo. 1999. User's guide to phreeqc (version 2)—a computer program for speciation, batch-reaction, one-dimensional transport, and inverse geochemical calculations. Water Resources Investigations Report 99-4259. U.S. Geological Survey, Denver, Colorado. 309 p.

Pitzer, K. S. 1973. Thermodytriarnics of electrolytes, i . Theoretical basis and general equations. Journal of Physical Chemistry 77(2): 268-277.

Plaut, G., and R. Vautard. 1994. Spells of low-frequency oscillations and weather regimes in the northern hemisphere. Journal of the Atmospheric Sciences 51(2): 210-236.

Regonda, S. K., B. Rajagopalan, M. Clark, and J. Pitlick. 2005. Seasonal cycle shifts in hydroclimatology over the western united states. Journal of Climate 18(2): 372-384.

Rohwer, C. 1933. Evaporation from salt solutions and from oil-covered water surfaces. Journal of Agricultural Research 46(1): 715-729.

Salhotra, A. M. 1986. A coupled heat, salt and water balance model of evaporation and stratification in saline terminal lakes: An application to the dead sea. Unpublished Ph.D Thesis. Massachusetts Institute of Technology, Cambridge, Massachusetts. 377 p.

Salhotra, A. M. 1987. The alpha, beta, gamma of evaporation from saline water bodies. Water Resources Research 23(9): 1769-1774.

Salhotra, A. M., E. E. Adams, and D. R. F. Harleman. 1985. Effect of salinity and ionic composition on evaporation - analysis of dead sea evaporation pans. Water Resources Research 21(9): 1336-1344.

Salhotra, A. M., E. E. Adams, and D. R. F. Harleman. 1992. On the concept of evaporation from fresh and saline water bodies - comment. Water Resources Research 28(5): 1491-1491.

Sangoyomi, T. 1993. Climatic variability and dynamics of great salt lake hydrology. Unpublished Ph.D. Thesis. Utah State University, Logan, Utah. 264 p.

Sangoyomi, T. B., U. Lall, and H. D. I. Abarbanel. 1996. Nonlinear dynamics of the great salt lake: Dimension estimation. Water Resources Research 32(1): 149-159.

Sharma, A., D. G. Tarboton, and U. Lall. 1997. Streamflow simulation: A nonparametric approach. Water Resources Research 33(2): 291-308.

Sheather, S. J., and M. C. Jones. 1991. A reliable data-based bandwidth selection method for kernel density-estimation. Journal of the Royal Statistical Society Series B-Methodological 53(3): 683-690.

Shun, T., and C. J. Duffy. 1999. Low-frequency oscillations in precipitation, temperature, and runoff on a west facing mountain front: A hydrogeologic interpretation. Water Resources Research 35(1): 191-201.

Shuttleworth, W. J. 1993. Evaporation, p.4.1-4.47. In D. R. Maidment (1st Ed). Handbook of hydrology. McGRAW Hill, Inc., New York.

Silverman, B. W. 1986. Density estimation for statistics and data analysis, 1st Edition. Chapman and Hall, London ; New York. ix, 175 p.

Slack, J. R., A. M. Lumb, and J. M. Landwehr. 1993. Hydro-climatic data network (hcdn) stream flow data set, 1874-1988. Water-Resources Investigations Report 93-4076. U.S. Geological Survey, Denver, Colorado.

Stumm, W., and J. J. Morgan. 1981. Aquatic chemistry : An introduction emphasizing chemical equilibria in natural waters, Second Edition. Wiley, New York. 780 p.

Sturrock, A. M., Jr. 1978. Evaporation and radiation measurements at salton sea, california. Water-Supply Paper No.W 2053. U. S. Geological Survey, Reston, Virginia. 26 p.

Tarboton, D. G., A. Sharma, and U. Lall. 1998. Disaggregation procedures for stochastic hydrology based on nonparametric density estimation. Water Resources Research 34(1): 107-119.

Turk, L. J. 1969. Hydrogeology of the bonneville salt flats, utah. Unpublished Ph.D. Thesis. Stanford University, Stanford, California. 328 p.

Turk, L. J. 1970. Evaporation of brine: A field study on the bonneville salt flats, utah. Water Resources Research 6(4): 1209-1215.

Vapnik, V. N. 1995. The nature of statistical learning theory. Springer, New York. 188 p.

Vautard, R., P. Yiou, and M. Ghil. 1992. Singular-spectrum analysis - A toolkit for short, noisy chaotic signals. Physica D 58(1-4): 95-126.

Wei, W. W. S. 1990. Time series analysis : Univariate and multivariate methods. Addison-Wesley Pub., Redwood City, California. 478 p.

Wold, S. R., B. E. Thomas, and K. M. Waddell. 1997. Water and salt balance of great salt lake, utah, and simulation of water and salt movement through the causeway. Water-Supply Paper 2450. U.S. Geological Survey, Denver, CO, p. vi, 64.

Wold, S. R., and K. M. Waddell. 1994. Salt budget for west pond, utah, april 1987 to June 1989. Water-Resources Investigations Report 93-4028. U.S. Geological Survey; Denver, Colorado, Salt Lake City, Utah. 20 p.

Young, A. A. 1947. Some recent evaporation investigations. Transactions, American Geophysical Union 28(2): 279-284.

APPENDIX

This appendix presents a comparison of Maurer et al. (2002) gridded data with metrological station data as a cross check on the data reliability. The metrological station data provides us with precipitation, temperature and other climate indices. We obtained datasets from NCDC (National Climate Data Center, (http://www.ncdc.noaa.gov/oa/ncdc.html) and the Western Regional Climate Center, (http://www.wrcc.dri.edu/index.html). A set of representative stations that had been previously used by Fan and Duffy (1993) was extracted from these two sites with the climate variables available (Table A-1 and Figure A-1). The monthly and seasonal (winter months) correlations between the gage and the gridded datasets were calculated and presented in Tables A-2 and A-3. The monthly correlation is the whole year (12 months), while seasonal correlation is winter months (i.e., November - February). Two sets of correlations were calculated one with the raw data and the other with the deseasonlized data. We calculated the deseasonlized data as explained and presented in equation (4.5). All the correlations are above 0.9 indicative of consistency between the gridded and station data. These results provide assurance for using the gridded dataset (Maurer et al., 2002).
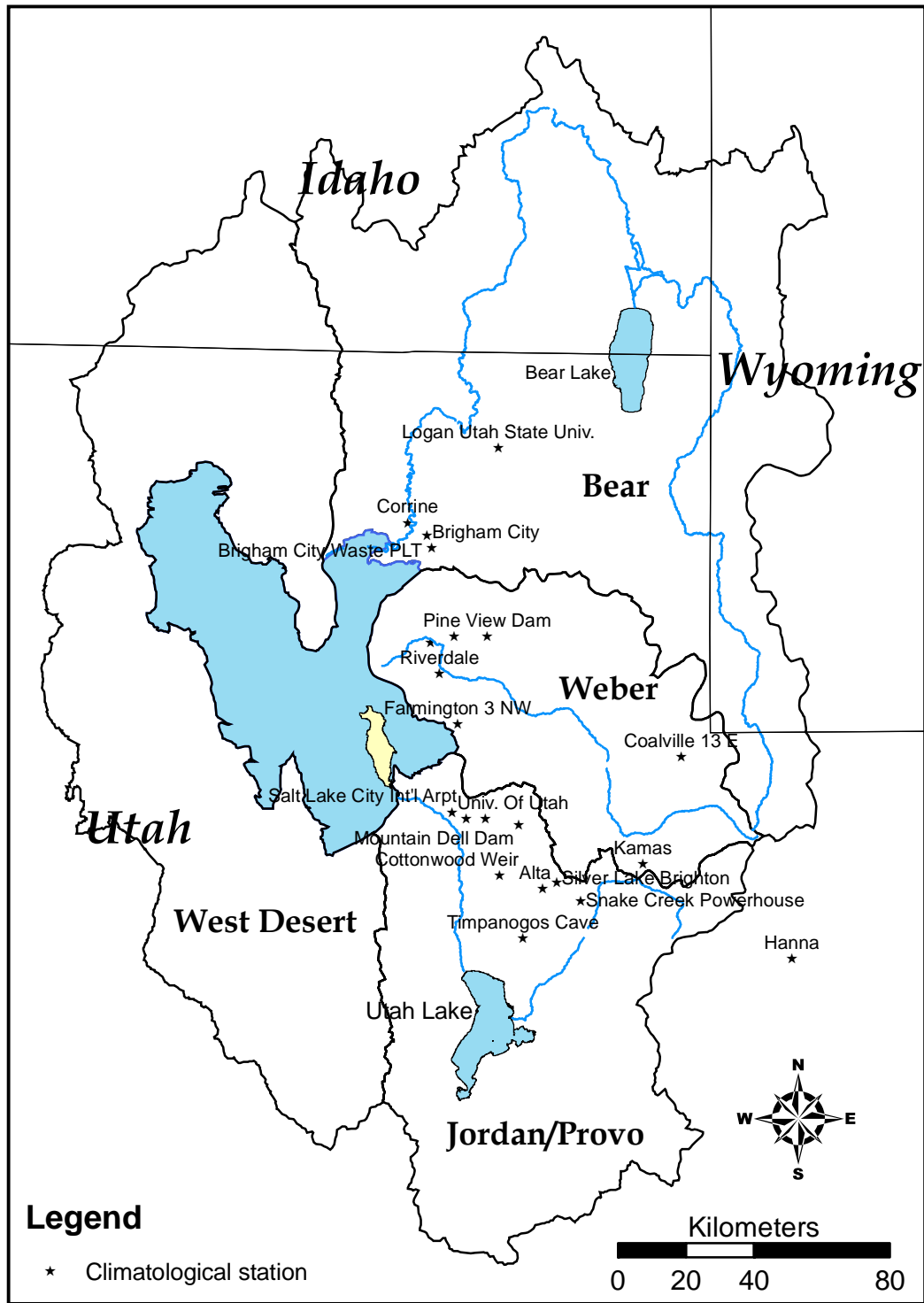
Figure A-1.   Climatological stations in the Great Salt Lake Basin.

Table A-1.   Climatological stations in the Wasatch Plateau

No.	Station	Latitude, °N	Longitude, °W	Elevation, m	Observed Years of Record	Source
1	Silver Lake Brighton	40° 36´	111° 35´	2664.0	Jan 1931 – Mar 2004	NCDCa
2	Salt Lake City Int'L Arpt	40° 47´	111° 57´	1287.8	Jan 1948 – Mar 2004	NCDC
3	Mountain Dell Dam	40° 45´	111° 43´	1652.0	Jan 1931 – Mar 2004	NCDC
4	Snake Creek Powerhouse	40° 33´	111° 30´	1831.8	Jan 1928 – Apr 2004	WRCCb
5	Brigham City	41° 29´	112° 02´	1324.1	Apr 1913 – Jan 1974	NCDC
6	Brigham City Waste Plt	41° 31´	112° 03´	1289.3	Jul 1974 – Mar 2004	NCDC
7	Ogden Sugar Factory	41° 14´	112° 02´	1304.5	Sep 1924 – Mar 2004	NCDC
8	Alta	40° 35´	111° 38´	2660.9	Dec 1944 – Mar 2004	NCDC
9	Corrine	41° 33´	112° 07´	1289.3	Feb 1871 – Mar 2004	WRCC
10	Cottonwood Weir	40° 37´	111° 47´	1511.8	Jan 1931 – Mar 2004	NCDC
11	Farmington 3 NWc	41° 01´	111° 56´	1335.0	Jan 1948 – Apr 2004	WRCC
12	Riverdale	41° 09´	112° 00´	1341.1	Feb 1914 – Feb 1991	NCDC
13	Ogden Pioneer PH	41° 15´	111° 57´	1325.9	Jan 1902 – Jun 2004	WRCC
14	Salt Lake City Downtown	40° 46´	111° 54´	1299.1	Jan 1928 – Jul 1954	WRCC
15	Timpanogos Cave	40° 27´	111° 42´	1719.1	Jan 1947 – Apr 2004	NCDC
16	Logan Utah State Univ.	41° 45´	111° 48´	1460.0	Mar 1893 – Apr 2004	WRCC
17	Coalville 13 E	40° 56´	111° 09´	1984.2	Oct 1974 – Jun 2004	WRCC
18	Hannad	40° 24´	110° 46´	2055.9	Jun 1952 – May 2004	WRCC
19	Kamas	40° 39´	111° 17´	1973.6	Oct 1948 – Jun 2004	WRCC
20	Pine View Dam	41° 15´	111° 50´	1505.7	Jan 1935 – Jun 2004	NCDC
21	Univ. Of Utah	40° 46´	111° 50´	1463.0	Jan 1949 – Feb 1990	WRCC

[a] National Climate Data Center ~ NOAA.
[b] Western Regional Climate Center.
[c] Nearest gage station to the Lake.
[d] Located outside the Great Basin with nearest grid about 23 Km.

Table A-2. Correlation, full data, between gage stations and gridded type format precipitation data

No.	Station	Observed Years of Record	Nearest Grid Location (Lat, Long)	4 Surrounding Grids Locations (Lat, Long)	Monthly Correlation (nearest grid)	Monthly Correlation Average of 4 Surroundings grids	Monthly Correlation (Deseasonlized) (nearest grid)	Monthly Correlation Average of 4 (Deseasonlized) Surroundings grids
1	Silver Lake Brighton	Jan 1931–Mar 2004	(40.5625,-111.5625)	(40.5625,-111.5625) (40.5625,-111.6875) (40.6875,-111.5625) (40.6875,-111.6875)	0.9674567	0.9402569	0.962731	0.9305498
2	Salt Lake City Int'L Arpt	Jan 1948–Mar 2004	(40.8125,-111.9375)	(40.6875,-111.9375) (40.6875,-112.0625) (40.8125,-111.9375) (40.8125,-112.0625)	0.9658605	0.9493205	0.9709512	0.9485387
3	Mountain Dell Dam	Jan 1931–Mar 2004	(40.6875,-111.6875)	(40.6875,-111.6875) (40.6875,-111.8125) (40.8125,-111.6875) (40.8125,-111.8125)	0.8521127	0.9038737	0.915321	0.9425206
4	Snake Creek Powerhouse	Jan 1928–Apr 2004	(40.5625,-111.4375)	(40.4375,-111.4375) (40.4375,-111.5625) (40.5625,-111.4375) (40.5625,-111.5625)	0.9655797	0.9480951	0.9725305	0.9354464
5	Brigham City	Apr 1913–Jan 1974	(41.4375,-112.0625)	(41.4375,-111.9375) (41.4375,-112.0625) (41.5625,-111.9375) (41.5625,-112.0625)	0.9669296	0.9507917	0.9921509	0.980635
6	Brigham City Waste Plt	Jul 1974–Mar 2004	(41.5265,-112.0625)	(41.4375,-111.9375) (41.4375,-112.0625) (41.5625,-111.9375) (41.5625,-112.0625)	0.9628457	0.9296348	0.970387	0.9735264
7	Ogden Sugar Factory	Sep 1924–Mar 2004	(41.1875,-112.0625)	(41.1875,-111.9375) (41.1875,-112.0625) (41.3125,-111.9375) (41.3125,-112.0625)	0.9579267	0.9194725	0.9640052	0.9472113
8	Alta	Dec 1944 – Mar 2004	(40.5625,-111.6875)	(40.5625,-111.5625) (40.5625,-111.6875) (40.6875,-111.5625) (40.6875,-111.6875)	0.941017	0.9400774	0.959915	0.9363565
9	Corrine	Feb 1871–Mar 2004	(41.5625,-112.0625)	(41.4375,-112.0625) (41.4375,-112.1875) (41.5625,-112.0625) (41.5625,-112.1875)	0.9570886	0.9466636	0.9631913	0.9497666
10	Cottonwood Weir	Jan 1931–Mar 2004	(40.5265,-111.8125)	(40.5625,-111.6875) (40.5625,-111.8125) (40.6875,-111.6875) (40.6875,-111.8125)	0.8852469	0.8298669	0.926559	0.8888446

Table A-2.   Continued

No.	Station	Observed Years of Record	Nearest Grid Location (Lat, Long)	4 Surrounding Grids Locations (Lat, Long)	Monthly Correlation (nearest grid)	Monthly Correlation Average of 4 Surroundings grids	Monthly Correlation (Deseasonlized) (nearest grid)	Monthly Correlation Average of 4 (Deseasonlized) Surroundings grids
11	Farmington 3 NW[a]	Jan 1948– Apr 2004	(41.0625,-111.9375)	(40.9375,-111.8125) (41.0625,-111.8125) (41.0625,-111.9375) (41.0625,-112.0625)	0.9594938	0.9382896	0.9693102	0.9688826
12	Riverdale	Feb 1914– Feb 1991	(41.1875,-112.0625)	(41.0625,-111.9375) (41.0625,-112.0625) (41.1875,-111.9375) (41.1875,-112.0625)	0.9669028	0.9489534	0.973731	0.9682137
13	Ogden Pioneer PH	Jan 1902– Jun 2004	(41.1875,-111.9375)	(41.1875,-111.9375) (41.1875,-112.0625) (41.3125,-111.9375) (41.3125,-112.0625)	0.9413977	0.9571855	0.9731723	0.9756837
14	Salt Lake City Downtown	Jan 1928– Jul 1954	(40.8125,-111.9375)	(40.6875,-111.8125) (40.6875,-111.9375) (40.8125,-111.8125) (40.8125,-111.9375)	0.9690754	0.949065	0.9830979	0.9784916
15	Timpanogos Cave	Jan 1947– Apr 2004	(40.4375,-111.6875)	(40.4375,-111.6875) (40.4375,-111.8125) (40.5625,-111.6875) (40.5625,-111.8125)	0.9558412	0.884848	0.9928542	0.9212436
16	Logan Utah State Univ.	Mar 1893– Apr 2004	(41.8125,-111.8125)	(41.6875,-111.6875) (41.6875,-111.8125) (41.8125,-111.6875) (41.8125,-111.8125)	0.9674945	0.9418369	0.9753158	0.9795756
17	Coalville 13 E	Oct 1974– Jun 2004	(40.9375,-111.1875)	(40.8125,-111.0625) (40.8125,-111.1875) (40.9375,-111.0625) (40.9375,-111.1875)	0.937856	0.8703732	0.9654899	0.9520516
18	Hanna[b]	Jun 1952– May 2004	(40.5625,-110.9375)	(40.3125,-111.1875) (40.4375,-111.0625) (40.5625,-110.9375) (40.6875,-110.8125)	0.7315353	0.7069491	0.8737283	0.8349902
19	Kamas	Oct 1948– Jun 2004	(40.6875,-111.3125)	(40.5625,-111.1875) (40.5625,-111.3125) (40.6875,-111.1875) (40.6875,-111.3125)	0.9735163	0.9412305	0.9744978	0.9639684
20	Pine View Dam	Jan 1935– Jun 2004	(41.1875,-111.8125)	(41.1875,-111.8125) (41.1875,-111.9375) (41.3125,-111.8125) (41.3125,-111.9375)	0.948232	0.9555628	0.9666836	0.9540218
21	Univ. Of Utah	Jan 1949– Feb 1990	(40.8125,-111.8125)	(40.6875,-111.8125) (40.6875,-111.9375) (40.8125,-111.8125) (40.8125,-111.9375)	0.859298	0.9358097	0.8855552	0.9376995

[a] Nearest gage station to the Lake.
[b] Located outside the Great Basin with nearest grid about 23 Km.

Table A-3.   Seasonal correlation, winter months, between gage stations and gridded type format precipitation data

No.	Station	Observed Years of Record	Nearest Grid Location (Lat., Long.)	4 Surrounding Grids Locations (Lat., Long.)	Seasonal Monthly Correlation (nearest grid)	Seasonal Monthly Correlation Average of 4 Surroundings grids	Seasonal Monthly Correlation (Deseasonlized) (nearest grid)	Seasonal Monthly Correlation Average of 4 (Deseasonlized) Surroundings grids
1	Silver Lake Brighton	Jan 1931–Mar 2004	(40.5625,-111.5625)	(40.5625,-111.5625) (40.5625,-111.6875) (40.6875,-111.5625) (40.6875,-111.6875)	0.959363	0.9123908	0.9024989	0.9204108
2	Salt Lake City Int'L Arpt	Jan 1948–Mar 2004	(40.8125,-111.9375)	(40.6875,-111.9375) (40.6875,-112.0625) (40.8125,-111.9375) (40.8125,-112.0625)	0.9375414	0.9220975	0.8354669	0.9370552
3	Mountain Dell Dam	Jan 1931–Mar 2004	(40.6875,-111.6875)	(40.6875,-111.6875) (40.6875,-111.8125) (40.8125,-111.6875) (40.8125,-111.8125)	0.8557414	0.9081365	0.8006733	0.9333062
4	Snake Creek Powerhouse	Jan 1928–Apr 2004	(40.5625,-111.4375)	(40.4375,-111.4375) (40.4375,-111.5625) (40.5625,-111.4375) (40.5625,-111.5625)	0.97639	0.9635374	0.9239312	0.9604403
5	Brigham City	Apr 1913–Jan 1974	(41.4375,-112.0625)	(41.4375,-111.9375) (41.4375,-112.0625) (41.5625,-111.9375) (41.5625,-112.0625)	0.9896724	0.9667468	0.8135143	0.9773185
6	Brigham City Waste Plt	Jul 1974–Mar 2004	(41.5265,-112.0625)	(41.4375,-111.9375) (41.4375,-112.0625) (41.5625,-111.9375) (41.5625,-112.0625)	0.9512909	0.9511482	0.9293742	0.9650308
7	Ogden Sugar Factory	Sep 1924–Mar 2004	(41.1875,-112.0625)	(41.1875,-111.9375) (41.1875,-112.0625) (41.3125,-111.9375) (41.3125,-112.0625)	0.9570677	0.9196487	0.881421	0.9474974
8	Alta	Dec 1944–Mar 2004	(40.5625,-111.6875)	(40.5625,-111.5625) (40.5625,-111.6875) (40.6875,-111.5625) (40.6875,-111.6875)	0.964371	0.9386	0.850547	0.9338728
9	Corrine	Feb 1871–Mar 2004	(41.5625,-112.0625)	(41.4375,-112.0625) (41.4375,-112.1875) (41.5625,-112.0625) (41.5625,-112.1875)	0.9592104	0.9455791	0.906854	0.948648
10	Cottonwood Weir	Jan 1931–Mar 2004	(40.5265,-111.8125)	(40.5625,-111.6875) (40.5625,-111.8125) (40.6875,-111.6875) (40.6875,-111.8125)	0.8278893	0.7681343	0.858992	0.8092565

Table A-3. Continued

No.	Station	Observed Years of Record	Nearest Grid Location (Lat., Long.)	4 Surrounding Grids Locations (Lat., Long.)	Seasonal Monthly Correlation (nearest grid)	Seasonal Monthly Correlation Average of 4 Surroundings grids	Seasonal Monthly Correlation (Deseasonlized) (nearest grid)	Seasonal Monthly Correlation Average of 4 (Deseasonlized) Surroundings grids
11	Farmington 3 NW[a]	Jan 1948– Apr 2004	(41.0625,-111.9375)	(40.9375,-111.8125) (41.0625,-111.8125) (41.0625,-111.9375) (41.0625,-112.0625)	0.9513051	0.9537257	0.911486	0.9695314
12	Riverdale	Feb 1914– Feb 1991	(41.1875,-112.0625)	(41.0625,-111.9375) (41.0625,-112.0625) (41.1875,-111.9375) (41.1875,-112.0625)	0.9641478	0.9612131	0.8566751	0.9757837
13	Ogden Pioneer PH	Jan 1902– Jun 2004	(41.1875,-111.9375)	(41.1875,-111.9375) (41.1875,-112.0625) (41.3125,-111.9375) (41.3125,-112.0625)	0.9409628	0.9549184	0.9125442	0.9698249
14	Salt Lake City Downtown	Jan 1928– Jul 1954	(40.8125,-111.9375)	(40.6875,-111.8125) (40.6875,-111.9375) (40.8125,-111.8125) (40.8125,-111.9375)	0.9637169	0.9658368	0.6751508	0.9808923
15	Timpanogos Cave	Jan 1947– Apr 2004	(40.4375,-111.6875)	(40.4375,-111.6875) (40.4375,-111.8125) (40.5625,-111.6875) (40.5625,-111.8125)	0.983506	0.8913909	0.9705589	0.8905012
16	Logan Utah State Univ.	Mar 1893– Apr 2004	(41.8125,-111.8125)	(41.6875,-111.6875) (41.6875,-111.8125) (41.8125,-111.6875) (41.8125,-111.8125)	0.9649523	0.9721884	0.9168349	0.976182
17	Coalville 13 E	Oct 1974– Jun 2004	(40.9375,-111.1875)	(40.8125,-111.0625) (40.8125,-111.1875) (40.9375,-111.0625) (40.9375,-111.1875)	0.9188518	0.8946444	0.8708427	0.9413712
18	Hanna[b]	Jun 1952– May 2004	(40.5625,-110.9375)	(40.3125,-111.1875) (40.4375,-111.0625) (40.5625,-110.9375) (40.6875,-110.8125)	0.8896954	0.8841886	0.8981337	0.8970242
19	Kamas	Oct 1948– Jun 2004	(40.6875,-111.3125)	(40.5625,-111.1875) (40.5625,-111.3125) (40.6875,-111.1875) (40.6875,-111.3125)	0.9769424	0.9366262	0.9540583	0.971269
20	Pine View Dam	Jan 1935– Jun 2004	(41.1875,-111.8125)	(41.1875,-111.8125) (41.1875,-111.9375) (41.3125,-111.8125) (41.3125,-111.9375)	0.9538072	0.9538368	0.9309928	0.9619078
21	Univ. Of Utah	Jan 1949– Feb 1990	(40.8125,-111.8125)	(40.6875,-111.8125) (40.6875,-111.9375) (40.8125,-111.8125) (40.8125,-111.9375)	0.8293617	0.9073139	0.8444689	0.9192553

[a] Nearest gage station to the Lake.
[b] Located outside the Great Basin with nearest grid about 23 Km.